Separation and Purification Technology 229 (2019) 115790

Contents lists available at ScienceDirect

Separation and Purification Technology

journal homepage: www.elsevier.com/locate/seppur

Short Communication

Maxwell-Stefan modelling of mixture desorption kinetics in microporous crystalline materials

Rajamani Krishna

Van 't Hoff Institute for Molecular Sciences, University of Amsterdam, Science Park 904, 1098 XH Amsterdam, the Netherlands

ARTICLE INFO

Keywords:
Transient desorption
Microporous adsorbents
Maxwell-Stefan diffusion
Thermodynamic coupling
Uphill diffusion
Vacuum blowdown

ABSTRACT

In kinetically driven separations using microporous crystalline adsorbents, the more mobile component is recovered during the desorption phase of pressure swing adsorption (PSA) processes. The primary focus of this article is on the modelling of mixture desorption kinetics. The Maxwell-Stefan (M-S) formulation of intra-crystalline diffusion is used to model the transient desorption of four different binary mixtures (N_2/CH_4, CO_2/C_2H_6, O_2/N_2, and C_3H_6/C_3H_8) in fixed beds packed with LTA-4A, DDR, CHA, or ZIF-8, that have cage-window structural topologies. The intra-crystalline flux of each species is coupled with that of partner species; the coupling effects are quantified by a 2×2 dimensional matrix of thermodynamic correction factors whose elements Γ_{ij} can be determined from the model used to describe mixture adsorption equilibrium. For desorption from a single crystallite, thermodynamic coupling effects cause transient undershoots in the loading of the more mobile component. If the Γ_{ij} are assumed to equal δ_{ij}, the Kronecker delta, no undershoots are realized. The recovery of the more mobile component during the blowdown phase of PSA operations is significantly enhanced by the off-diagonal elements of Γ_{ij}. The major conclusion to emerge from this study is that modelling of mixture desorption kinetics need to properly account for thermodynamic coupling effects.

1. Introduction

While the majority of separations in fixed-bed adsorbers, such a H_2 purification, rely on exploitation of mixture adsorption equilibria [1–8], there are a number of practical instances in which diffusional effects over-ride the influence of mixture adsorption equilibrium and are the prime driver for separations [9,10]. Examples of kinetically driven separations include production of N_2 from air, removal of N_2 from natural gas, and C_3H_6/C_3H_8 separations [2–4,11–15]. For enhancement of diffusion selectivities, the porous adsorbent materials are chosen to have restricted pore sizes [10,16,17]. Examples of such materials include LTA, CHA, DDR, ERI, and ZIF-8 that have narrow windows in the 3–4.5 Å size range. In such structures, the narrow windows allow the inter-cage hopping of only one molecule at a time; consequently, the inter-cage jumps are practically un-correlated [18–20]. For the scenario in which correlation effects are of negligible importance, the Maxwell-Stefan (M-S) formulation [19,21–24] simplifies to yield the following expression for the intra-crystalline fluxes for binary mixtures [10]

$$N_i = -\rho Đ_i \frac{q_i}{RT}\frac{\partial \mu_i}{\partial r}; \quad i = 1, 2 \tag{1}$$

In Eq. (1) R is the gas constant, T is the temperature, ρ represents the framework density of the microporous crystalline material, r is the radial distance coordinate, and the component loadings q_i are defined in terms of moles per kg of framework. The $Đ_i$ characterize and quantify the interaction between species i and pore walls. The persuasive advantage of the M-S formulation Eq. (1) is that the M-S diffusivity $Đ_i$ equals the corresponding diffusivity for a unary system, determined at the same pore occupancy [19]. Furthermore, the M-S diffusivity $Đ_i$ for any species i, in a mixture remains invariant to choice of the partner species [19,25].

The chemical potential gradients $\partial \mu_i/\partial r$ can be related to the gradients of the molar loadings, q_i, by defining thermodynamic correction factors Γ_{ij}

$$\frac{q_i}{RT}\frac{\partial \mu_i}{\partial r} = \sum_{j=1}^{2} \Gamma_{ij}\frac{\partial q_j}{\partial r}; \quad \Gamma_{ij} = \frac{q_i}{p_i}\frac{\partial p_i}{\partial q_j}; \qquad i, j = 1, 2 \tag{2}$$

The thermodynamic correction factors Γ_{ij} can be calculated by differentiation of the model describing mixture adsorption equilibrium such as the Ideal Adsorbed Solution Theory (IAST) theory [26] or the mixed-gas Langmuir model:

$$\frac{q_i}{q_{i,sat}} = \frac{b_i p_i}{1 + \sum_{j=1}^{n} b_j p_j}; \qquad i = 1, 2, ..n \tag{3}$$

E-mail address: r.krishna@contact.uva.nl.

https://doi.org/10.1016/j.seppur.2019.115790
Received 16 March 2019; Accepted 5 July 2019
Available online 08 July 2019

Nomenclature

Latin alphabet

b_i	Langmuir binding constant, Pa^{-1}
c_i	molar concentration of species i, mol m^{-3}
c_{i0}	molar concentration of species i in fluid mixture at inlet, mol m^{-3}
$Đ_i$	Maxwell-Stefan diffusivity for molecule-wall interaction, $m^2 s^{-1}$
n	number of species in the mixture, dimensionless
L	length of packed bed adsorber, m
N_i	molar flux of species i with respect to framework, mol $m^{-2} s^{-1}$
p_i	partial pressure of species i in mixture, Pa
p_t	total system pressure, Pa
q_i	component molar loading of species i, mol kg^{-1}
$q_{i,sat}$	molar loading of species i at saturation, mol kg^{-1}
q_t	total molar loading in mixture, mol kg^{-1}
$\bar{q}_i(t)$	spatial-averaged component uptake of species i, mol kg^{-1}
r	radial direction coordinate, m
r_c	radius of crystallite, m
R	gas constant, 8.314 J $mol^{-1} K^{-1}$
t	time, s
T	absolute temperature, K
v	interstitial gas velocity in packed bed, m s^{-1}
x_i	mole fraction of species i in adsorbed phase, dimensionless
z	distance along the adsorber, m

Greek alphabet

Γ_{ij}	thermodynamic factors, dimensionless
δ_{ij}	Kronecker delta, dimensionless
ε	voidage of packed bed, dimensionless
μ_i	molar chemical potential, J mol^{-1}
ρ	framework density, kg m^{-3}
τ	time, dimensionless

In Eq. (3), p_i are the component partial pressures, q_i are the component loadings defined in terms of moles per kg of framework, $q_{i,sat}$ are the saturation capacities, and b_i are Langmuir binding constants, with units of Pa^{-1}.

Combining Eqs. (1), and (2), we get

$$N_i = -\rho Đ_i \sum_{j=1}^{2} \Gamma_{ij} \frac{\partial q_j}{\partial r}; \quad i = 1, 2 \tag{4}$$

Finite magnitudes of the off-diagonal elements Γ_{ij} $(i \neq j)$ cause the flux of species i to be also influenced by the gradient of the molar loading of species j [27]. In order to appreciate the significance of such thermodynamic "coupling", Fig. 1 presents the calculations of Γ_{12}/Γ_{11}, and Γ_{21}/Γ_{22} for 50/50 $C_3H_6(1)/C_3H_8(2)$ mixture adsorption in ZIF-8 at 303 K. We note that at a total pressure of 100 kPa, the cross-coefficients are about 60% of the magnitudes of the diagonal elements, indicating that thermodynamic coupling effects may be significant.

A number of experimental [12,28–33] and theoretical investigations [9,10,24,34] have demonstrated that an important consequence of thermodynamic coupling effects is the occurrence of uphill diffusion, overshoots, and the attainment of supra-equilibrium loadings during transient *uptake* of binary mixtures in zeolites, and ZIFs. The primary objective of this article is investigate, and highlight, the strong influence of Γ_{ij} $(i \neq j)$ on the kinetics of mixture *desorption* operations in kinetically driven separation of four different mixtures: N_2/CH_4, CO_2/C_2H_6, O_2/N_2, and C_3H_6/C_3H_8. We aim to highlight the phenomena of *undershoots* during transient desorption, and draw consequences for the recovery of the more mobile partner species during the blowdown phase of PSA operations.

2. Transient undershoots during mixture desorption from crystallites

We begin by considering the transient desorption of components from spherical crystallites of radius r_c exposed to a bulk gas phase mixture maintained at constant composition and total pressure. The radial distribution of molar loadings, q_i, is obtained from a solution of a set of two differential equations

$$\rho \frac{\partial q_i(r,t)}{\partial t} = -\frac{1}{r^2}\frac{\partial}{\partial r}(r^2 N_i); \quad i = 1, 2 \tag{5}$$

The intra-crystalline fluxes N_i, in turn, are related to the radial gradients in the molar loadings by Eq. (4). Combination of Eqs. (4) and (5) results in a set of coupled differential equations that need to be solved numerically; details are provided in the Supplementary material.

At any time t, the component loadings at the surface of the particle $q_i(r_c, t) = q_i^*$ is in equilibrium with the bulk phase gas mixture. The loadings q_i^* are determined by the IAST or mixed-gas Langmuir model, as appropriate [35].

At any time t, during the transient approach to thermodynamic equilibrium, the spatial-averaged component loading within the crystallites of radius r_c is calculated using

$$\bar{q}_i(t) = \frac{3}{r_c^3}\int_0^{r_c} q_i(r,t) r^2 dr \tag{6}$$

Fig. 2a shows the component loadings of N_2 and CH_4 in LTA-4A crystal on exposure to 20/80 N_2/CH_4 gas phase mixture whose total pressure is reduced at time $t = 0$ from 100 kPa to 10 kPa. The nitrogen molecule has a "pencil-like" shape with dimensions of 4.4 Å × 3.3 Å; it can hop length-wise across the narrow 4.1 Å × 4.5 Å 8-ring windows of LTA-4A [9,20]. The methane molecule has spherical shape with dimensions of 3.7 Å; it is much more severely constrained in the window regions and has a diffusivity that is 22 times lower than that of N_2

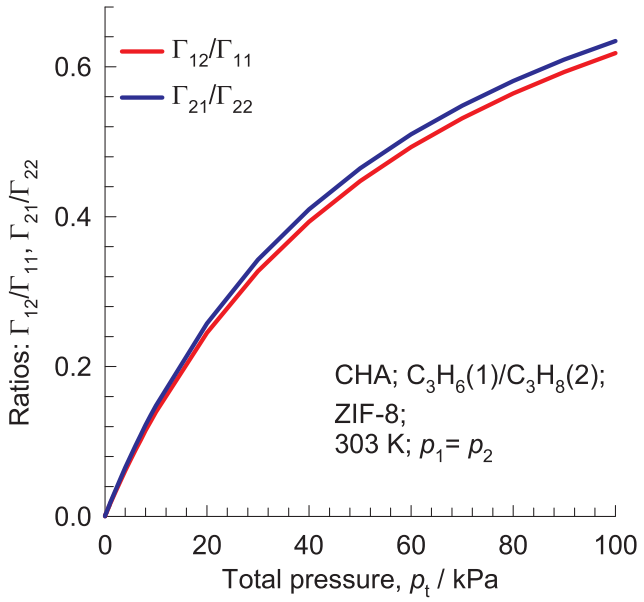

Fig. 1. Calculations of Γ_{12}/Γ_{11}, and Γ_{21}/Γ_{22} for 50/50 $C_3H_6(1)/C_3H_8(2)$ mixture adsorption within crystals of ZIF-8 at 303 K. The isotherm data are provided in Chapter 8 of Supplementary Material.

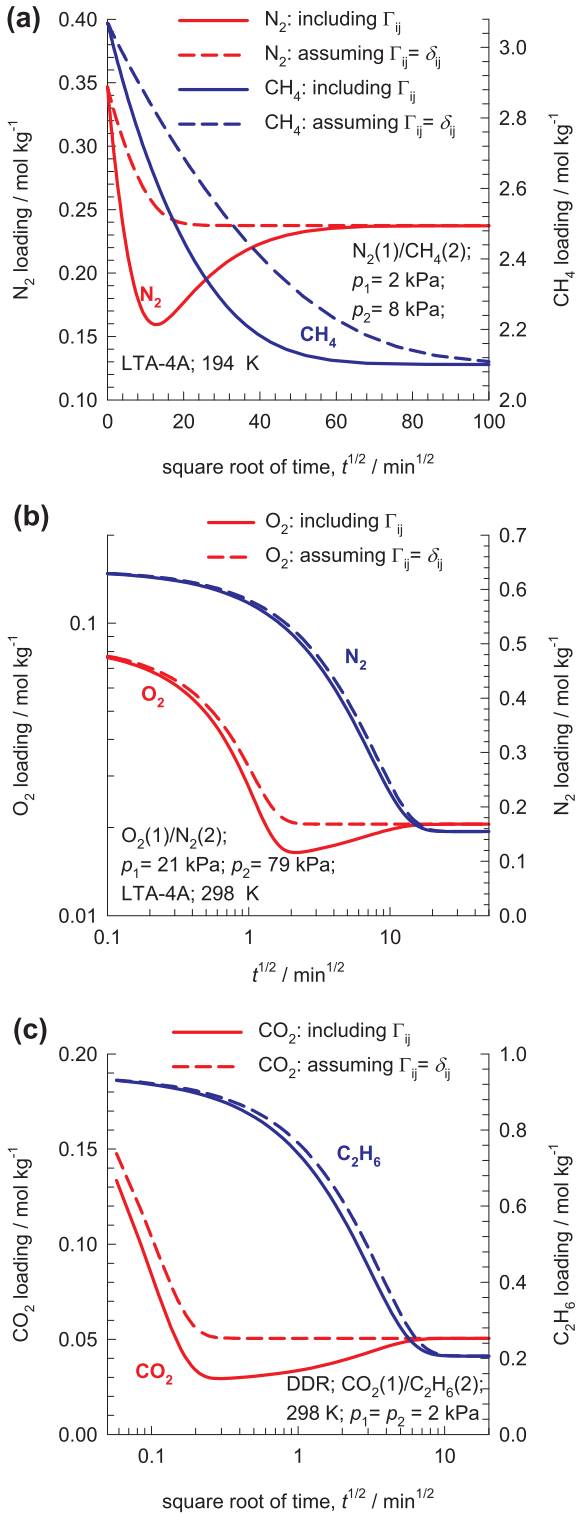

Fig. 2. (a) Transient desorption of N_2, and CH_4 in LTA-4A crystal at 194 K, exposed to 20/80 $N_2(1)/CH_4(2)$ bulk gas mixtures with total pressure reduction from 100 kPa to 10 kPa. (b) Transient desorption of O_2 and N_2 in LTA-4A crystal at 298 K, exposed to 21/79 $O_2(1)/N_2(2)$ mixtures with total pressure reduction from 600 kPa to 100 kPa. (c) Transient desorption of CO_2 and C_2H_6 in DDR zeolite at 298 K, exposed to 50/50 $CO_2(1)/C_2H_6(2)$ bulk gas mixtures with total pressure reduction from 40 kPa to 4 kPa. The continuous solid lines are simulations based on Eq. (4). The dashed lines are the simulations based on Eq. (7). Further details and input data are provided in Chapters 5, 6, and 7 of Supplementary Material.

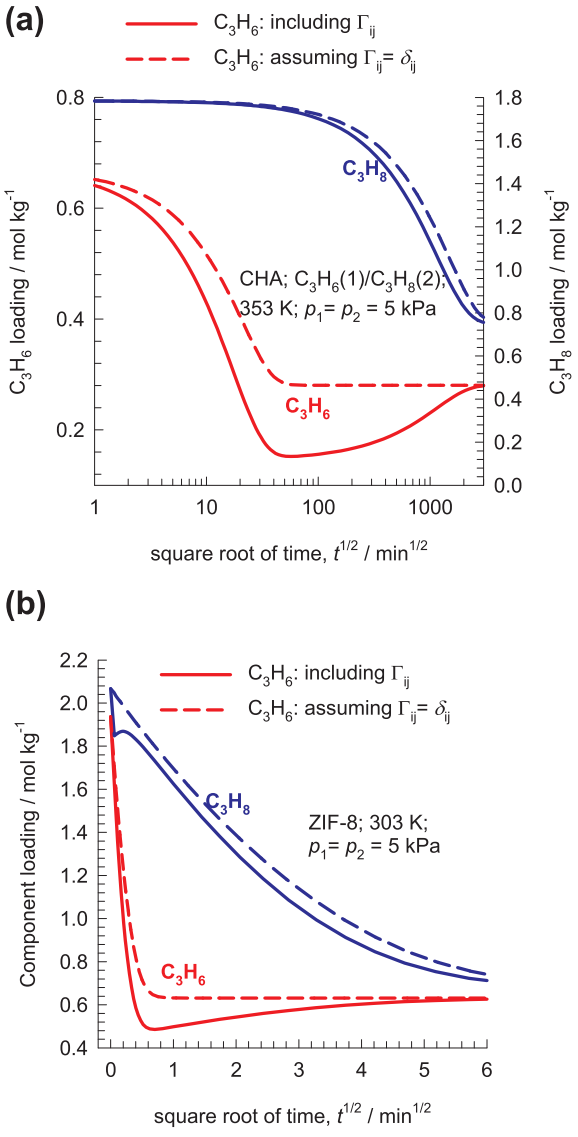

Fig. 3. (a) Transient desorption of C_3H_6 and C_3H_8 in CHA crystal at 353 K, exposed to 50/50 $C_3H_6(1)/C_3H_8(2)$ bulk gas mixtures with total pressure reduction from 100 kPa to 10 kPa. (b) Transient desorption of C_3H_6 and C_3H_8 in ZIF-8 crystal at 303 K, exposed to 50/50 $C_3H_6(1)/C_3H_8(2)$ bulk gas mixtures with total pressure reduction from 100 kPa to 10 kPa. The continuous solid lines are simulations based on Eq. (4). The dashed lines are the simulations based on Eq. (7). Further details and input data are provided in Chapter 8 of Supplementary Material.

[20,34]. The adsorption strength of CH_4 is higher than that of N_2 by a factor 2.2. The continuous solid lines, that are the simulations obtained by solving Eqs. (4) and (5), show a pronounced undershoot in the loading of the more mobile N_2 during initial transience. This undershoot signals the phenomenon of uphill diffusion, causing sub-equilibrium loadings of N_2 to be realized. If thermodynamic coupling effects are ignored (i.e. $\Gamma_{ij} = \delta_{ij}$, the Kronecker delta) and a simplified *uncoupled* flux relation

$$N_i = -\rho \text{Đ}_i \frac{\partial q_i}{\partial r}; \quad i = 1, 2. .n \tag{7}$$

is invoked, the undershoot disappears and the transient equilibration process is monotonic in nature; see dashed lines in Fig. 2a.

Fig. 2b shows the component loadings of O_2, and N_2 in LTA-4A zeolite on exposure to 21/79 O_2/N_2 bulk gas phase mixture whose total pressure is reduced at time $t = 0$ from 600 kPa to 100 kPa. The mixture

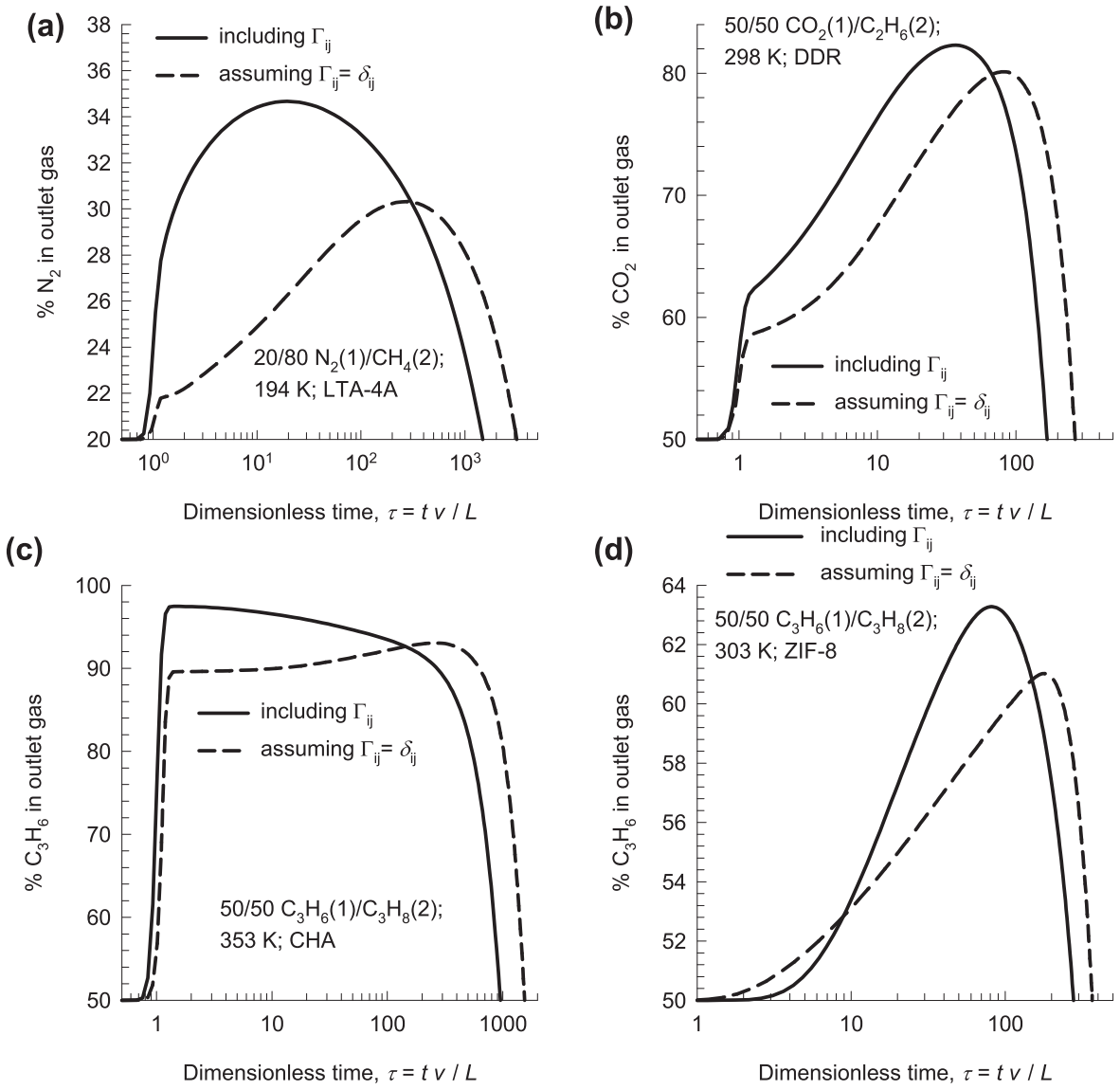

Fig. 4. Transient breakthroughs of components during co-current vacuum blowdown. (a) LTA-4A zeolite packed bed initially equilibrated with 20/80 N_2(1)/CH_4(2) feed gas mixtures at 194 K and 100 kPa. (b) DDR packed bed initially equilibrated with 50/50 CO_2(1)/C_2H_6(2) feed gas mixtures at total pressure of 40 kPa. (c) CHA zeolite packed bed initially equilibrated with 50/50 C_3H_6(1)/C_3H_8(2) feed gas mixtures at 353 K and total pressure of 100 kPa. (d) ZIF-8 packed bed initially equilibrated with 50/50 C_3H_6(1)/C_3H_8(2) feed gas mixtures at 303 K and total pressure of 100 kPa. The continuous solid lines are simulations based on Eq. (4). The dashed lines are the simulations based on Eq. (7). Further details and input data are provided in the Supplementary Material.

adsorption equilibrium is in favor of N_2 that has a higher quadrupole moment compared to O_2. Due to its smaller size, the diffusivity of O_2 is 37 times higher than that of N_2. Simulations that take due account of thermodynamic coupling effects show a pronounced undershoot in the loading of the more mobile O_2 during initial transience. If thermodynamic coupling effects are neglected, and Eq. (7) is invoked, no O_2 undershoot is experienced.

For CO_2/C_2H_6 diffusion in DDR, the adsorption equilibrium is in favor of C_2H_6 but the inter-cage hopping CO_2 across the 3.65 Å × 4.37 Å 8-ring windows of DDR occurs at a rate that is three orders of magnitude higher than for C_2H_6 [34]. During the transient desorption process, CO_2 exhibits a marked undershoot, that disappears if the simpler Equation (7) is used in the flux calculations; see Fig. 2c.

Diffusion-selective separations of C_3H_6/C_3H_8 mixtures are achievable with CHA [12], ZIF-8 [36], and KAUST-7 [37]. Due to subtle differences in bond angles and bond lengths, the diffusivity of the unsaturated alkene is significantly higher in these materials. Fig. 3(a,b) show transient desorption of C_3H_6 and C_3H_8 in (a) CHA and (b) ZIF-8 crystals, exposed to 50/50 C_3H_6(1)/C_3H_8(2) bulk gas mixtures subject to pressure reduction at time $t = 0$ from 100 kPa to 10 kPa. The more mobile C_3H_6 exhibits transient undershoots in both hosts, signaling the phenomena of uphill diffusion.

3. Simulations of vacuum blowdown operations in fixed-bed adsorbers

The phenomena of uphill diffusion and the attainment of sub-equilibrium loadings during transient desorption, as witnessed in Figs. 2 and 3, have consequences for the recovery of the more mobile components during the blowdown operations of PSA operations. To illustrate this, we performed transient breakthrough simulations in fixed bed adsorbers. For an *n*-component gas mixture flowing under plug flow conditions through a fixed bed adsorber maintained under isothermal, isobaric, conditions, the molar concentrations in the gas phase at any position and instant of time are obtained by solving the following set of partial differential equations for each of the species *i* in

the gas mixture [4,23,27]

$$\frac{\partial c_i(t,z)}{\partial t} + \frac{\partial (v(t,z)c_i(t,z))}{\partial z} + \frac{(1-\varepsilon)}{\varepsilon}\rho\frac{\partial \bar{q}_i(t,z)}{\partial t} = 0; \quad i = 1, 2, ...n \tag{8}$$

In Eq. (8), t is the time, z is the distance along the adsorber, ε is the bed voidage, v is the interstitial gas velocity, and $\bar{q}_i(t, z)$ is the *spatially averaged* molar loading within the crystallites of radius r_c, monitored at position z, and at time t; these are determined using Eq. (6) in conjunction with Eq. (4). The fixed bed of crystalline particles is considered to be initially equilibrated with co-current flow of the feed gas mixtures at a specified temperature and total pressure. At time $t = 0$ the vacuum blowdown operation commences. The numerical methodology for solving the set of partial differential equations is described in the Supplementary material.

Fig. 4a shows the % N_2 exiting the bed during vacuum blowdown of a fixed bed of LTA-4A zeolite bed that is initially equilibrated with co-current flow of 20/80 N_2/CH_4 feed gas mixtures at 194 K and 100 kPa. The x-axis is the dimensionless time, $\tau = tv/L$, obtained by dividing the actual time, t, by the characteristic time, L/v, where L is the length of adsorber. For simulations that properly account for thermodynamic coupling, based on Eq. (4), the composition of the exiting gas is richer in the more mobile N_2. If thermodynamic coupling effects are ignored, and Eq. (7) is invoked to describe the intra-crystalline fluxes, the exit gas is significantly poorer in N_2 during the early stages of blowdown operations.

Precisely analogous conclusions emerge for blowdown operations for CO_2/C_2H_6/DDR (see Fig. 4b), C_3H_6/C_3H_8/CHA (see Fig. 4c), and C_3H_6/C_3H_8/ZIF-8 (see Fig. 4d). In all cases, the inclusion of thermodynamic coupling effects results in an exit gas that is richer in the more mobile component during the initial stages of vacuum blowdown.

4. Conclusions

The Maxwell-Stefan diffusion formulation has been used to model the desorption kinetics of kinetically driven mixture separation in fixed beds of microporous crystalline adsorbents. Four different mixture separations N_2/CH_4, CO_2/C_2H_6, O_2/N_2, and C_3H_6/C_3H_8 in cage-window host structures (LTA-4A, DDR, CHA, ZIF-8) have been analyzed to highlight the influence of thermodynamic coupling. For transient desorption from single crystals, the off-diagonal elements Γ_{ij} $(i \neq j)$ engender undershoots in the loading of the more mobile partner species during early stages of equilibration. Such undershoots, signifying uphill diffusion, result in enhanced recovery of the more mobile component during the vacuum blowdown phase of PSA operations.

Appendix A. Supplementary material

Supplementary data to this article can be found online at https://doi.org/10.1016/j.seppur.2019.115790.

References

[1] D.M. Ruthven, Principles of Adsorption and Adsorption Processes, John Wiley, New York, 1984.
[2] R.T. Yang, Gas separation by Adsorption Processes, Butterworth, Boston, 1987.
[3] R.T. Yang, Adsorbents: Fundamentals and Applications, John Wiley & Sons Inc, Hoboken, New Jersey, 2003.
[4] D.M. Ruthven, S. Farooq, K.S. Knaebel, Pressure swing adsorption, VCH Publishers, New York, 1994.
[5] R. Krishna, Methodologies for screening and selection of crystalline microporous materials in mixture separations, Sep. Purif. Technol. 194 (2018) 281–300, https://doi.org/10.1016/j.seppur.2017.11.056.
[6] R. Krishna, Screening metal-organic frameworks for mixture separations in fixed-bed adsorbers using a combined selectivity/capacity metric, RSC Adv. 7 (2017) 35724–35737, https://doi.org/10.1039/C7RA07363A.
[7] R. Krishna, Methodologies for evaluation of metal-organic frameworks in separation applications, RSC Adv. 5 (2015) 52269–52295.
[8] R. Krishna, Elucidation and characterization of entropy effects in mixture separations with micro-porous crystalline adsorbents, Sep. Purif. Technol. 215 (2019) 227–241, https://doi.org/10.1016/j.seppur.2019.01.014.
[9] R. Krishna, A Maxwell-Stefan-Glueckauf description of transient mixture uptake in microporous adsorbents, Sep. Purif. Technol. 191 (2018) 392–399, https://doi.org/10.1016/j.seppur.2017.09.057.
[10] R. Krishna, Highlighting the influence of thermodynamic coupling on kinetic separations with microporous crystalline materials, ACS Omega 4 (2019) 3409–3419, https://doi.org/10.1021/acsomega.8b03480.
[11] B.R. Pimentel, R.P. Lively, Propylene enrichment via kinetic vacuum pressure swing adsorption using ZIF-8 fiber sorbents, ACS Appl. Mater. Interfaces 10 (2018) 36323–36331, https://doi.org/10.1021/acsami.8b08983.
[12] M. Khalighi, Y.F. Chen, S. Farooq, I.A. Karimi, J.W. Jiang, Propylene/propane separation using SiCHA, Ind. Eng. Chem. Res. 52 (2013) 3877–3892.
[13] S.J. Bhadra, S. Farooq, Separation of methane nitrogen mixture by pressure swing adsorption for natural gas upgrading, Ind. Eng. Chem. Res. 50 (2011) 14030–14045.
[14] A. Jayaraman, A.J. Hernandez-Maldonado, R.T. Yang, D. Chinn, C.L. Munson, D.H. Mohr, Clinoptilolites for nitrogen/methane separation, Chem. Eng. Sci. 59 (2004) 2407–2417.
[15] M. Tagliabue, D. Farrusseng, S. Valencia, S. Aguado, U. Ravon, C. Rizzo, A. Corma, C. Mirodatos, Natural gas treating by selective adsorption: Material science and chemical engineering interplay, Chem. Eng. J. 155 (2009) 553–566.
[16] R. Krishna, J.M. van Baten, A molecular dynamics investigation of the diffusion characteristics of cavity-type zeolites with 8-ring windows, Microporous Mesoporous Mater. 137 (2011) 83–91.
[17] Y. Wang, D. Zhao, Beyond equilibrium: metal–organic frameworks for molecular sieving and kinetic gas separation, Cryst. Growth Des. 17 (2017) 2291–2308.
[18] R. Krishna, J.M. van Baten, Investigating the influence of diffusional coupling on mixture permeation across porous membranes, J. Membr. Sci. 430 (2013) 113–128.
[19] R. Krishna, Occupancy dependency of Maxwell–Stefan diffusivities in ordered crystalline microporous materials, ACS Omega 3 (2018) 15743–15753, https://doi.org/10.1021/acsomega.8b02465.
[20] R. Krishna, J.M. van Baten, Using molecular dynamics simulations for elucidation of molecular traffic in ordered crystalline microporous materials, Microporous Mesoporous Mater. 258 (2018) 151–169, https://doi.org/10.1016/j.micromeso.2017.09.014.
[21] R. Krishna, Describing the diffusion of guest molecules inside porous structures, J. Phys. Chem. C 113 (2009) 19756–19781.
[22] R. Krishna, Diffusion in porous crystalline materials, Chem. Soc. Rev. 41 (2012) 3099–3118.
[23] R. Krishna, The Maxwell-Stefan description of mixture diffusion in nanoporous crystalline materials, Microporous Mesoporous Mater. 185 (2014) 30–50.
[24] R. Krishna, Diffusing uphill with James Clerk Maxwell and Josef Stefan, Chem. Eng. Sci. 195 (2019) 851–880, https://doi.org/10.1016/j.ces.2018.10.032.
[25] R. Krishna, J.M. van Baten, Onsager coefficients for binary mixture diffusion in nanopores, Chem. Eng. Sci. 63 (2008) 3120–3140.
[26] A.L. Myers, J.M. Prausnitz, Thermodynamics of mixed gas adsorption, AIChE J. 11 (1965) 121–130.
[27] R. Krishna, R. Baur, Modelling issues in zeolite based separation processes, Sep. Purif. Technol. 33 (2003) 213–254.
[28] H.W. Habgood, The Kinetics of Molecular Sieve Action. Sorption of Nitrogen-Methane Mixtures by Linde Molecular Sieve 4A, Canad. J. Chem. 36 (1958) 1384–1397.
[29] T. Titze, C. Chmelik, J. Kärger, J.M. van Baten, R. Krishna, Uncommon synergy between adsorption and diffusion of hexane isomer mixtures in MFI zeolite induced by configurational entropy effects, J. Phys. Chem. C 118 (2014) 2660–2665.
[30] J.C. Saint-Remi, G.V. Baron, J.F.M. Denayer, Non-uniform chain length dependent diffusion of short 1-alcohols in SAPO-34 in liquid phase, J. Phys. Chem. C 117 (2013) 9758–9765.
[31] T. Binder, A. Lauerer, C. Chmelik, J. Haase, J. Kärger, D.M. Ruthven, Micro-imaging of transient intracrystalline concentration profiles during two-component uptake of light hydrocarbon - carbon dioxide mixtures by DDR-type zeolites, Ind. Eng. Chem. Res. 54 (2015) 8997–9004.
[32] A. Lauerer, T. Binder, C. Chmelik, E. Miersemann, J. Haase, D.M. Ruthven, J. Kärger, Uphill diffusion and overshooting in the adsorption of binary mixtures in nanoporous solids, Nat. Commun. 6 (2015) 7697, https://doi.org/10.1038/ncomms8697.
[33] B. Majumdar, S.J. Bhadra, R.P. Marathe, S. Farooq, Adsorption and diffusion of methane and nitrogen in barium exchanged ETS-4, Ind. Eng. Chem. Res. 50 (2011) 3021–3034.
[34] R. Krishna, Tracing the origins of transient overshoots for binary mixture diffusion in microporous crystalline materials, Phys. Chem. Chem. Phys. 18 (2016) 15482–15495.
[35] R. Krishna, J.R. Long, Screening metal-organic frameworks by analysis of transient breakthrough of gas mixtures in a fixed bed adsorber, J. Phys. Chem. C 115 (2011) 12941–12950.
[36] U. Böhme, B. Barth, C. Paula, A. Kuhnt, W. Schwieger, A. Mundstock, J. Caro, M. Hartmann, Ethene/ethane and propene/propane separation via the olefin and paraffin selective metal–organic framework adsorbents CPO-27 and ZIF-8, Langmuir 29 (2013) 8592–8600.
[37] A. Cadiau, K. Adil, P.M. Bhatt, Y. Belmabkhout, M. Eddaoudi, A metal-organic framework-based splitter for separating propylene from propane, Science 353 (2016) 137–140.

Supplementary Material

Maxwell-Stefan Modelling of Mixture Desorption Kinetics in Microporous Crystalline Materials

Rajamani Krishna

Van 't Hoff Institute for Molecular Sciences

University of Amsterdam

Science Park 904

1098 XH Amsterdam, The Netherlands

email: r.krishna@contact.uva.nl

Table of Contents

1 Preamble

This Supplementary Material accompanying the article *Maxwell-Stefan Modelling of Mixture Desorption Kinetics in Microporous Crystalline Materials* provides:

(a) Brief summary of the Ideal Adsorbed Solution theory for calculation of mixture adsorption equilibrium, along with derivations of the mixed-gas Langmuir model

(b) Brief summary of the Maxwell-Stefan theory of diffusion in microporous materials

(c) Methodology adopted for numerical solutions to transient uptake within single crystalline particle

(d) Methodology used for transient breakthroughs in fixed bed adsorbers, incorporating the Maxwell-Stefan description of intra-particle diffusion

(e) Four different case studies illustrating kinetic separations of CO_2/C_2H_6, N_2/CH_4, O_2/N_2, and C_3H_6/C_3H_8 mixtures. Simulation details and input data on pure component isotherms, and Maxwell-Stefan diffusivities are provided for each of the four case studies.

For ease of reading, the Supplementary Material is written as a stand-alone document.

2 The Ideal Adsorbed Solution Theory (IAST)

A brief summary of the IAST theory is provided in order to facilitate comparisons with the statistical thermodynamics based models to be discussed later in this article.

2.1 Brief outline of theory

Within microporous crystalline materials, the guest molecules exist in the adsorbed phase. The Gibbs adsorption equation[1] in differential form is

$$Ad\pi = \sum_{i=1}^{n} q_i d\mu_i \tag{S-1}$$

The quantity A is the surface area per kg of framework, with units of m^2 per kg of the framework of the crystalline material; q_i is the molar loading of component i in the adsorbed phase with units moles per kg of framework; μ_i is the molar chemical potential of component i. The spreading pressure π has the same units as surface tension, i.e. N m^{-1}.

The chemical potential of any component in the adsorbed phase, μ_i, equals that in the bulk fluid phase. If the partial fugacities in the bulk fluid phase are f_i, we have

$$d\mu_i = RTd\ln f_i \tag{S-2}$$

where R is the gas constant (= 8.314 J mol^{-1} K^{-1}).

Briefly, the basic equation of Ideal Adsorbed Solution Theory (IAST) theory of Myers and Prausnitz[2] is the analogue of Raoult's law for vapor-liquid equilibrium, i.e.

$$f_i = P_i^0 x_i; \quad i = 1,2,...n \tag{S-3}$$

where x_i is the mole fraction in the adsorbed phase

$$x_i = \frac{q_i}{q_1 + q_2 + ...q_n} \tag{S-4}$$

and P_i^0 is the pressure for sorption of every component *i*, which yields the same spreading pressure, π for each of the pure components, as that for the mixture:

$$\frac{\pi A}{RT} = \int_0^{P_1^0} \frac{q_1^0(f)}{f} df = \int_0^{P_2^0} \frac{q_2^0(f)}{f} df = \int_0^{P_3^0} \frac{q_3^0(f)}{f} df = ... \tag{S-5}$$

where $q_i^0(f)$ is the *pure* component adsorption isotherm. The units of $\frac{\pi A}{RT}$, also called the adsorption potential,[3] are mol kg^{-1}.

The unary isotherm may be described by say the 1-site Langmuir isotherm

$$q^0(f) = q_{sat} \frac{bf}{1+bf}; \quad \theta = \frac{bf}{1+bf} \tag{S-6}$$

where we define the fractional *occupancy* of the adsorbate molecules, $\theta = q^0(f)/q_{sat}$. The superscript 0 is used to emphasize that $q^0(f)$ relates the *pure component* loading to the bulk fluid fugacity. More generally, the unary isotherms may need to be described by, say, the dual-Langmuir-Freundlich model

$$q^0(f) = q_{A,sat} \frac{b_A f^{\nu A}}{1+b_A f^{\nu A}} + q_{B,sat} \frac{b_B f^{\nu B}}{1+b_B f^{\nu B}} \tag{S-7}$$

or the 3-site Langmuir-Freundlich model:

$$q^0 = q_{A,sat} \frac{b_A f^{\nu_A}}{1+b_A f^{\nu_A}} + q_{B,sat} \frac{b_B f^{\nu_B}}{1+b_B f^{\nu_B}} + q_{C,sat} \frac{b_C f^{\nu_C}}{1+b_C f^{\nu_C}} \tag{S-8}$$

Each of the integrals in Equation (S-5) can be evaluated analytically. For the 3-site Langmuir-Freundlich isotherm, for example, the integration yields for component *i*,

$$\begin{aligned} \int_{f=0}^{P_i^0} \frac{q^0(f)}{f} df &= \frac{q_{A,sat}}{\nu_A} \ln\left(1+b_A\left(P_i^0\right)^{\nu_A}\right) + \frac{q_{B,sat}}{\nu_B} \ln\left(1+b_B\left(P_i^0\right)^{\nu_B}\right) + \frac{q_{C,sat}}{\nu_C} \ln\left(1+b_C\left(P_i^0\right)^{\nu_C}\right) \\ \int_{f=0}^{P_i^0} \frac{q^0(f)}{f} df &= \frac{q_{A,sat}}{\nu_A} \ln\left(1+b_A\left(\frac{f_i}{x_i}\right)^{\nu_A}\right) + \frac{q_{B,sat}}{\nu_B} \ln\left(1+b_B\left(\frac{f_i}{x_i}\right)^{\nu_B}\right) + \frac{q_{C,sat}}{\nu_C} \ln\left(1+b_C\left(\frac{f_i}{x_i}\right)^{\nu_C}\right) \end{aligned} \tag{S-9}$$

The right hand side of equation (S-9) is a function of P_i^0. For multicomponent mixture adsorption, each of the equalities on the right hand side of Equation (S-5) must be satisfied. These constraints may

be solved using a suitable equation solver, to yield the set of values of P_1^0, P_2^0, P_3^0,.. P_n^0, all of which satisfy Equation (S-5). The corresponding values of the integrals using these as upper limits of integration must yield the same value of $\frac{\pi A}{RT}$ for each component; this ensures that the obtained solution is the correct one.

The adsorbed phase mole fractions x_i are then determined from

$$x_i = \frac{f_i}{P_i^0}; \quad i = 1,2,...n \tag{S-10}$$

A key assumption of the IAST is that the enthalpies and surface areas of the adsorbed molecules do not change upon mixing. If the total mixture loading is q_t, the area covered by the adsorbed mixture is $\frac{A}{q_t}$ with units of m^2 (mol mixture)$^{-1}$. Therefore, the assumption of no surface area change due to mixture adsorption translates as $\frac{A}{q_t} = \frac{Ax_1}{q_1^0\left(P_1^0\right)} + \frac{Ax_2}{q_2^0\left(P_2^0\right)} + \cdots \frac{Ax_n}{q_n^0\left(P_n^0\right)}$; the total mixture loading is q_t is calculated from

$$q_t = q_1 + q_2 ... + q_n = \frac{1}{\frac{x_1}{q_1^0(P_1^0)} + \frac{x_2}{q_2^0(P_2^0)} + ... + \frac{x_n}{q_n^0(P_n^0)}} \tag{S-11}$$

in which $q_1^0(P_1^0)$, $q_2^0(P_2^0)$,… $q_n^0(P_n^0)$ are determined from the unary isotherm fits, using the sorption pressures for each component P_1^0, P_2^0, P_3^0,.. P_n^0 that are available from the solutions to equations Equations (S-5), and (S-9).

The entire set of equations (S-3) to (S-11) need to be solved numerically to obtain the loadings, q_i of the individual components in the mixture.

2.2 IAST model: 1-site Langmuir isotherms

The IAST procedure for will be explained in a step-by-step manner for binary mixture adsorption in which the unary isotherms are described by the 1-site Langmuir model. The objective is to determine the molar loadings, q_1, and q_2, in the adsorbed phase.

Performing the integration of Equation (S-5) results in an expression relating the sorption pressures P_i^0 of the two species

$$\begin{aligned}&\frac{\pi A}{RT} = q_{1,sat}\ln\left(1+b_1P_1^0\right) = q_{2,sat}\ln\left(1+b_2P_2^0\right)\\ &b_1P_1^0 = \exp\left(\frac{\pi A}{q_{1,sat}RT}\right)-1; \quad b_2P_2^0 = \exp\left(\frac{\pi A}{q_{2,sat}RT}\right)-1\end{aligned} \tag{S-12}$$

The adsorbed phase mole fractions of component 1, and component 2 are given by equation (S-10)

$$x_1 = \frac{f_1}{P_1^0}; \quad x_2 = 1-x_1 = \frac{f_2}{P_2^0} \tag{S-13}$$

Since the mole fractions add to unity, we may combine equations (S-12), and (S-13) to obtain a relation in just *one* unknown, x_1:

$$\frac{\pi A}{RT} = q_{1,sat}\ln\left(1+b_1\frac{f_1}{x_1}\right) = q_{2,sat}\ln\left(1+b_2\frac{f_2}{1-x_1}\right) \tag{S-14}$$

Equation (S-14) is a non-linear equation

$$q_{1,sat}\ln\left(1+b_1\frac{f_1}{x_1}\right) - q_{2,sat}\ln\left(1+b_2\frac{f_2}{1-x_1}\right) = 0 \tag{S-15}$$

The partial fugacities of the two components in the bulk gas phase are known, and equation (S-15) needs to be solved using a root finder to solve for the unknown, x_1. Once x_1, and $x_2 = 1-x_1$ are determined, the sorption pressures can be calculated:

$$P_1^0 = \frac{f_1}{x_1}; \quad P_2^0 = \frac{f_2}{x_2} = \frac{f_2}{1-x_1} \tag{S-16}$$

The total amount adsorbed, $q_t = q_1 + q_2$ can be calculated from

$$q_t = q_1 + q_2 = \frac{1}{\frac{x_1}{q_1^0(P_1^0)} + \frac{x_2}{q_2^0(P_2^0)}} \tag{S-17}$$

in which $q_1^0(P_1^0)$, and $q_2^0(P_2^0)$ are determined from the Langmuir parameters along with the sorption pressures, determined from equation (S-16). The component loadings, q_1, and q_2 are then determined from $q_1 = q_t x_1; \quad q_2 = q_t(1 - x_1)$.

2.3 Langmuir isotherms with equal saturation capacities

For the special case of binary mixture adsorption with equal saturation capacities, $q_{1,sat} = q_{2,sat} = q_{sat}$, the component loadings can be determined explicitly. Equation (S-15) can be solved explicitly to obtain the adsorbed phase mole fractions

$$\frac{x_1}{x_2} = \frac{q_1}{q_2} = \frac{b_1 f_1}{b_2 f_2}; \quad x_1 = \frac{q_1}{q_t} = \frac{b_1 f_1}{b_1 f_1 + b_2 f_2}; \quad x_2 = \frac{q_2}{q_t} = \frac{b_2 f_2}{b_1 f_1 + b_2 f_2} \tag{S-18}$$

Equation (S-12) simplifies to yield

$$\begin{aligned} &\frac{\pi A}{RT} = q_{sat} \ln\left(1 + b_1 P_1^0\right) = q_{sat} \ln\left(1 + b_2 P_2^0\right) \\ &b_1 P_1^0 = b_2 P_2^0 = \exp\left(\frac{\pi A}{q_{sat} RT}\right) - 1 = \exp\left(\frac{\pi A}{q_{sat} RT}\right) - 1 \end{aligned} \tag{S-19}$$

From equation (S-16) we get

$$\begin{aligned} &b_i P_1^0 = \frac{b_1 f_1}{x_1} = b_2 P_2^0 = \frac{b_2 f_2}{x_2} = b_1 f_1 + b_2 f_2 \\ &1 + b_i P_1^0 = 1 + b_2 P_2^0 = 1 + b_1 f_1 + b_2 f_2 \end{aligned} \tag{S-20}$$

Equations (S-17), (S-18), (S-19), and (S-20) yield

$$\begin{aligned} &\frac{q_{sat}}{q_t} = \frac{x_1}{b_1 P_1^0}\left(1 + b_1 P_1^0\right) + \frac{x_2}{b_2 P_2^0}\left(1 + b_2 P_2^0\right) = \frac{1 + b_1 f_1 + b_2 f_2}{b_1 f_1 + b_2 f_2} \\ &q_t = q_{sat} \frac{b_1 f_1 + b_2 f_2}{1 + b_1 f_1 + b_2 f_{22}} \end{aligned} \tag{S-21}$$

Combining equations (S-18), and (S-21) we obtain the following explicit expressions for the component loadings, and fractional occupancies

$$\theta_1 = \frac{q_1}{q_{sat}} = \frac{b_1 f_1}{1 + b_1 f_1 + b_2 f_2}; \quad \theta_2 = \frac{q_2}{q_{sat}} = \frac{b_2 f_2}{1 + b_1 f_1 + b_2 f_2} \tag{S-22}$$

Equation (S-22) is commonly referred to as the mixed-gas Langmuir model, or extended Langmuir model. Rao and Sircar[4] show that the mixed-gas Langmuir model described by Equation (S-22) passes the thermodynamic consistency test only when the saturation capacities equal each other, i.e. $q_{1,sat} = q_{2,sat}$.

From Equation (S-22), it also follows that the adsorbed phase mole fraction is

$$x_1 = \frac{1}{1 + \frac{b_2 f_2}{b_1 f_1}} \tag{S-23}$$

3 Diffusion in Microporous Crystalline Materials

3.1 The Maxwell-Stefan (M-S) description of diffusion

Within micro-porous crystalline materials, such as zeolites, metal-organic frameworks (MOFs), and zeolitic imidazolate frameworks (ZIFs), the guest molecules exist in the adsorbed phase. The Maxwell-Stefan (M-S) equations for *n*-component diffusion in porous materials is applied in the following manner[5-12]

$$\begin{aligned}
-\frac{\partial \mu_1}{\partial r} &= \frac{RT}{Đ_{12}} x_2 \left(u_1 - u_2\right) + \frac{RT}{Đ_{13}} x_3 \left(u_1 - u_3\right) + \ldots + \frac{RT}{Đ_1}\left(u_1\right) \\
-\frac{\partial \mu_2}{\partial r} &= \frac{RT}{Đ_{21}} x_1 \left(u_2 - u_1\right) + \frac{RT}{Đ_{23}} x_3 \left(u_2 - u_3\right) + \ldots + \frac{RT}{Đ_2}\left(u_2\right) \\
&\cdots\cdots \\
-\frac{\partial \mu_n}{\partial r} &= \frac{RT}{Đ_{n1}} x_1 \left(u_n - u_1\right) + \frac{RT}{Đ_{n2}} x_2 \left(u_n - u_3\right) + \ldots + \frac{RT}{Đ_n}\left(u_n\right)
\end{aligned} \tag{S-24}$$

The left members of equation (S-24) are the negative of the gradients of the chemical potentials, with the units N mol^{-1}; it represents the driving force acting per mole of species 1, 2, 3,..*n*. The u_i represents the velocity of motion of the adsorbate, defined in a reference frame with respect to the framework material. The crystalline framework is considered to be stationary. The term $RT/Đ_i$ is interpreted as the drag or friction coefficient between the guest species *i* and the pore wall. The term $RT/Đ_{ij}$ is interpreted as the friction coefficient for the *i-j* pair of guest molecules. The multiplier $x_i = q_i / q_t$ where q_i is the molar loading of adsorbate, and q_t is the *total* mixture loading $q_t = \sum_{i=1}^{n} q_i$. We expect the friction to be dependent on the number of molecules of *j* relative to that of component *i*.

An important, persuasive, argument for the use of the M-S formulation for mixture diffusion is that the M-S diffusivity $Đ_i$ in mixtures can be estimated using information on the loading dependence of the

corresponding unary diffusivity values. Put another way, the M-S diffusivity $Đ_i$ can be estimated from experimental data on *unary* diffusion in the porous material.

The M-S diffusivity $Đ_{ij}$ has the units m^2 s^{-1} and the physical significance of an *inverse* drag coefficient. The magnitudes of the M-S diffusivities $Đ_{ij}$ do not depend on the choice of the mixture reference velocity because equation (S-24) is set up in terms of velocity differences. At the molecular level, the $Đ_{ij}$ reflect how the facility for transport of species *i correlates* with that of species *j*; they are also termed *exchange coefficients*.

For *meso*porous materials with pores in the 20 Å to 100 Å size range the values of the exchange coefficient $Đ_{12}$ are the nearly the same as the binary *fluid phase* M-S diffusivity, $Đ_{12,fl}$, over the entire range of pore concentrations.[7, 8, 12-14] For micro-porous materials, the exchange coefficient $Đ_{12}$ cannot be directly identified with the corresponding fluid phase diffusivity $Đ_{12,fl}$ because the molecule-molecule interactions are also significantly influenced by molecule-wall interactions.

The Maxwell-Stefan diffusion formulation (S-24) is consistent with the theory of irreversible thermodynamics. The Onsager Reciprocal Relations imply that the M-S pair diffusivities are symmetric

$$Đ_{ij} = Đ_{ji} \tag{S-25}$$

We define N_i as the number of moles of species *i* transported per m^2 of crystalline material per second

$$N_i \equiv \rho q_i u_i \tag{S-26}$$

where ρ is the framework density with units of kg m^{-3}. Multiplying both sides of equation (S-24) by ρq_i, the M-S equations for *n*-component diffusion in zeolites, MOFs, and ZIFs take the form [13, 15, 16]

$$-\rho \frac{q_i}{RT}\frac{\partial \mu_i}{\partial r} = \sum_{\substack{j=1 \\ j\neq i}}^{n} \frac{x_j N_i - x_i N_j}{Đ_{ij}} + \frac{N_i}{Đ_i}; \qquad i = 1, 2, ..n \tag{S-27}$$

The fluxes N_i in equations (S-27) are defined in terms of the moles transported per m^2 of the *total surface of crystalline material*.

3.2 Thermodynamic correction factors

At thermodynamic equilibrium, the chemical potential of component *i* in the bulk fluid mixture equals the chemical potential of that component in the adsorbed phase. For the bulk fluid phase mixture we have

$$\frac{1}{RT}\frac{\partial \mu_i}{\partial r} = \frac{\partial \ln f_i}{\partial r} = \frac{1}{f_i}\frac{\partial f_i}{\partial r}; \qquad i = 1, 2, ..n \tag{S-28}$$

The chemical potential gradients $\partial \mu_i / \partial r$ can be related to the gradients of the molar loadings, q_i, by defining thermodynamic correction factors Γ_{ij}

$$\frac{q_i}{RT}\frac{\partial \mu_i}{\partial r} = \sum_{j=1}^{n} \Gamma_{ij}\frac{\partial q_j}{\partial r}; \quad \Gamma_{ij} = \frac{q_i}{f_i}\frac{\partial f_i}{\partial q_j}; \qquad i, j = 1, ...n \tag{S-29}$$

The thermodynamic correction factors Γ_{ij} can be calculated by differentiation of the model describing mixture adsorption equilibrium. Generally speaking, the Ideal Adsorbed Solution Theory (IAST) of Myers and Prausnitz[2] is the preferred method for estimation of mixture adsorption equilibrium. In some special case, the mixed-gas Langmuir model

$$\frac{q_i}{q_{i,sat}} = \theta_i = \frac{b_i f_i}{1 + \sum_{i=1}^{n} b_i f_i}; \quad i = 1, 2, ...n \tag{S-30}$$

may be of adequate accuracy. Analytic differentiation of equation (S-30) yields

$$\Gamma_{ij} = \delta_{ij} + \left(\frac{q_{i,sat}}{q_{j,sat}}\right)\left(\frac{\theta_i}{\theta_V}\right); \quad i, j = 1, 2 \ldots n \tag{S-31}$$

where the fractional vacancy θ_V is defined as

$$\theta_V = 1 - \theta_t = 1 - \sum_{i=1}^{n} \theta_i \tag{S-32}$$

The elements of the matrix of thermodynamic factors Γ_{ij} can be calculated explicitly from information on the component loadings q_i in the adsorbed phase; this is the persuasive advantage of the use of the

mixed-gas Langmuir model. By contrast, the IAST does not allow the calculation of Γ_{ij} explicitly from knowledge on the component loadings q_i in the adsorbed phase; a numerical procedure is required.

3.3 Explicit expression for the fluxes as function of loading gradients

By defining an n-dimensional square matrix $[B]$ with elements

$$B_{ii} = \frac{1}{Đ_i} + \sum_{\substack{j=1 \\ j\neq i}}^{n} \frac{x_j}{Đ_{ij}}; \qquad B_{ij} = -\frac{x_i}{Đ_{ij}}; \quad i, j = 1,2....n \tag{S-33}$$

we can recast equation (S-27) into the following form

$$-\rho \frac{q_i}{RT}\frac{\partial \mu_i}{\partial r} = \sum_{j=1}^{n} B_{ij} N_j; \qquad i = 1,2,..n \tag{S-34}$$

Equation (S-34) can be re-written in n-dimensional matrix notation as

$$(N) = -\rho \left[B\right]^{-1} \left[\Gamma\right] \frac{\partial (q)}{\partial r} = -\rho \left[\Lambda\right]\left[\Gamma\right] \frac{\partial (q)}{\partial r} \tag{S-35}$$

We denote the inverse of $[B]$ as $\left[\Lambda\right]$:

$$[B]^{-1} \equiv \left[\Lambda\right] \tag{S-36}$$

Compliance with the Onsager Reciprocal Relations demands

$$n_j \Lambda_{ij} = n_i \Lambda_{ji}; \quad i, j = 1, 2, ...n \tag{S-37}$$

If the correlation effects are considered to be of negligible importance, the first term on the right of equations (S-27) may be ignored; this results in a simplified set of equations

$$N_i = -\rho Đ_i \sum_{j=1}^{n} \Gamma_{ij} \frac{\partial q_j}{\partial r}; \qquad i = 1, 2..n \tag{S-38}$$

Furthermore, if the thermodynamic coupling effects are also ignored, Equation (S-38) degenerates to a set of uncoupled flux relations

$$N_i = -\rho Đ_i \frac{\partial q_i}{\partial r}; \qquad i = 1, 2..n \tag{S-39}$$

3.4 M-S formulation for binary mixture diffusion

For binary mixture diffusion inside microporous crystalline materials the Maxwell-Stefan equations (S-27) are written

$$\begin{aligned} -\rho\frac{q_1}{RT}\frac{\partial\mu_1}{\partial r} &= \frac{x_2N_1 - x_1N_2}{Đ_{12}} + \frac{N_1}{Đ_1} \\ -\rho\frac{q_2}{RT}\frac{\partial\mu_2}{\partial r} &= \frac{x_1N_2 - x_2N_1}{Đ_{12}} + \frac{N_2}{Đ_2} \end{aligned} \tag{S-40}$$

The first members on the right hand side of Equation (S-40) are required to quantify slowing-down effects that characterize binary mixture diffusion.[7, 8, 17] There is no experimental technique for direct determination of the exchange coefficients $Đ_{12}$, that quantify molecule-molecule interactions.

In two-dimensional matrix notation, equation (S-29) take the form

$$-\begin{pmatrix} \frac{q_1}{RT}\frac{\partial\mu_1}{\partial r} \\ \frac{q_2}{RT}\frac{\partial\mu_2}{\partial r} \end{pmatrix} = [\Gamma]\begin{pmatrix} \frac{\partial q_1}{\partial r} \\ \frac{\partial q_2}{\partial r} \end{pmatrix} \tag{S-41}$$

For the mixed-gas Langmuir model, equation (S-30), we can derive simple analytic expressions for the four elements of the matrix of thermodynamic factors:[18]

$$\begin{bmatrix} \Gamma_{11} & \Gamma_{12} \\ \Gamma_{21} & \Gamma_{22} \end{bmatrix} = \frac{1}{1-\theta_1-\theta_2}\begin{bmatrix} 1-\theta_2 & \frac{q_{1,sat}}{q_{2,sat}}\theta_1 \\ \frac{q_{2,sat}}{q_{1,sat}}\theta_2 & 1-\theta_1 \end{bmatrix} \tag{S-42}$$

where the fractional occupancies, θ_i, are defined by equation (S-30).

Let us define the square matrix $[B]$

$$[B] = \begin{bmatrix} \frac{1}{Đ_1}+\frac{x_2}{Đ_{12}} & -\frac{x_1}{Đ_{12}} \\ -\frac{x_2}{Đ_{12}} & \frac{1}{Đ_2}+\frac{x_1}{Đ_{12}} \end{bmatrix}; \quad [B]^{-1} = \frac{1}{1+\frac{x_1Đ_2}{Đ_{12}}+\frac{x_2Đ_1}{Đ_{12}}}\begin{bmatrix} Đ_1\left(1+\frac{x_1Đ_2}{Đ_{12}}\right) & \frac{x_1Đ_1Đ_2}{Đ_{12}} \\ \frac{x_2Đ_1Đ_2}{Đ_{12}} & Đ_2\left(1+\frac{x_2Đ_1}{Đ_{12}}\right) \end{bmatrix} \tag{S-43}$$

In proceeding further, it is convenient to define a 2×2 dimensional square matrix $[\Lambda]$:

$$[\Lambda]=\begin{bmatrix} \frac{1}{Đ_1}+\frac{x_2}{Đ_{12}} & -\frac{x_1}{Đ_{12}} \\ -\frac{x_2}{Đ_{12}} & \frac{1}{Đ_2}+\frac{x_1}{Đ_{12}} \end{bmatrix}^{-1}=\frac{1}{1+\frac{x_1Đ_2}{Đ_{12}}+\frac{x_2Đ_1}{Đ_{12}}}\begin{bmatrix} Đ_1\left(1+\frac{x_1Đ_2}{Đ_{12}}\right) & \frac{x_1Đ_1Đ_2}{Đ_{12}} \\ \frac{x_2Đ_1Đ_2}{Đ_{12}} & Đ_2\left(1+\frac{x_2Đ_1}{Đ_{12}}\right) \end{bmatrix} \tag{S-44}$$

Equation (S-40) can be re-cast into 2-dimensional matrix notation

$$(N)=-\rho[\Lambda][\Gamma]\frac{\partial(q)}{\partial r};$$

$$\begin{pmatrix} N_1 \\ N_2 \end{pmatrix}=-\frac{\rho}{1+\frac{x_1Đ_2}{Đ_{12}}+\frac{x_2Đ_1}{Đ_{12}}}\begin{bmatrix} Đ_1\left(1+\frac{x_1Đ_2}{Đ_{12}}\right) & \frac{x_1Đ_1Đ_2}{Đ_{12}} \\ \frac{x_2Đ_1Đ_2}{Đ_{12}} & Đ_2\left(1+\frac{x_2Đ_1}{Đ_{12}}\right) \end{bmatrix}\begin{bmatrix} \Gamma_{11} & \Gamma_{12} \\ \Gamma_{21} & \Gamma_{22} \end{bmatrix}\begin{pmatrix} \frac{\partial q_1}{\partial r} \\ \frac{\partial q_2}{\partial r} \end{pmatrix} \tag{S-45}$$

The elements of $[B]$ can be obtained by inverting the matrix $[\Lambda]$:

$$\begin{bmatrix} B_{11} & B_{12} \\ B_{21} & B_{22} \end{bmatrix}=\begin{bmatrix} \frac{1}{Đ_1}+\frac{x_2}{Đ_{12}} & -\frac{x_1}{Đ_{12}} \\ -\frac{x_2}{Đ_{12}} & \frac{1}{Đ_2}+\frac{x_1}{Đ_{12}} \end{bmatrix}=[\Lambda]^{-1} \tag{S-46}$$

A 2×2 dimensional Fick diffusivity matrix $[D]$ is defined as the product of $[\Lambda]$ and the matrix of thermodynamic correction factors $[\Gamma]$:

$$[D]=[B]^{-1}[\Gamma]=\frac{1}{1+\frac{x_1Đ_2}{Đ_{12}}+\frac{x_2Đ_1}{Đ_{12}}}\begin{bmatrix} Đ_1\left(1+\frac{x_1Đ_2}{Đ_{12}}\right) & \frac{x_1Đ_1Đ_2}{Đ_{12}} \\ \frac{x_2Đ_1Đ_2}{Đ_{12}} & Đ_2\left(1+\frac{x_2Đ_1}{Đ_{12}}\right) \end{bmatrix}\begin{bmatrix} \Gamma_{11} & \Gamma_{12} \\ \Gamma_{21} & \Gamma_{22} \end{bmatrix} \tag{S-47}$$

$$(N)=-\rho[D]\frac{\partial(q)}{\partial r};$$

3.5 Negligible correlations scenario for M-S diffusivities

For values of $Đ_1/Đ_{12}\to 0$, and $Đ_2/Đ_{12}\to 0$, the contribution of the first right member of M-S Equation (S-40) can be ignored and correlations can be considered to be of negligible importance; we derive

$$\frac{Đ_1}{Đ_{12}} \to 0; \quad \frac{Đ_2}{Đ_{12}} \to 0; \quad \begin{bmatrix} \Lambda_{11} & \Lambda_{12} \\ \Lambda_{21} & \Lambda_{22} \end{bmatrix} \to \begin{bmatrix} Đ_1 & 0 \\ 0 & Đ_2 \end{bmatrix}$$

$$\begin{pmatrix} N_1 \\ N_2 \end{pmatrix} = -\rho \begin{bmatrix} Đ_1 & 0 \\ 0 & Đ_2 \end{bmatrix} \begin{bmatrix} \Gamma_{11} & \Gamma_{12} \\ \Gamma_{21} & \Gamma_{22} \end{bmatrix} \begin{pmatrix} \frac{\partial q_1}{\partial r} \\ \frac{\partial q_2}{\partial r} \end{pmatrix} \tag{S-48}$$

Equation (S-48) is valid, as a first approximation, for diffusion in cage-type zeolites with 8-ring windows (CHA, LTA, DDR, ERI) and ZIF-8; see Figure S-1, ane also earlier publications.[9, 13, 19-24]

When correlation effects are negligible, the diffusional coupling effects are solely traceable to mixture adsorption thermodynamics, embodied in the matrix $[\Gamma]$.

If the mixed-gas Langmuir model is used to describe mixture adsorption equilibrium, the matrix of thermodynamic correction factors is given by Equation (S-42). Combining equations (S-42)., and (S-48) we obtain the flux expression

$$\begin{pmatrix} N_1 \\ N_2 \end{pmatrix} = -\rho \begin{bmatrix} Đ_1 & 0 \\ 0 & Đ_2 \end{bmatrix} \frac{1}{1-\theta_1-\theta_2} \begin{bmatrix} 1-\theta_2 & \frac{q_{1,sat}}{q_{2,sat}}\theta_1 \\ \frac{q_{2,sat}}{q_{1,sat}}\theta_2 & 1-\theta_1 \end{bmatrix} \begin{pmatrix} \frac{\partial q_1}{\partial r} \\ \frac{\partial q_2}{\partial r} \end{pmatrix} \tag{S-49}$$

Equation (S-49) is essentially equivalent to the flux relation used by Habgood[25] to model transient overshoots in the loading of N_2 during transient uptake of N_2/CH_4 in LTA-4A zeolite. These flux relations (S-49) are also incorporated into the models for describing the transient breakthroughs in fixed bed adsorbers by Ruthven, Farooq, Knaebel, and co-workers.[26-29]

3.6 Ignoring thermodynamic coupling effects

In the Henry regime of adsorption, i.e. at low component loading, thermodynamic correction factors may be adequately described by $\Gamma_{ij} = \delta_{ij}$, the Kronecker delta.

$$\begin{bmatrix} \Gamma_{11} & \Gamma_{12} \\ \Gamma_{21} & \Gamma_{22} \end{bmatrix} = \begin{bmatrix} 1 & 0 \\ 0 & 1 \end{bmatrix}; \quad \begin{pmatrix} N_1 \\ N_2 \end{pmatrix} = -\rho \begin{bmatrix} Đ_1 & 0 \\ 0 & Đ_2 \end{bmatrix} \begin{pmatrix} \frac{\partial q_1}{\partial r} \\ \frac{\partial q_2}{\partial r} \end{pmatrix} \tag{S-50}$$

Indeed, the major objective of this article is to demonstrate the inadequacy of Equation (S-50) to model transient mixture uptake in microporous crystals, and transient breakthroughs in fixed bed adsorbers.

3.7 List of Figures for Diffusion in Microporous Crystalline Materials

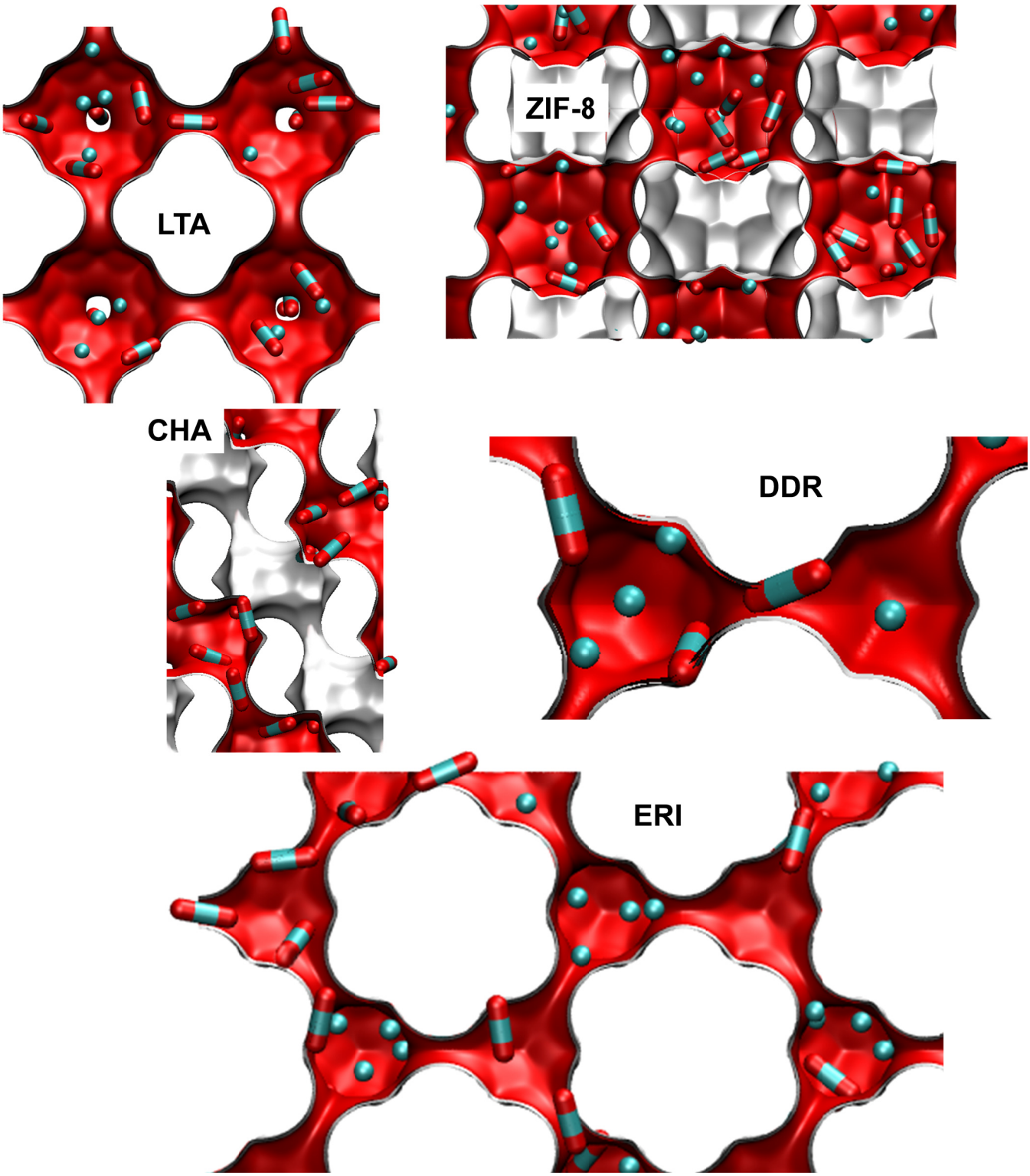

Figure S-1. Structures consisting of cages separated by narrow windows: LTA, CHA, DDR, ERI and ZIF-8.

4 Transient breakthroughs in fixed bed adsorbers

We first analyze the transient uptake of mixtures within a spherical micro-porous crystalline particle.

4.1 Transient uptake inside microporous crystals

The radial distribution of molar loadings, q_i, within a spherical crystallite, of radius r_c, is obtained from a solution of a set of differential equations describing the uptake

$$\rho \frac{\partial q_i(r,t)}{\partial t} = -\frac{1}{r^2}\frac{\partial}{\partial r}\left(r^2 N_i\right) \tag{S-51}$$

The intra-crystalline fluxes N_i, in turn, are related to the radial gradients in the molar loadings by Equation (S-45), or the simplified Equation (S-48) for the negligible correlations scenario. At time $t = 0$, i.e. the initial conditions, the molar loadings $q_i(r,0)$ at all locations r within the crystal are uniform (zero loadings). For all times $t \geq 0$, the exterior of the crystal is brought into contact with a bulk gas mixture at partial pressures p_{i0} that is maintained constant till the crystal reaches thermodynamic equilibrium with the surrounding gas mixture. At any time t, the component loadings at the surface of the particle $q_i(r_c,t) = q_i^*$ is in equilibrium with the bulk phase gas mixture with partial pressures p_{i0}. In the general case, the component loadings are calculated using the Ideal Adsorbed Solution Theory (IAST) of Myers and Prausnitz.[2] Alternatively, in some cases, the mixed-gas Langmuir equation (S-30) may be of sufficient accuracy. An important advantage of the use of the mixed-gas Langmuir model is that the matrix of the thermodynamic correction factors can be determined explicitly using Equation (S-42).

At any time t, during the transient approach to thermodynamic equilibrium, the spatial-averaged component loading within the crystallites of radius r_c is calculated using

$$\bar{q}_i(t) = \frac{3}{r_c^3}\int_0^{r_c} q_i(r,t) r^2 dr \tag{S-52}$$

Summing equation (S-52) over all *n* species in the mixture allows calculation of the *total average* molar loading of the mixture within the crystallite

$$\bar{q}_t(t,z) = \sum_{i=1}^{n} \bar{q}_i(t,z) \tag{S-53}$$

The spatial-averaged $\bar{q}_i(t)$ and $\bar{q}_t(t,z)$ can be compared directly with experimental transient uptake data.

There is no generally applicable analytical solution to describe transient diffusion of binary mixtures and the set of equations (S-45), (S-51), and (S-52), and (S-53) need to be solved numerically using robust computational techniques. However, see Krishna[30] for simplified approaches to describe transient mixture uptake using the matrix generalization of the Geddes[31] and Glueckauf[32] models.

Equations (S-51) are first subjected to finite volume discretization. One of two strategies can be adopted: (a) equi-volume discretization, or (b) equi-distant discretization; see Figure S-2. The choice of the discretization scheme used is crucially important in obtaining accurate, converged results. The choice of equi-volume slices is needed when the gradients of the loadings are particularly steep nearer to $r = r_c$. For either strategy, about 20 – 150 slices were employed in the simulations presented in this work, depending on the guest/host combination. Combination of the discretized partial differential equations (S-51) along with algebraic equations describing mixture adsorption equilibrium (IAST or mixed-gas Langmuir model), results in a set of differential-algebraic equations (DAEs), which are solved using BESIRK.[33] BESIRK is a sparse matrix solver, based on the semi-implicit Runge-Kutta method originally developed by Michelsen,[34] and extended with the Bulirsch-Stoer extrapolation method.[35] Use of BESIRK improves the numerical solution efficiency in solving the set of DAEs. The evaluation of the sparse Jacobian required in the numerical algorithm is largely based on analytic expressions.[18] Further details of the numerical procedures used in this work, are provided by Krishna and co-workers;[18, 36-38] interested readers are referred to our website that contains the numerical details.[36]

4.2 Modelling transient breakthroughs in fixed bed

We describe below the simulation methodology used to perform transient breakthrough calculations for fixed bed adsorbers (see schematics in Figure S-2, and Figure S-3). The simulation methodology is the same as used in our earlier publications.[15, 16, 39, 40] For an *n*-component gas mixture flowing through a fixed bed maintained under isothermal, isobaric, conditions, the molar concentrations in the gas phase at any position and instant of time are obtained by solving the following set of partial differential equations for each of the species *i* in the gas mixture[15, 18, 26, 36]

$$-D_{ax}\frac{\partial^2 c_i(t,z)}{\partial z^2}+\frac{\partial c_i(t,z)}{\partial t}+\frac{\partial\left(v(t,z)c_i(t,z)\right)}{\partial z}+\frac{\left(1-\varepsilon\right)}{\varepsilon}\rho\frac{\partial \bar{q}_i(t,z)}{\partial t}=0;\quad i=1,2,...n \tag{S-54}$$

In equation (S-54), t is the time, z is the distance along the adsorber, ρ is the framework density, ε is the bed voidage, D_{ax} is the axial dispersion coefficient, v is the interstitial gas velocity, and $\bar{q}_i(t,z)$ is the *spatially averaged* molar loading within the crystallites of radius r_c, monitored at position z, and at time t. The time $t = 0$, corresponds to the time at which the feed mixture is injected at the inlet to the fixed bed. Prior to injection of the feed, it is assumed that an inert, non-adsorbing, gas flows through the fixed bed. In this model described by equation (S-54), the effects of all mechanisms that contribute to axial mixing are lumped into a single effect axial dispersion coefficient D_{ax}. Ruthven et al.[26] state that more detailed models that include radial dispersion are generally not necessary. They also make the following remark "when mass transfer resistance is significantly greater than axial dispersion, one may neglect the axial dispersion term and assume plug flow". This is the situation that manifests for kinetically controlled separations, the focus of the present article.Consequently, all of the analysis and breakthrough simulations were carried out using the plug flow assumption.

The term $\frac{\partial \bar{q}_i(t,z)}{\partial t}$ in equation (S-54) is determined by solving the set of equations (S-51), and (S-52), and (S-53). At any time t, and position z, the component loadings at the outer surface of the particle $q_i(r_c,t,z)$ is in equilibrium with the bulk phase gas mixture with partial pressures $p_i(t,z)$ in the

bulk gas mixture. In the general case, the component loadings $q_i(r_c,t,z)$ are calculated using the Ideal Adsorbed Solution Theory (IAST) of Myers and Prausnitz.[2] Alternatively, in some cases, the mixed-gas Langmuir equation (S-30) may be of sufficient accuracy.

The *interstitial* gas velocity is related to the *superficial* gas velocity by

$$v = \frac{u}{\varepsilon} \tag{S-55}$$

For the adsorption phase of fixed-bed separations, the entire bed of crystalline particles is considered to be devoid of adsorbates at time $t = 0$, i.e. we have the initial condition

$$t = 0; \quad q_i(0,z) = 0 \tag{S-56}$$

At time, $t = 0$, the inlet to the adsorber, $z = 0$, is subjected to a step input of the n-component gas mixture and this step input is maintained till the end of the adsorption cycle when steady-state conditions are reached.

$$t \geq 0; \quad p_i(0,t) = p_{i0}; \quad u(0,t) = u_0 \tag{S-57}$$

where $u_0 = v_0\varepsilon$ is the superficial gas velocity at the inlet to the adsorber.

For the simulations of the blowdown phase of fixed-bed operations, the fixed-bed is initially equilibrated with co-current flow of the feed gas mixture at the specified temperature and total pressure conditions. At time $t = 0$ the vacuum blowdown operation commences.

Typically, the adsorber length is divided into 100 slices, and each spherical crystallite was discretized into 20 - 150 equi-volume slices. The results thus obtained were confirmed to be of adequate accuracy. Combination of the discretized partial differential equations (PDEs) along with the algebraic equations describing mixture adsorption equilibrium (IAST, or mixed-gas Langmuir model, as appropriate), results in a set of differential-algebraic equations (DAEs), which are solved using BESIRK.[33] BESIRK is a sparse matrix solver, based on the semi-implicit Runge-Kutta method originally developed by Michelsen,[34] and extended with the Bulirsch-Stoer extrapolation method.[35] Use of BESIRK improves the numerical solution efficiency in solving the set of DAEs. The evaluation of the sparse Jacobian

required in the numerical algorithm is largely based on analytic expressions.[18] Further details of the numerical procedures used in this work, are provided by Krishna and co-workers;[18, 36-38] interested readers are referred to our website that contains the numerical details.[36]

For presenting the breakthrough simulation results, we use the dimensionless time, $\tau = \frac{tv}{L}$, obtained by dividing the actual time, t, by the characteristic time, $\frac{L}{v}$, where L is the length of adsorber, v is the interstitial gas velocity.[41]

For all the simulations reported in this article we choose the following: adsorber length, L = 0.3 m; cross-sectional area, A = 1 m^2; superficial gas velocity in the bed, u_0 = 0.04 m s^{-1}; voidage of the packed bed, ε = 0.4. Also, the total pressures is assumed to be constant along the length of the fixed bed. Please note that since the superficial gas velocity is specified, the specification of the cross-sectional area of the tube, A, is not relevant in the simulation results presented. The total volume of the bed is $V_{bed} = LA$. The volume of zeolite or MOF used in the simulations is $V_{ads} = LA(1-\varepsilon)$ = 0.18 m^3. If ρ is the framework density, the mass of the adsorbent in the bed is $m_{ads} = \rho LA(1-\varepsilon)$ kg. It is important to note that the volume of adsorbent, V_{ads}, includes the pore volume of the adsorbent material. In these breakthrough simulations we use the same volume of adsorbent in the breakthrough apparatus, i.e. (1 - ε) A L = 0.18 m^3 = 180 L.

4.3 List of Figures for Transient breakthroughs in fixed bed adsorbers

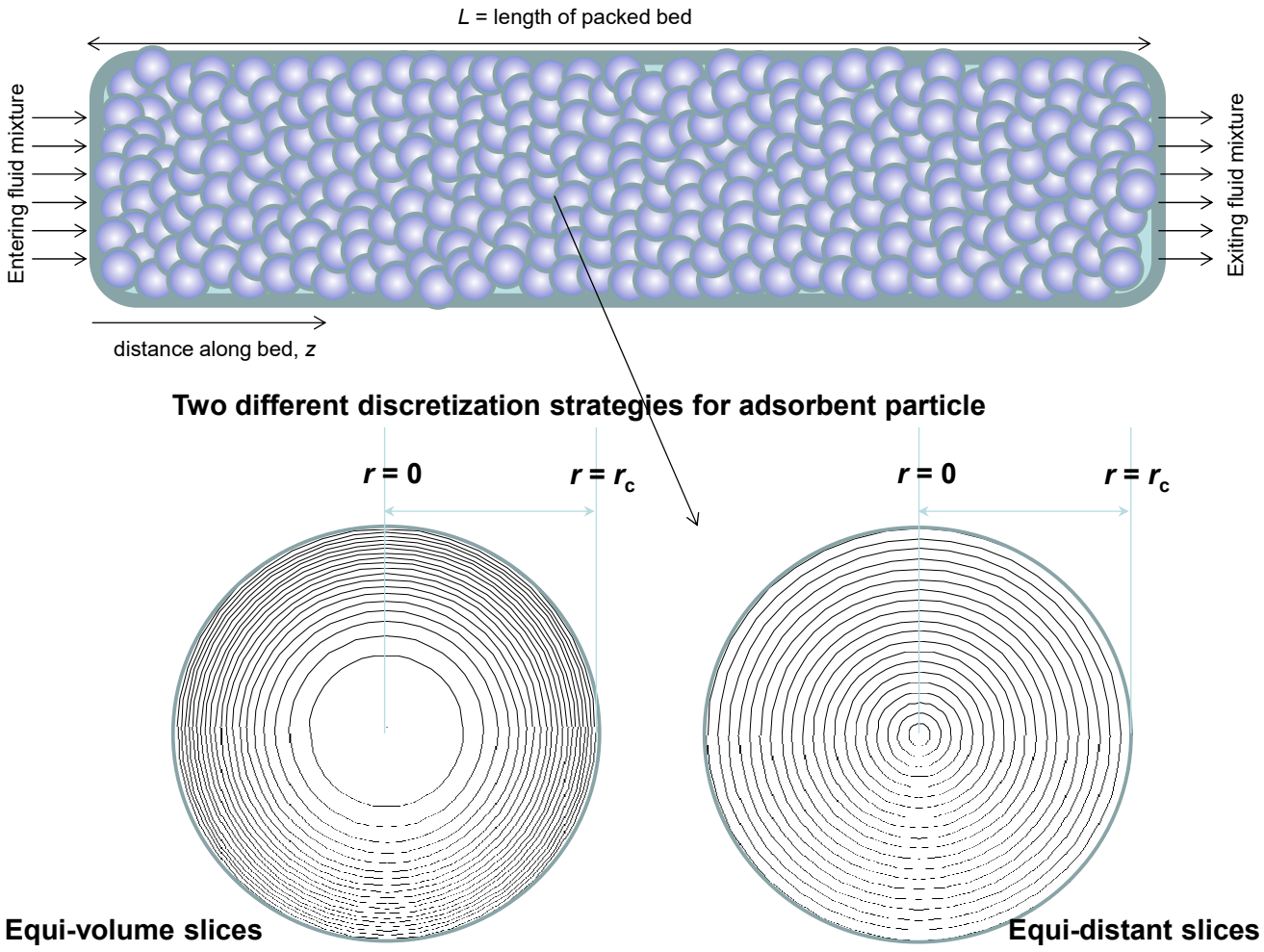

Figure S-2. Two different discretization schemes for a single spherical crystallite.

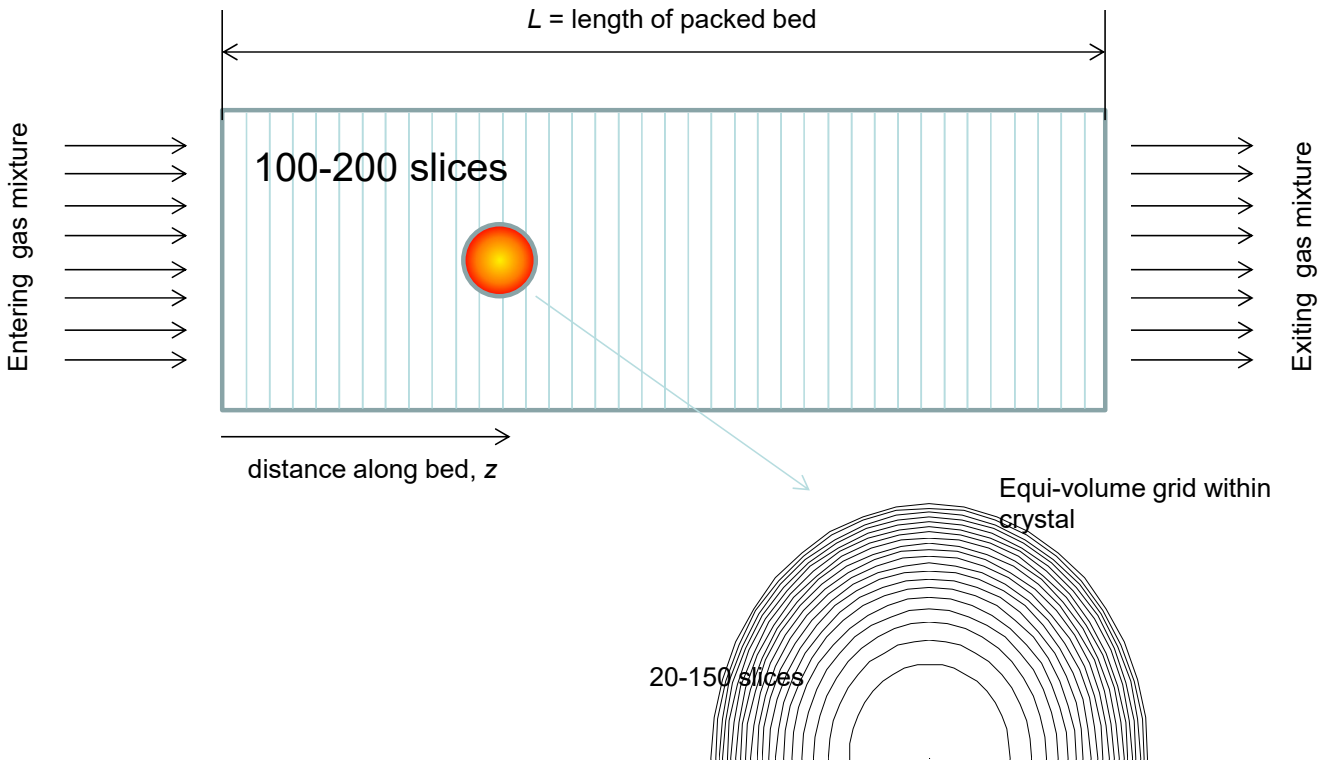

Figure S-3. Discretization scheme for fixed bed adsorber.

5 Separation of N_2/CH_4 mixtures using LTA-4A zeolite

Many natural gas reserves contain nitrogen in concentrations ranging to about 20%.[42] To meet pipeline specifications, the nitrogen level must be reduced to below 4%.[43] A large majority of nitrogen removal facilities use cryogenic distillation, but such units are economical only for large capacity wells. For smaller reserves pressure swing adsorption technology has economic benefits, especially because the feed mixtures are available at high pressures.[42, 43] It is desirable to use adsorbents in pressure swing adsorption (PSA) units that are selective to N_2. For most known adsorbents, the adsorption selectivity for separation of N_2/CH_4 mixtures is in favor of CH_4 due to its higher polarizability.

One practical solution is to rely on diffusion selectivities by using microporous materials, such as LTA-4A zeolite, ETS-4 (ETS = Engelhard Titano Silicate; ETS-4 is also named as CTS-1 = Contracted Titano Silicate -1), and clinoptilolites, that have significantly higher diffusivities of N_2, compared to that of CH_4.[25, 43-46]

5.1 Transient uptake of N_2/CH_4 mixtures in LTA-4A zeolite

The earliest study demonstrating the possibility of using LTA-4A zeolite, utilizing diffusion selectivities for separating $N_2(1)/CH_4(2)$ mixtures is contained in the classic paper of Habgood.[25] LTA-4A zeolite (also called 4A or NaA zeolite) contains extra-framework cations (containing 96Si, 96 Al, 96 Na^+ per unit cell; Si/Al=1). LTA-4A zeolite consists of cages of 743 $Å^3$ volume, separated by 4.11 Å × 4.47 Å 8-ring windows. The pore landscape and structural details of LTA-4A zeolite are provided in Figure S-4. The Na^+ cations partially block the window sites, leading to low magnitudes of guest diffusivities. The partial blocking of the windows enhances efficacy of kinetic separations, because it significantly enhances the ratio of the diffusivities of mobile and tardier species. Molecules jump one-at-a-time across the windows of LTA-4A. Extensive Molecular Dynamics (MD) simulations have confirmed that correlation effects are of negligible importance for mixture diffusion across cage-type zeolites such as CHA, LTA, DDR, ERI that consist of cages separated by windows in the 3.4 Å – 4.2 Å size range.[7, 8, 17, 24] Consequently, the appropriate flux description is provided by Equation (S-48).

Figure S-5(a) presents simulations of transient uptake of 20/80 $N_2(1)/CH_4(2)$ mixtures in crystallites of LTA-4A at 194 K with the bulk gas phase maintained at partial pressures p_1 =20 kPa; p_2 = 80 kPa. Nitrogen is a "pencil-like" molecule (4.4 Å × 3.3 Å) that can hop length-wise across the narrow windows; the "spherical" CH_4 (3.7 Å) is much more severely constrained and has a diffusivity that is 21.7 times lower than that of N_2. The adsorption strength of CH_4, as reflected in the Langmuir "*b*" parameter, is higher than that of N_2 by a factor 2.2; see unary isotherm data fits in Table S-1. The $N_2(1)/CH_4(2)$ mixture constitutes a combination of more-mobile-less-strongly-adsorbed-N_2 and tardier-more-strongly-adsorbed-CH_4. The continuous solid lines in Figure S-5(a) are Maxwell-Stefan model simulations based on Equation (S-48); these simulations display an overshoot in the uptake of the more mobile N_2. The Maxwell-Stefan diffusivities used in the simulations are: $Đ_1/r_c^2$ = 1.56×10^{-5} s^{-1}; $Đ_2/r_c^2$ = 7.2×10^{-9} s^{-1}; these values based on the diffusivity data provided by Habgood.[25] During the initial stages of the transient uptake, the pores of LTA-4A are predominantly richer in the more mobile N_2, but this is displaced by the more strongly adsorbed, tardier CH_4 molecules at longer times. This results in an overshoot in the N_2 uptake during the early stages of the transience. The dashed lines in Figure S-5(a) are the simulations based on Equation (S-50), in which the thermodynamic correction factors are assumed to be described by $\Gamma_{ij} = \delta_{ij}$, i.e. $\begin{bmatrix} \Gamma_{11} & \Gamma_{12} \\ \Gamma_{21} & \Gamma_{21} \end{bmatrix} = \begin{bmatrix} 1 & 0 \\ 0 & 1 \end{bmatrix}$; in this scenario, no N_2 overshoot is experienced. We conclude that the overshoots in the N_2 uptake, that signal the phenomenon of uphill diffusion,[12, 41] is engendered by thermodynamic coupling effects.

Figure S-5(b) presents simulations of transient desorption process in which the initial loadings in the zeolite correspond to the final equilibrated loadings in Figure S-5(a), i.e. corresponding to the bulk gas phase maintained at partial pressures p_1 =20 kPa; p_2 = 80 kPa. At time t = 0, the bulk gas phase partial pressures are reduced to the values p_1 =2 kPa; p_2 = 8 kPa. The continuous solid lines in Figure S-5(b) are Maxwell-Stefan model simulations based on Equation (S-48); these simulations show undershoot in the desorption of the mobile N_2. The dashed lines in Figure S-5(b) are the simulations based on

Equation (S-50), in which the thermodynamic correction factors are assumed to be described by $\Gamma_{ij} = \delta_{ij}$, i.e. $\begin{bmatrix} \Gamma_{11} & \Gamma_{12} \\ \Gamma_{21} & \Gamma_{21} \end{bmatrix} = \begin{bmatrix} 1 & 0 \\ 0 & 1 \end{bmatrix}$; in this scenario, no N_2 undershoot is experienced. We conclude that the undershoot in the N_2 uptake, that signal the phenomenon of uphill diffusion,[12, 41] is engendered by thermodynamic coupling effects.

Overshoots/undershoots during the adsorption/desorption phase of PSA operations have consequences for $N_2(1)/CH_4(2)$ mixture separations in a fixed bed adsorber packed with LTA-4A adsorbent.

5.2 Separating N_2/CH_4 mixtures in fixed bed adsorbers packed with LTA-4A

We consider the separations of 20/80 $N_2(1)/CH_4(2)$ mixtures in a fixed bed adsorber using LTA-4A zeolite operating at a total pressure of 100 kPa, and T = 194 K. Figure S-6(a) show the transient breakthrough simulations for 20/80 $N_2(1)/CH_4(2)$ mixtures through fixed bed adsorber packed with LTA-4A crystals operating at 194 K, and total pressure p_t = 100 kPa. The y-axis is the % CH_4 at the adsorber outlet. The x-axis is the dimensionless time, $\tau = tv/L$, obtained by dividing the actual time, t, by the characteristic time, L/v. The continuous solid lines are simulations taking due account of intra-crystalline diffusion using Equation (S-48) with parameters: $Đ_1/r_c^2 = 1.56\times10^{-5}$ s^{-1}; $Đ_2/r_c^2 = 7.2\times10^{-9}$ s^{-1}. The dashed lines are the corresponding simulations based on Equation (S-50), in which the thermodynamic correction factors are assumed to be described by $\Gamma_{ij} = \delta_{ij}$, the Kronecker delta.

For the target purity of CH_4 is 96%, corresponding to prescribed pipeline specification, we can determine the moles of 96%+ pure CH_4 produced from a material balance on the adsorber. Expressed per kg of LTA-4A zeolite in the packed bed, the respective productivities are 0.09 and 0.002 mol kg^{-1}. Ignoring thermodynamic coupling effects severely underestimates the separation performance by a factor of about 50.

Figure S-6(b) present simulations of the co-current blowdown process operating at deep vacuum corresponding to p_1 =0.2 Pa; p_2 = 0.8 Pa; the initial loadings in the adsorber correspond to the final

equilibrated loadings determined in Figure S-6(a). During the co-current blowdown phase, the more mobile component, N_2, exits the adsorber in higher proportions. The continuous solid lines are Maxwell-Stefan model simulations based on Equation (S-48). The dashed lines are the simulations based on Equation (S-50), in which the thermodynamic correction factors are assumed to be described by $\Gamma_{ij} = \delta_{ij}$, the Kronecker delta. Properly accounting for thermodynamic coupling effects results in a gas mixture composition that is richer in the more mobile component, N_2. In other words, the purged gas mixture is richer in N_2 due to the phenomena of uphill diffusion and transient undershoots experienced in Figure S-5(b).

5.3 List of Tables for Separation of N2/CH4 mixtures using LTA-4A zeolite

Table S-1. 1-site Langmuir parameters for N_2 and CH_4 in LTA-4A zeolite at 194 K. These parameters have been fitted from the isotherm data scanned from the paper by Habgood[25]

	q_{sat} mol kg^{-1}	b Pa^{-1}
N_2	3.6	9.4×10^{-5}
CH_4	3.6	2.08×10^{-4}

5.4 List of Figures for Separation of N2/CH4 mixtures using LTA-4A zeolite

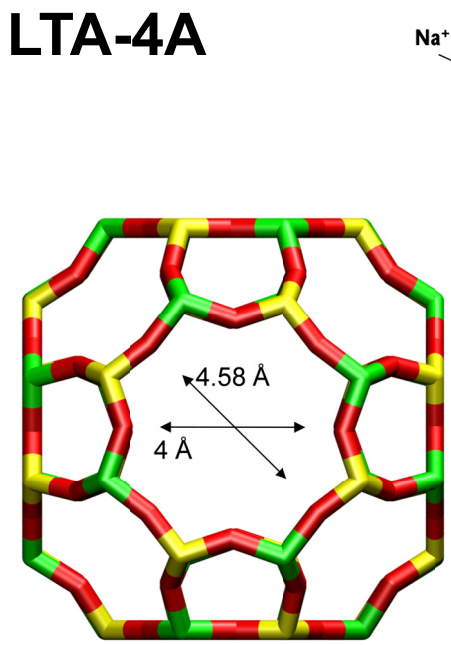

LTA-4A

The window dimension calculated using the van der Waals diameter of framework atoms = 2.7 Å is indicated above by the arrow.

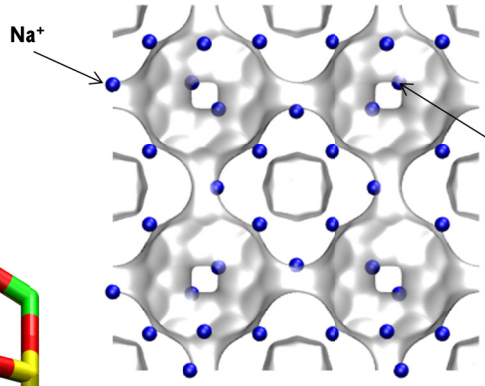

LTA-4A (96 Na+)

	LTA-4A
a /Å	24.555
b /Å	24.555
c /Å	24.555
Cell volume / Å^3	14805.39
conversion factor for [molec/uc] to [mol per kg Framework]	0.0733
conversion factor for [molec/uc] to [kmol/m^3]	0.2991
ρ [kg/m3] (with cations)	1529.55
MW unit cell [g/mol(framework+cations)]	13637.27
ϕ, fractional pore volume	0.375
open space / Å^3/uc	5552.0
Pore volume / cm^3/g	0.245
Surface area /m^2/g	
DeLaunay diameter /Å	4.00

Figure S-4. Structural details of LTA-4A zeolite.

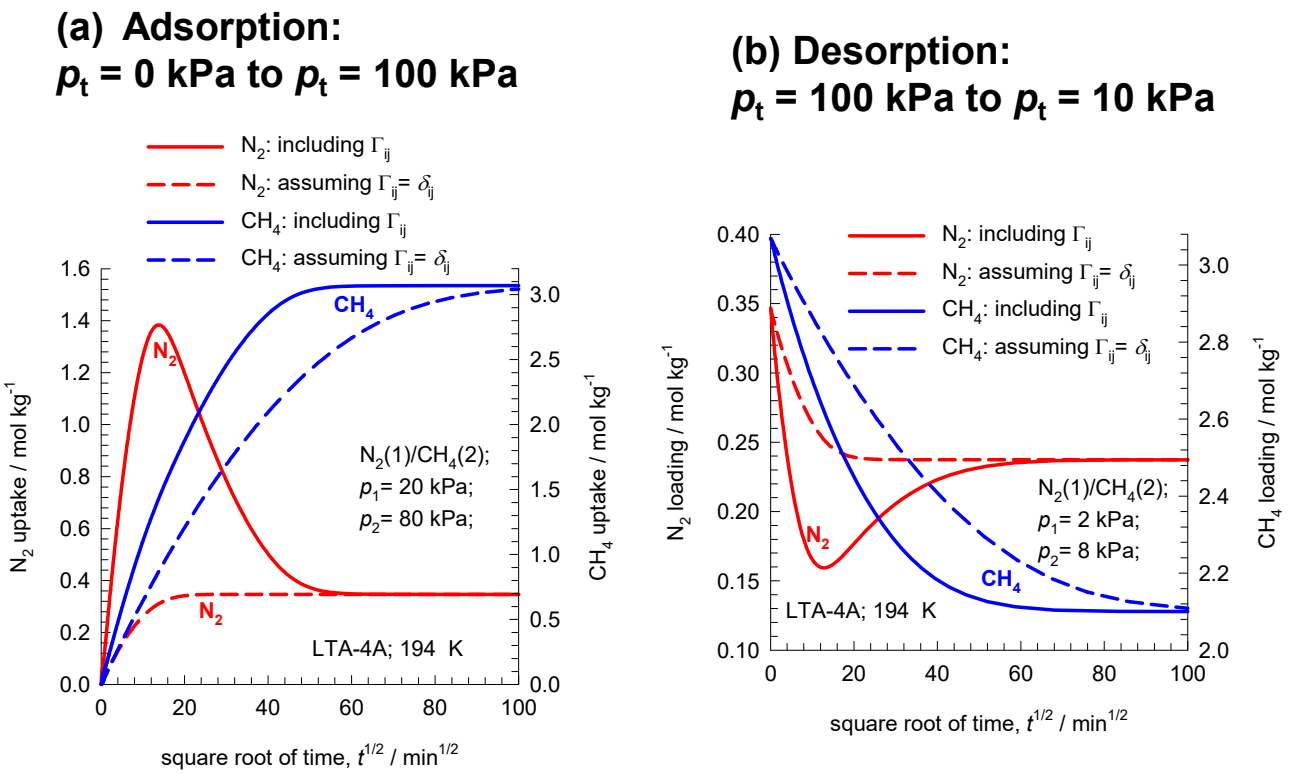

Figure S-5. (a) Transient uptake of 20/80 $N_2(1)/CH_4(2)$ mixture within LTA-4A crystals, exposed to binary gas mixtures at 194 K and total pressure in the bulk gas phase p_t = 100 kPa. (b) Transient desorption of $N_2(1)/CH_4(2)$ mixtures in LTA-4A crystals. The initial loadings are those corresponding to the equilibrated loadings in (a). At time t = 0, the bulk gas phase mixture is maintained at p_1 = 2 kPa, and p_2 = 8 kPa. The unary isotherms are provided in Table S-1. The continuous solid lines are Maxwell-Stefan model simulations based on Equation (S-48). The dashed lines are the simulations based on Equation (S-50), in which the thermodynamic correction factors are assumed to be described by $\Gamma_{ij} = \delta_{ij}$, the Kronecker delta. The Maxwell-Stefan diffusivities used in the simulations are: $Đ_1/r_c^2 = 1.56\times10^{-5}$ s^{-1}; $Đ_2/r_c^2 = 7.2\times10^{-9}$ s^{-1}.

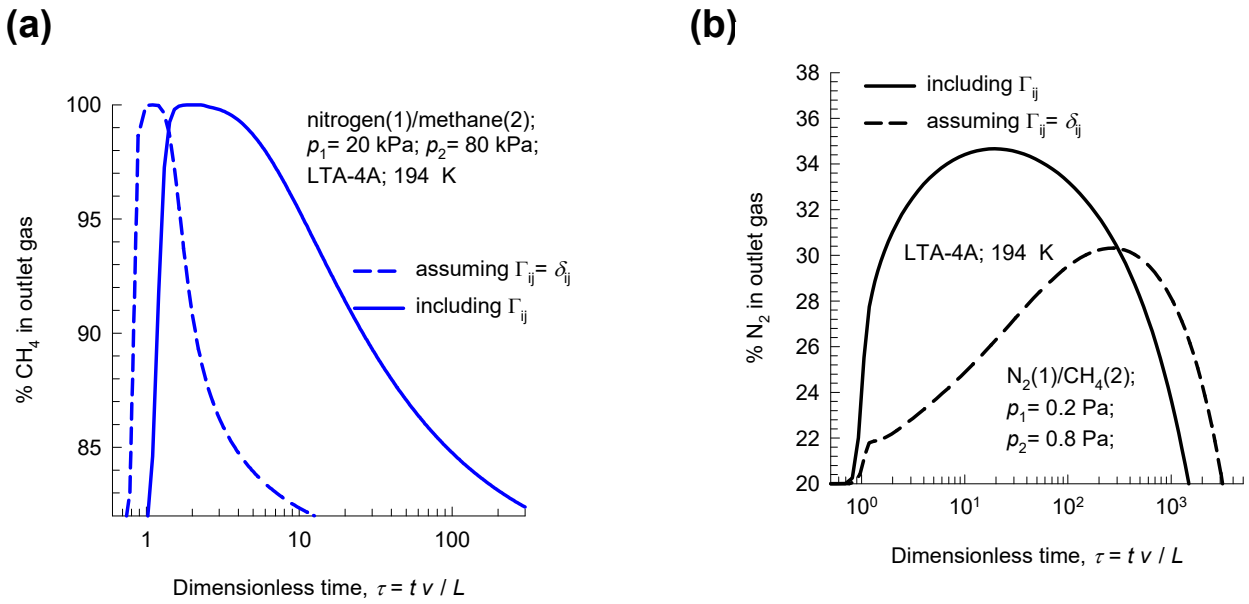

Figure S-6. (a) Transient breakthrough of 20/80 $N_2(1)/CH_4(2)$ mixture in fixed bed adsorber packed with LTA-4A crystals operating at 194 K, and total pressure p_t = 100 kPa. (b) Co-current blowdown of $N_2(1)/CH_4(2)$ mixture in fixed bed adsorber packed with LTA-4A crystals operating at 194 K. The initial loadings correspond to the equilibrated loadings in (a). At time t = 0, the pressure is reduced to deep vacuum, p_t = 1 Pa. The continuous solid lines are Maxwell-Stefan model simulations based on Equation (S-48). The dashed lines are the simulations based on Equation (S-50), in which the thermodynamic correction factors are assumed to be described by $\Gamma_{ij} = \delta_{ij}$, the Kronecker delta. The Maxwell-Stefan diffusivities used in the simulations are: $Đ_1/r_c^2 = 1.56\times10^{-5}$ s^{-1}; $Đ_2/r_c^2 = 7.2\times10^{-9}$ s^{-1}.

6 Separation of CO_2/C_2H_6 mixtures with DDR zeolite

DDR consists of cages of 277.8 $Å^3$ volume, separated by 3.65 Å × 4.37 Å 8-ring windows; the pore landscapes and structural details are provided in Figure S-7, and Figure S-8. The guest molecules jump one-at-a-time across the narrow 8-ring windows. Consequently, correlation effects are of negligible importance; the intra-crystalline fluxes N_i, in turn, are related to the radial gradients in the molar loadings by Equation (S-48).

Figure S-9(a) presents simulations of the transient uptake of $CO_2(1)/C_2H_6(2)$ gas mixtures within crystals of DDR zeolite at 298 K. The partial pressures in the bulk gas phase are $p_1 = p_2 = 20$ kPa. The continuous solid lines are simulations of the transient uptake using the flux relations (S-48). The Maxwell-Stefan model displays overshoots in CO_2 loadings during the early stages of transient uptake. The overshoots in the CO_2 uptake signal the phenomenon of uphill diffusion, engendered by thermodynamic coupling.[16, 47] In order to confirm that thermodynamic coupling effects are responsible for the overshoots, we also performed transient uptake in which the thermodynamic correction factors are assumed to be described by $\Gamma_{ij} = \delta_{ij}$, the Kronecker delta. The dashed lines in Figure S-9(a) represent the simulation results based on Equation (S-50); with this simplified model, no overshoots in the CO_2 uptake are experienced. An important consequence of thermodynamic coupling effects is that supra-equilibrium loadings of CO_2 are realized during the early transience.

Figure S-9(b) presents simulations of transient desorption process in which the initial loadings in the zeolite correspond to the final equilibrated loadings in Figure S-9(a), i.e. corresponding to the bulk gas phase maintained at partial pressures $p_1 = p_2 = 20$ kPa. At time $t = 0$, the bulk gas phase partial pressures are reduced to the values $p_1 = p_2 = 2$ kPa. The continuous solid lines in Figure S-9(b) are Maxwell-Stefan model simulations based on Equation (S-48); these simulations show undershoot in the desorption of the mobile CO_2. The dashed lines in Figure S-9(b) are the simulations based on Equation

(S-50), in which the thermodynamic correction factors are assumed to be described by $\Gamma_{ij} = \delta_{ij}$, i.e. $\begin{bmatrix} \Gamma_{11} & \Gamma_{12} \\ \Gamma_{21} & \Gamma_{21} \end{bmatrix} = \begin{bmatrix} 1 & 0 \\ 0 & 1 \end{bmatrix}$; in this scenario, no CO_2 undershoot is experienced. We conclude that the undershoot in the CO_2 uptake, that signals the phenomenon of uphill diffusion,[12, 41] is engendered by thermodynamic coupling effects.

6.1 Separating CO_2/C_2H_6 mixtures in fixed bed adsorber packed with DDR zeolite

The transient uptake simulations in Figure S-9(a,b) suggest the possibility of diffusion-selective purification of ethane by selective removal of CO_2 present as impurities in mixtures with ethane.

Figure S-10(a) show the transient breakthrough simulations for 1:1 CO_2/C_2H_6 mixtures through fixed bed adsorber packed with DDR crystals operating at 298 K, and total pressure p_t = 40 kPa. The *y*-axis is the % component at the adsorber outlet. The *x*-axis is the dimensionless time, $\tau = tv/L$, obtained by dividing the actual time, *t*, by the characteristic time, L/v. The continuous solid lines are simulations taking due account of intra-crystalline diffusion using Equation (S-48) with parameters: $Đ_1/r_c^2$ = 0.00125 s^{-1}; $Đ_1/Đ_2$ = 1333.

We note that C_2H_6 breaks through earlier and can be recovered in purified form during the early stages of the transient operations, prior to the breakthrough of CO_2. The dashed lines in Figure S-10(a) are the simulations in which thermodynamic coupling effects are ignored and Equation (S-50) is used to describe the transfer fluxes. In this scenario, the breakthrough of CO_2 occurs earlier and therefore the productivity of purified C_2H_6 is lower. If we assume that the target purity of C_2H_6 is 90%, we can determine the moles of 90%+ pure C_2H_6 produced from a material balance on the adsorber. Expressed per kg of DDR zeolite in the packed bed, the respective productivities are 0.18 and 0.054 mol kg^{-1}, respectively. Ignoring thermodynamic coupling effects severely underestimates the separation performance.

Figure S-10(b) presents simulations of the co-current blowdown of CO_2(1)/C_2H_6(2) mixtures in fixed bed packed with DDR zeolite crystals. The initial loadings are those corresponding to the equilibrated

loadings in Figure S-10(a). At time $t = 0$, the bulk gas phase mixture is maintained at $p_1 = p_2 = 0.1$ Pa. The continuous solid lines are simulations taking due account of intra-crystalline diffusion using Equation (S-48). The dashed lines in Figure S-10(a) are the simulations in which thermodynamic coupling effects are ignored and Equation (S-50) is used to describe the transfer fluxes. For simulations that include thermodynamic coupling, the composition of the purged gas mixture during co-current blowdown is richer in the more mobile CO_2; this is directly attributable to uphill diffusion and the undershoot phenomena witnessed in Figure S-9(b).

6.2 List of Tables for Separation of CO2/C2H6 mixtures with DDR zeolite

Table S-2. 1-site Langmuir parameters for CO_2 and C_2H_6 in DDR zeolite at 298 K. These parameters have been fitted from the data scanned from Figure 36, Chapter 4 of the PhD dissertation of Binder.[48]

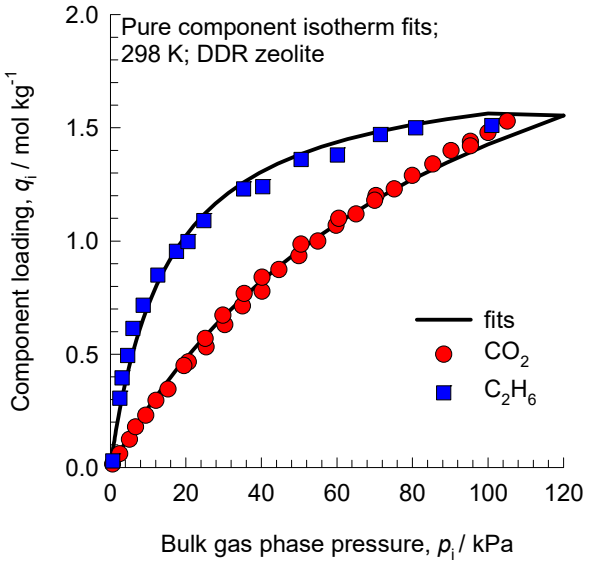

	q_{sat} mol kg^{-1}	b Pa^{-1}
CO_2	2.8	1.04×10^{-5}
C_2H_6	1.8	6.6×10^{-5}

6.3 List of Figures for Separation of CO2/C2H6 mixtures with DDR zeolite

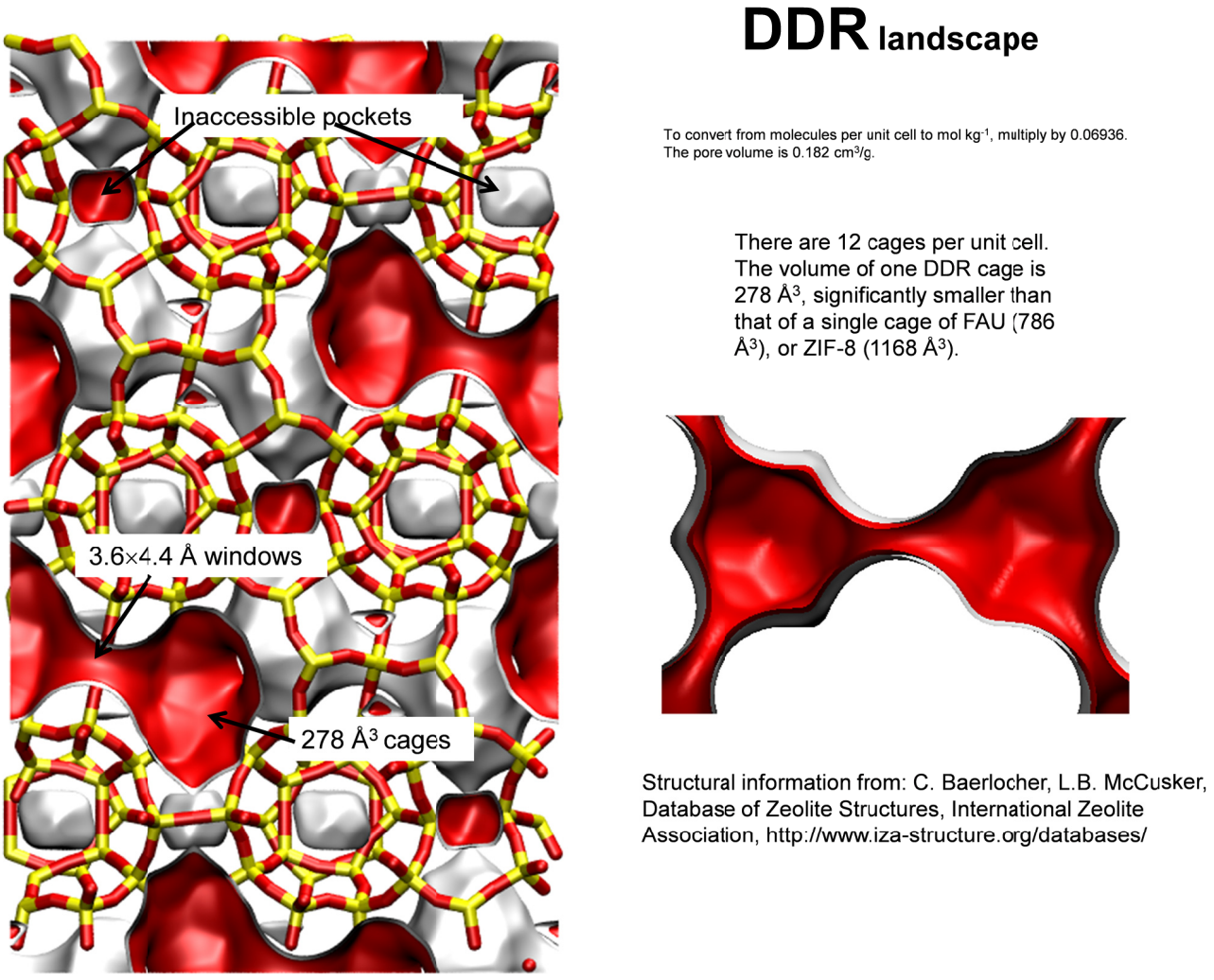

Figure S-7. Pore landscape of all-silica DDR zeolite.

DDR window and pore dimensions

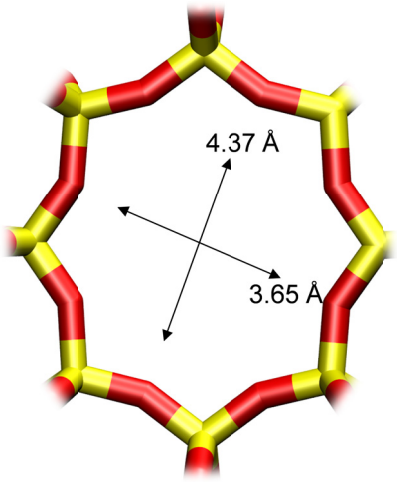

DDR

The window dimensions calculated using the van der Waals diameter of framework atoms = 2.7 Å are indicated above by the arrows.

	DDR
a /Å	24.006
b /Å	13.86
c /Å	40.892
Cell volume / Å^3	13605.72
conversion factor for [molec/uc] to [mol per kg Framework]	0.0693
conversion factor for [molec/uc] to [kmol/m^3]	0.4981
ρ [kg/m3]	1759.991
MW unit cell [g/mol(framework)]	14420.35
ϕ, fractional pore volume	0.245
open space / Å^3/uc	3333.5
Pore volume / cm^3/g	0.139
Surface area /m^2/g	350.0
DeLaunay diameter /Å	3.65

Figure S-8. Structural details of all-silica DDR zeolite.

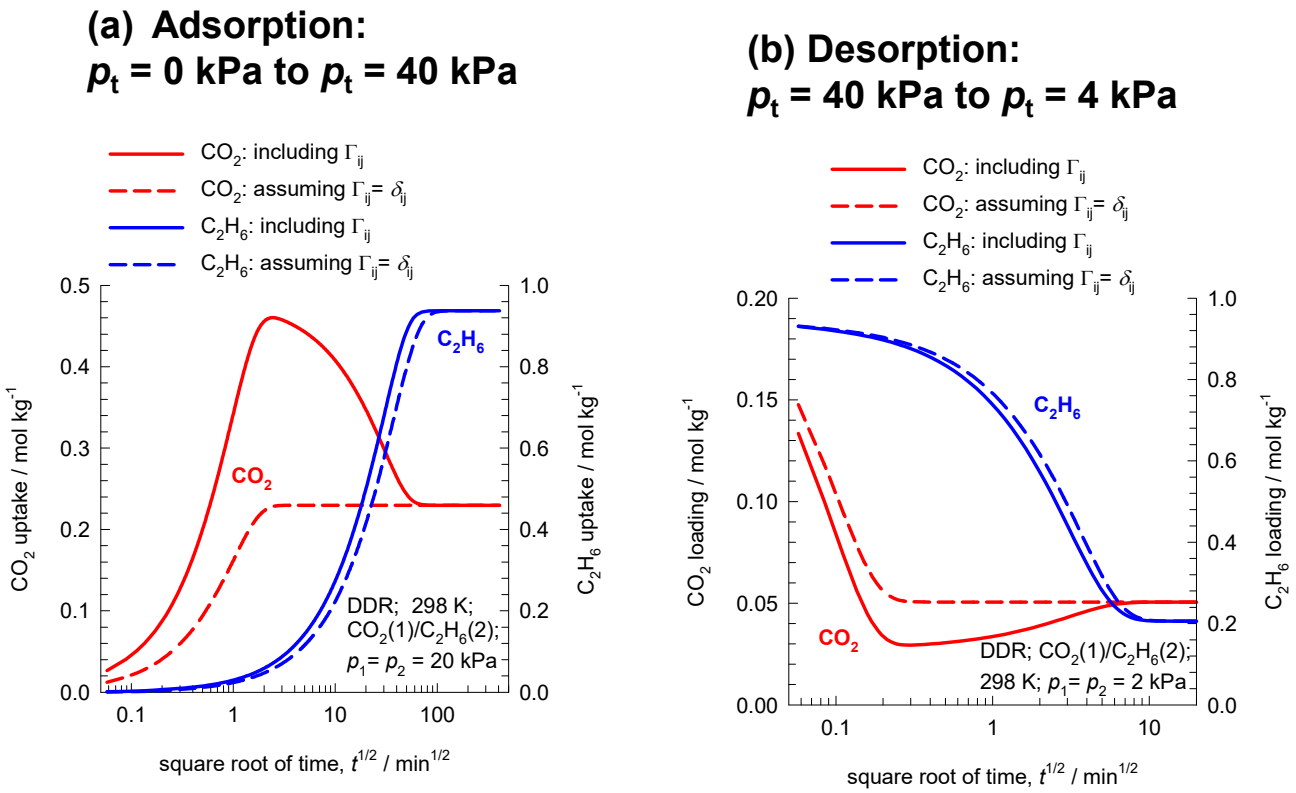

Figure S-9. (a) Transient uptake of $CO_2(1)/C_2H_6(2)$ mixture within DDR zeolite crystals at 298 K; the partial pressures in the bulk gas phase are $p_1 = p_2 = 20$ kPa. (b) Transient desorption of $CO_2(1)/C_2H_6(2)$ mixtures in DDR zeolite crystals. The initial loadings are those corresponding to the equilibrated loadings in (a). At time $t = 0$, the bulk gas phase mixture is maintained at $p_1 = p_2 = 2$ kPa. The continuous solid lines are Maxwell-Stefan model simulations based on Equation (S-48), with parameters: $Đ_1/r_c^2 = 0.00125$ s^{-1}; $Đ_1/Đ_2 = 1333$. The dashed lines are the simulations based on Equation (S-50), in which the thermodynamic correction factors are assumed to be described by $\Gamma_{ij} = \delta_{ij}$, the Kronecker delta. The single-site Langmuir parameters are provided in Table S-2. On the basis of comparisons with IAST calculations, Krishna[16] has established that the mixed-gas Langmuir model predicts the mixture adsorption equilibrium with good accuracy.

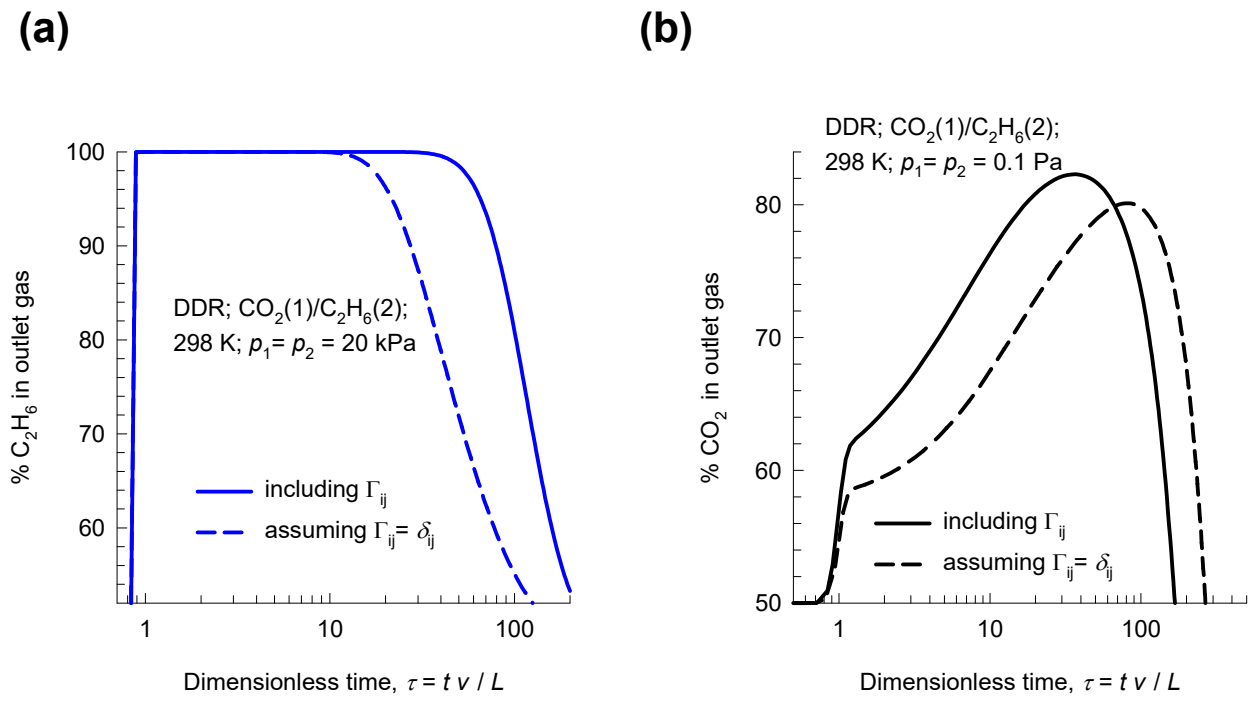

Figure S-10. (a) Transient breakthrough of $CO_2(1)/C_2H_6(2)$ mixture in fixed bed packed with DDR zeolite crystals at 298 K; the partial pressures in the bulk gas phase feed mixture are $p_1 = p_2 = 20$ kPa. (b) Co-current blowdown of $CO_2(1)/C_2H_6(2)$ mixtures in fixed bed packed with DDR zeolite crystals. The initial loadings are those corresponding to the equilibrated loadings in (a). At time $t = 0$, the bulk gas phase mixture is maintained at $p_1 = p_2 = 0.1$ Pa. The continuous solid lines are simulations based on Equation (S-48) for the transfer fluxes, with parameters: $Đ_1/r_c^2 = 0.00125$ s^{-1}; $Đ_1/Đ_2 = 1333$. The dashed lines are the simulations based on Equation (S-50), in which the thermodynamic correction factors are assumed to be described by $\Gamma_{ij} = \delta_{ij}$, the Kronecker delta. The single-site Langmuir parameters are provided in Table S-2. On the basis of comparisons with IAST calculations, Krishna[16] has established that the mixed-gas Langmuir model predicts the mixture adsorption equilibrium with good accuracy.

7 Separation of O_2/N_2 mixtures

The separation of air to produce N_2 and O_2 of high purities is one of the most important industrial processes that uses pressure swing adsorption technology.[26, 49] The process technologies are geared to either production of purified O_2 or purified N_2. Cryogenic distillation has been the common technologies for this separation, but adsorptive separations offer energy efficient alternatives. Purified O_2 is required for a wide variety of applications that include portable adsorption units for medical applications and in space vehicles. Nitrogen is required in applications where it is desired or necessary to exclude oxygen. Typical industrial applications include preservation of fruit and produce during trucking, the blanketing of fuel tanks of fighter aircraft, the inerting of reactors in a number of pharmaceutical processes, laser cutting. N_2 is required for use in laboratory analytical equipment such as GC, LC, LCMS, FTIR, ICP, and in glove boxes.

Diffusion-selective separation of O_2/N_2 mixtures with LTA-4A zeolite are employed for production of purified N_2 from air.[28, 50] Diffusion limitations manifest in LTA-4A because the window regions are partially blocked by the cations; see pore landscape in Figure S-11.

7.1 Transient uptake of O_2/N_2 mixtures in LTA-4A zeolite

Figure S-12(a) presents the simulations of transient uptake of $O_2(1)/N_2(2)$ mixture in LTA-4A zeolite at 298 K and total pressure of 600 kPa. The partial pressures of the components in the bulk gas phase are p_1 = 126 kPa, p_2 = 474 kPa. The continuous solid lines are Maxwell-Stefan model simulations based on Equation (S-48), that accounts for thermodynamic coupling. The O_2 overshoot signals uphill diffusion.[12,41] The dashed lines are the simulations based on Equation (S-50), in which the thermodynamic correction factors are assumed to be described by $\Gamma_{ij} = \delta_{ij}$, the Kronecker delta; in this scenario there is no O_2 overshoot. The conclusion to be drawn is that the O_2 overshoot is engendered by thermodynamic coupling effects.

Figure S-12(b) presents simulations of transient desorption process in which the initial loadings in the zeolite correspond to the final equilibrated loadings in Figure S-12(a), i.e. corresponding to the bulk gas phase maintained at partial pressures p_1 = 126 kPa, p_2 = 474 kPa. At time t = 0, the bulk gas phase partial pressures are reduced to the values p_1 = 21 kPa, p_2 = 79 kPa. The continuous solid lines in Figure S-12(b) are Maxwell-Stefan model simulations based on Equation (S-48); these simulations show undershoot in the desorption of the more mobile O_2. The dashed lines in Figure S-12(b) are the simulations based on Equation (S-50), in which the thermodynamic correction factors are assumed to be described by $\Gamma_{ij} = \delta_{ij}$, i.e. $\begin{bmatrix} \Gamma_{11} & \Gamma_{12} \\ \Gamma_{21} & \Gamma_{21} \end{bmatrix} = \begin{bmatrix} 1 & 0 \\ 0 & 1 \end{bmatrix}$; in this scenario, no O_2 undershoot is experienced. We conclude that the undershoot in the O_2 uptake, that signals the phenomenon of uphill diffusion,[12, 41] is engendered by thermodynamic coupling effects.

7.2 O_2/N_2 mixture separations in fixed bed adsorber packed with LTA-4A

Diffusion-selective separations may be exploited for production of pure N_2 relying on the significantly lower diffusivity of N_2 as compared to O_2, and uphill diffusion. To demonstrate the feasibility of this concept, Figure S-13(a) presents transient breakthrough simulations for a fixed bed operating at 298 K and total pressure of 600 kPa. The continuous solid lines are Maxwell-Stefan model simulations based on Equation (S-48), that accounts for thermodynamic coupling.[28, 50] Neglecting thermodynamic coupling effects leads to lower productivity of purified N_2, during the initial transience.

For an assumed target purity of 95%+ N_2, we can determine the moles of 95%+ pure N_2 produced from a material balance on the adsorber. Expressed per kg of LTA-4A zeolite in the packed bed, the respective productivities are 0.066 and 0.036 mol kg^{-1}. Ignoring thermodynamic coupling effects underestimates the separation performance by about 40%.

Figure S-13(b) presents simulations of co-current blowdown of $O_2(1)/N_2(2)$ mixtures in fixed bed packed with DDR zeolite crystals. The initial loadings are those corresponding to the equilibrated loadings in (a). At time t = 0, the bulk gas phase mixture is maintained at p_1 =2.1 Pa, p_2 = 7.9 Pa.

7.3 List of Tables for Separation of O2/N2 mixtures

Table S-3. 1-site Langmuir parameters for O_2 and N_2 in LTA-4A zeolite at 298 K. These isotherm data are taken from Farooq et al.[28, 50] These data are for RS-10, a modified version of LTA-4A that affords higher diffusion selectivity in favor of O_2.

	q_{sat} mol kg^{-1}	b Pa^{-1}
O_2	1.91	5.65×10^{-7}
N_2	1.91	1.13×10^{-6}

On the basis of the information provided in Table 3 of Farooq et al.[28]

The crystal framework density $\rho = 1100$ kg m^{-3};

The Maxwell-Stefan diffusivities are

$Đ_1/r_c^2 = 2.75\times10^{-2}$ s^{-1}; $Đ_2/r_c^2 = 7.5\times10^{-4}$ s^{-1}; $Đ_1/Đ_2 = 36.7$.

7.4 List of Figures for Separation of O2/N2 mixtures

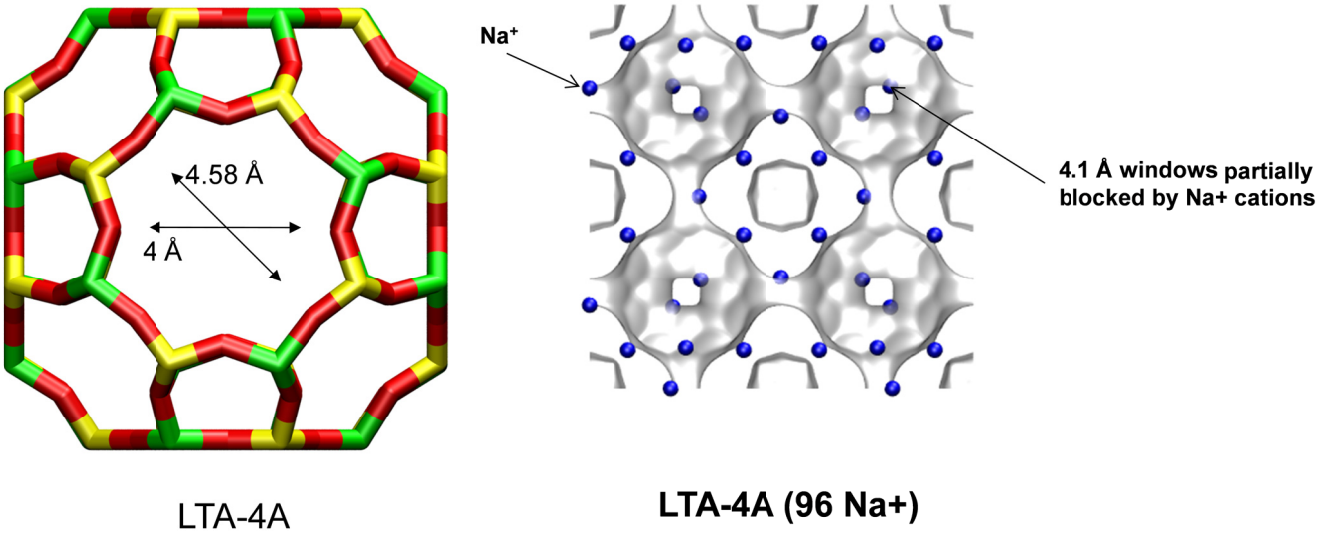

Figure S-11. Partial blocking of the windows of LTA-4A zeolite.

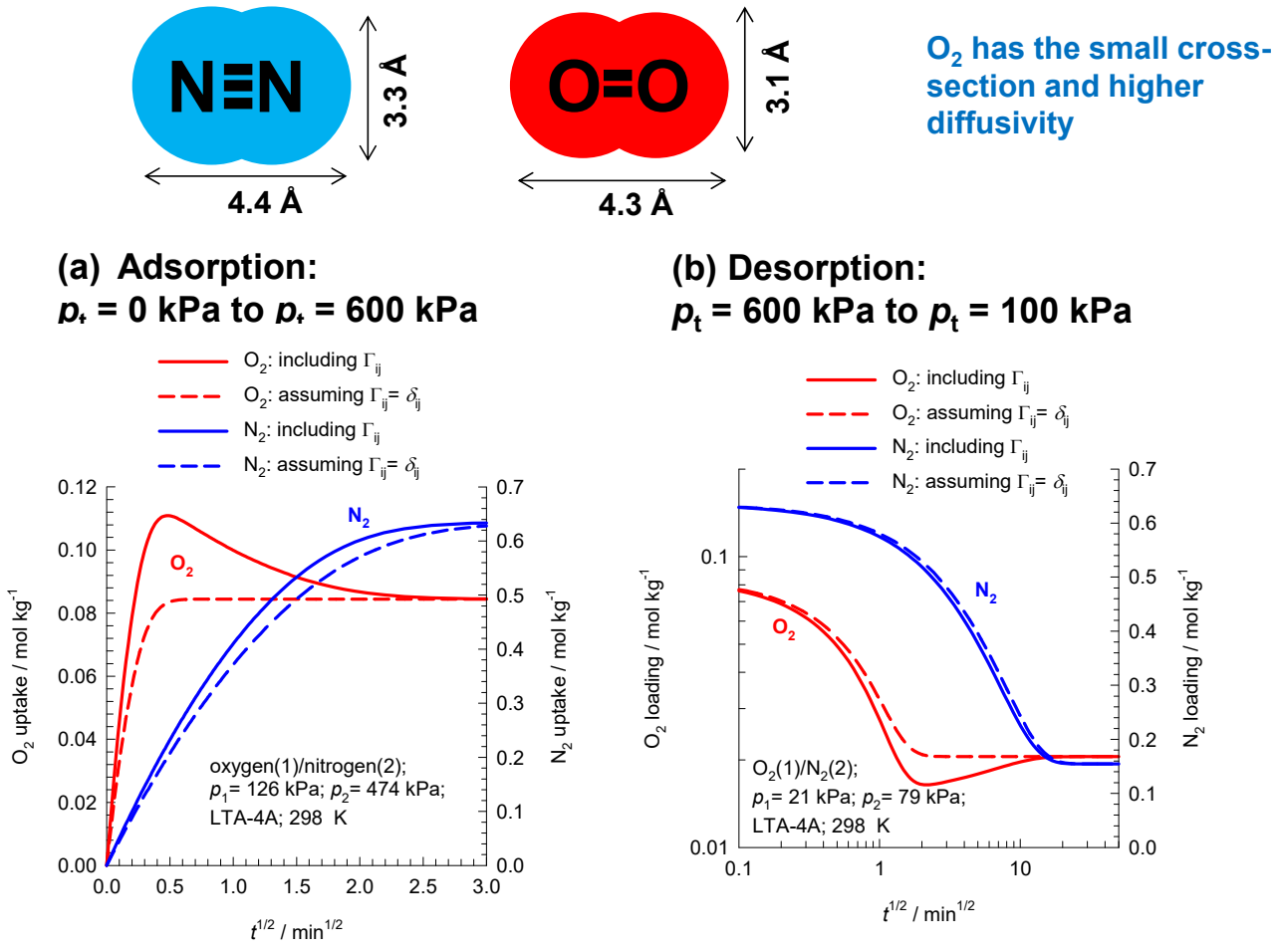

Figure S-12. (a) Transient uptake of 21/79 $O_2(1)/N_2(2)$ mixture in LTA-4A zeolite at 298 K and total pressure of 600 kPa. The partial pressures of the components in the bulk gas phase are p_1 = 126 kPa, p_2 = 474 kPa. (b) Transient desorption of 21/79 $O_2(1)/N_2(2)$ mixture in LTA-4A zeolite at 298 K. The initial loadings are those corresponding to the final equilibrated loadings in (a). At time t = 0, the bulk gas phase mixture is maintained at p_1 = 21 kPa, p_2 = 79 kPa. The unary isotherms are provided in Table S-3. The continuous solid lines are Maxwell-Stefan model simulations based on Equation (S-48). The dashed lines are the simulations based on Equation (S-50), in which the thermodynamic correction factors are assumed to be described by $\Gamma_{ij} = \delta_{ij}$, the Kronecker delta. The Maxwell-Stefan diffusivities used in the simulations are: $Đ_1/r_c^2 = 2.75\times10^{-2}$ s^{-1}; $Đ_2/r_c^2 = 7.5\times10^{-4}$ s^{-1}; $Đ_1/Đ_2 = 36.7$.

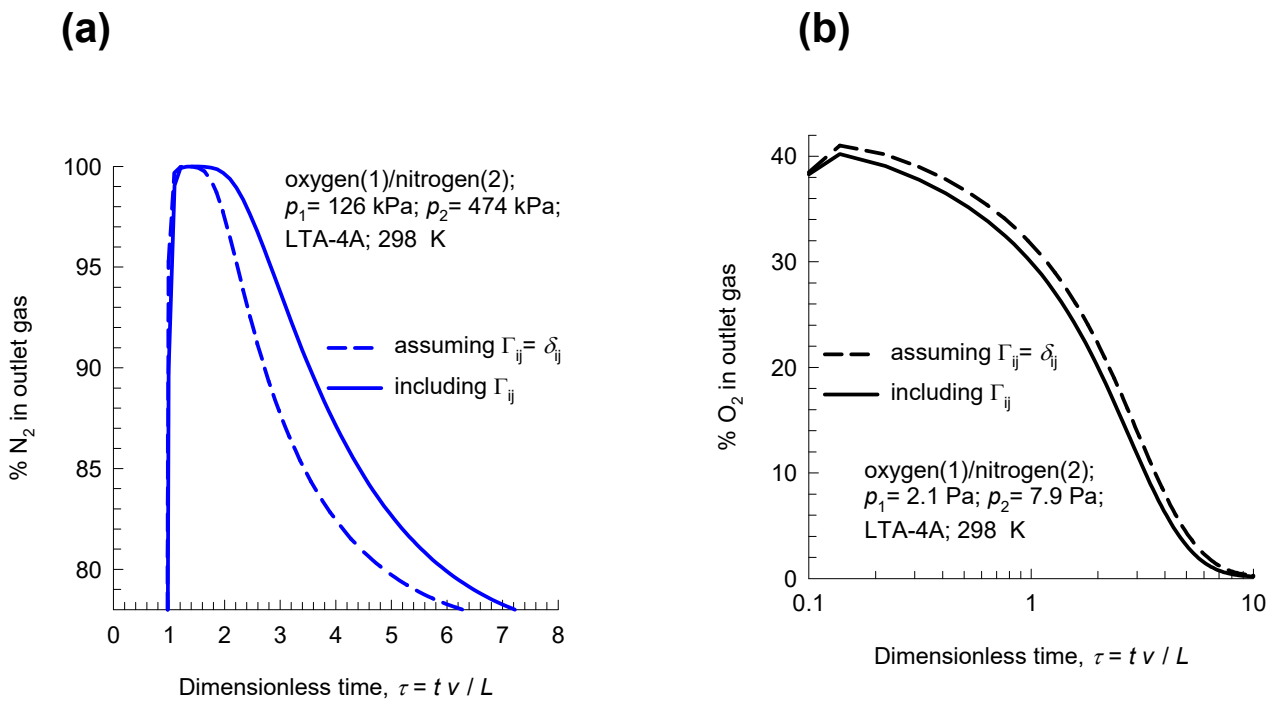

Figure S-13. (a) Transient breakthrough of 21/79 $O_2(1)/N_2(2)$ feed mixture in a fixed bed adsorber packed with LTA-4A operating at a total pressure of 600 kPa and 298 K. The partial pressures of the components in the bulk gas phase at the inlet are p_1 = 126 kPa, p_2 = 474 kPa. (b) Co-current blowdown of $O_2(1)/N_2(2)$ mixtures in fixed bed packed with DDR zeolite crystals. The initial loadings are those corresponding to the equilibrated loadings in (a). At time t = 0, the bulk gas phase mixture is maintained at partial pressures p_1 =2.1 Pa, p_2 = 7.9 Pa. The continuous solid lines are breakthrough simulations based on Equation (S-48). The dashed lines are the simulations based on Equation (S-50), in which the thermodynamic correction factors are assumed to be described by $\Gamma_{ij} = \delta_{ij}$, the Kronecker delta. The unary isotherms are provided in Table S-3. The Maxwell-Stefan diffusivities used in the simulations are: $Đ_1/r_c^2 = 2.75\times10^{-2}$ s^{-1}; $Đ_2/r_c^2 = 7.5\times10^{-4}$ s^{-1}; $Đ_1/Đ_2 = 36.7$.

8 Separation of C_3H_6/C_3H_8 mixtures

Propene is an important feedstock in the petrochemical industry. Propene is mostly used to make polypropylene, which accounts for nearly two-thirds of global propylene consumption. Other outlets include acrylonitrile, propylene oxide, a number of alcohols, cumene and acrylic acid. Propene is a by-product from the steam cracking of liquid feedstocks such as naphtha and liquefied petroleum gas (LPG), as well as off-gases produced in fluid catalytic cracking (FCC) units in refineries. It is also made via on-purpose technologies such as propane dehydrogenation and metathesis.

Cryogenic distillation of C_3H_6/C_3H_8 mixtures is the currently used technology for making polymer grade propene (99.5% minimum purity). 90% pure propane is used for various purposes such as fuel for engines, oxy-gas torches, barbecues; this can be obtained as the bottoms product of the cryogenic distillation column.[29] The boiling points are close to each other: propene (226 K), and propane (231.3 K). Consequently the distillation columns are some of the largest and tallest distillation columns used in the petrochemical industries with about 150 - 200 trays, and operating at reflux ratios of about 15. In fact, the U.S. Department of Energy has established that propene/propane separation is the most energy-intensive single distillation process practiced commercially.[29]

A pressure swing adsorption (PSA) process can be an attractive alternative for propene/propane separation, because of its expected low energy demand. A variety of adsorbents have been investigated for this separation task.[29, 51-53] With great potential for alkene/alkane separations are MOFs with coordinatively unsaturated metal centers that may be created by evacuation of frameworks that have metal-bound solvent molecules. This strategy has been employed to expose M^{2+} cation sites in M_2(dobdc) [M = Mg, Mn, Co, Ni, Zn, Fe; $dobdc^{4-}$ = 2,5- dioxido-1,4-benzenedicarboxylate]; these MOFs are also referred to as M-MOF-74 and CPO-27-M. Unsaturated alkynes, and alkenes such as C_2H_2, C_2H_4, and C_3H_6 can bind with Fe^{2+} of FeMOF-74, with side-on attachment and π-coordination;

[54, 55] The capability of M-MOF-74 for the technologically important separations of C_2H_2/C_2H_4, C_2H_4/C_2H_6, and C_3H_6/C_3H_8 mixtures has been established in laboratory studies.[54, 55] Other adsorbents that are also based on adsorption selectivity in favor of the unsaturated propene include: CuBTC,[56] LTA-4A zeolite,[51, 52] and NaX (= 13X) zeolite.[51, 53]

An important disadvantage of the C_3H_6/C_3H_8 separations with the adsorbents listed above is that the desired alkene product, required for production of polymer grade feedstock, can only be recovered in the desorption phase. It becomes necessary to operate with multiple beds involving five different steps; the C_3H_6 product of the desired purity is recovered in the final step by counter-current vacuum blowdown;[52, 53, 57] see Figure S-14.

The recovery of high purity C_3H_6 product in the final vacuum blowdown step is expected to be enhanced if C_3H_8 is (almost) excluded during the high pressure adsorption cycle. Near-total exclusion of C_3H_8 is achievable by kinetically based separations using cage-type zeolites with 8-ring windows. Due to the small cross-section of the propene molecule (see Figure S-15), kinetic separations, selective to propene, are possible using (a) all-silica CHA zeolite (all-silica CHA zeolite, also named SiCHA, or (b) ZIF-8. For both CHA zeolite, and ZIF-8 the adsorption equilibrium is in favor of propane, whereas diffusion favors propene.

CHA zeolite consists of cages of volume 316 Å^3, separated by 3.8 Å × 4.2 Å 8-ring windows; the pore landscape and structural details are provided in Figure S-16, and Figure S-17).[29, 58-60] For CHA, the ratio of Maxwell-Stefan diffusivities, $Đ_1/Đ_2$ = 5000. The ratio of single-site Langmuir parameter b_2/b_1 = 2.67 at 353 K.

ZIF-8 has a cage-window SOD (sodalite) topology (see pore landscapes in Figure S-18, and Figure S-19). The crystallographic size of the windows of ZIF-8 are 3.3 Å, but the windows are flexible. Due to subtle differences in bond lengths and bond angles, the diffusivity of C_3H_6 (1) is significantly higher than that of C_3H_8 (2); Li et al.[61] report the value of the ratio $Đ_1/Đ_2$ = 125 based on the data on pure component uptakes. In ZIF-8, the adsorption strength of the saturated propane is higher than that of

propene. From the unary isotherm data in Table S-5, the ratio of single-site Langmuir parameter b_2/b_1 = 1.07 at 303 K.

8.1 Transient uptake of C_3H_6/C_3H_8 within crystals of all-silica CHA

Figure S-20(a) shows the simulations of transient uptake of 50/50 C_3H_6(1)/C_3H_8(2) mixtures within crystals of all-silica CHA at 353 K. The bulk gas mixture is maintained at partial pressures $p_1 = p_2 = 50$ kPa. The continuous solid lines are Maxwell-Stefan model simulations based on Equation (S-48). The Maxwell-Stefan diffusivities are $Đ_1/r_c^2 = 1.7\times10^{-4}$ s^{-1}; $Đ_2/r_c^2 = 3.4\times10^{-8}$ s^{-1}; $Đ_1/Đ_2 = 5000$. The more mobile C_3H_6 exhibits a pronounced overshoot in its approach to thermodynamic equilibrium. The attainment of supra-equilibrium loadings during the initial stages of transience signals the phenomenon of uphill diffusion, and enhanced separation. The dashed lines in Figure S-20(a)a are the simulations based on Equation (S-50), in which the thermodynamic correction factors are assumed to be described by $\Gamma_{ij} = \delta_{ij}$, the Kronecker delta. In this scenario, no C_3H_6 overshoot is observed indicating that thermodynamic coupling effects are the root cause of uphill diffusion.

Figure S-20(b) presents simulations of transient desorption process in which the initial loadings in the zeolite correspond to the final equilibrated loadings in Figure S-20(a), i.e. corresponding to the bulk gas phase maintained at partial pressures $p_1 = p_2 = 50$ kPa.. At time $t = 0$, the bulk gas phase partial pressures are reduced to the values $p_1 = p_2 = 5$ kPa. The continuous solid lines in Figure S-20(b) are Maxwell-Stefan model simulations based on Equation (S-48); these simulations show undershoot in the desorption of the more mobile C_3H_6. The dashed lines in Figure S-20(b) are the simulations based on Equation (S-50), in which the thermodynamic correction factors are assumed to be described by $\Gamma_{ij} = \delta_{ij}$, i.e. $\begin{bmatrix}\Gamma_{11} & \Gamma_{12}\\ \Gamma_{21} & \Gamma_{21}\end{bmatrix} = \begin{bmatrix}1 & 0\\ 0 & 1\end{bmatrix}$; in this scenario, no C_3H_6 undershoot is experienced. We conclude that the undershoot in the C_3H_6 uptake, that signals the phenomenon of uphill diffusion,[12, 41] is engendered by thermodynamic coupling effects.

8.2 Transient breakthrough of C_3H_6/C_3H_8 mixtures in fixed bed with CHA

Figure S-21(a) show the simulations of transient breakthrough of 50/50 $C_3H_6(1)/C_3H_8(2)$ mixtures in a fixed bed adsorber packed with crystals of all-silica CHA at 353 K and operating at a total pressure of 100 kPa. The continuous solid lines are Maxwell-Stefan model simulations based on Equation (S-48). The simulations clearly show that 90%+ pure C_3H_8 can be collected during the earlier stages of transience. If thermodynamic coupling effects are ignored (these simulations are shown by the dashed lines), the time interval during which 90%+ pure C_3H_8 can be recovered is reduced by about an order of magnitude. Expressed per kg of CHA zeolite in the packed bed, the respective productivities of 90%+ pure C_3H_8 are 0.62 and 0.06 mol kg^{-1}. Ignoring thermodynamic coupling effects underestimates the separation performance by a factor of about 10.

Figure S-21(b) presents simulations of the co-current blowdown of $C_3H_6(1)/C_3H_8(2)$ mixtures in fixed bed packed with CHA zeolite crystals. The initial loadings are those corresponding to the equilibrated loadings in Figure S-21(a). At time $t = 0$, the gas phase feed mixture is maintained at $p_1 = p_2 = 0.1$ Pa. The continuous solid lines are simulations taking due account of intra-crystalline diffusion using Equation (S-48). The dashed lines in Figure S-21(b) are the simulations in which thermodynamic coupling effects are ignored and Equation (S-50) is used to describe the transfer fluxes. For simulations that include thermodynamic coupling, the composition of the purged gas mixture during co-current blowdown is richer in the more mobile C_3H_6; this is directly attributable to uphill diffusion and the undershoot phenomena witnessed in Figure S-20(b).

8.3 Transient uptake of C_3H_6/C_3H_8 within crystals of ZIF-8

Figure S-22(a) shows the simulations of transient uptake of 50/50 $C_3H_6(1)/C_3H_8(2)$ mixtures within crystals of ZIF-8 at 303 K. The bulk gas mixture is maintained at partial pressures $p_1 = p_2 = 50$ kPa. The continuous solid lines are Maxwell-Stefan model simulations based on Equation (S-48). The Maxwell-Stefan diffusivities $Đ_1/r_c^2 = 1.5\times10^{-2}$ s^{-1}; $Đ_2/r_c^2 = 1.2\times10^{-4}$ s^{-1}; $Đ_1/Đ_2 = 125$. The more mobile C_3H_6 exhibits a pronounced overshoot in its approach to thermodynamic equilibrium. The attainment of

supra-equilibrium loadings during the initial stages of transience signals the phenomenon of uphill diffusion, and enhanced separation. The dashed lines in Figure S-22(a) are the simulations based on Equation (S-50), in which the thermodynamic correction factors are assumed to be described by $\Gamma_{ij} = \delta_{ij}$, the Kronecker delta. In this scenario, no C_3H_6 overshoot is observed indicating that thermodynamic coupling effects are the root cause of uphill diffusion.

Figure S-22(b) presents simulations of transient desorption process in which the initial loadings in the zeolite correspond to the final equilibrated loadings in Figure S-22(a), i.e. corresponding to the bulk gas phase maintained at partial pressures $p_1 = p_2 = 50$ kPa.. At time $t = 0$, the bulk gas phase partial pressures are reduced to the values $p_1 = p_2 = 5$ kPa. The continuous solid lines in Figure S-22(b) are Maxwell-Stefan model simulations based on Equation (S-48); these simulations show undershoot in the desorption of the more mobile C_3H_6. The dashed lines in Figure S-22(b) are the simulations based on Equation (S-50), in which the thermodynamic correction factors are assumed to be described by $\Gamma_{ij} = \delta_{ij}$, i.e. $\begin{bmatrix} \Gamma_{11} & \Gamma_{12} \\ \Gamma_{21} & \Gamma_{21} \end{bmatrix} = \begin{bmatrix} 1 & 0 \\ 0 & 1 \end{bmatrix}$; in this scenario, no C_3H_6 undershoot is experienced. We conclude that the undershoot in the C_3H_6 uptake, that signals the phenomenon of uphill diffusion,[12, 41] is engendered by thermodynamic coupling effects.

8.4 Transient breakthrough of C_3H_6/C_3H_8 mixtures in fixed bed with ZIF-8

Figure S-23(a) show the simulations of transient breakthrough of 50/50 $C_3H_6(1)/C_3H_8(2)$ mixtures in a fixed bed adsorber packed with crystals of all-silica CHA at 353 K and operating at a total pressure of 100 kPa. The continuous solid lines are Maxwell-Stefan model simulations based on Equation (S-48). The simulations clearly show that 90%+ pure C_3H_8 can be collected during the earlier stages of transience. If thermodynamic coupling effects are ignored (these simulations are shown by the dashed lines), the time interval during which 90%+ pure C_3H_8 can be recovered is reduced by about an order of magnitude. Expressed per kg of CHA zeolite in the packed bed, the respective productivities of 90%+

pure C_3H_8 are 0.62 and 0.06 mol kg^{-1}. Ignoring thermodynamic coupling effects underestimates the separation performance by a factor of about 10.

Figure S-23(b) presents simulations of the co-current blowdown of $C_3H_6(1)/C_3H_8(2)$ mixtures in fixed bed packed with CHA zeolite crystals. The initial loadings are those corresponding to the equilibrated loadings in Figure S-23(a). At time $t = 0$, the gas phase feed mixture is maintained at $p_1 = p_2 = 0.1$ Pa. The continuous solid lines are simulations taking due account of intra-crystalline diffusion using Equation (S-48). The dashed lines in Figure S-23(b) are the simulations in which thermodynamic coupling effects are ignored and Equation (S-50) is used to describe the transfer fluxes. For simulations that include thermodynamic coupling, the composition of the purged gas mixture during co-current blowdown is richer in the more mobile C_3H_6; this is directly attributable to uphill diffusion and the undershoot phenomena witnessed in Figure S-22(b).

8.5 List of Tables for Separation of C3H6/C3H8 mixtures

Table S-4. 1-site Langmuir parameters for C_3H_6/, and C_3H_8 in all-silica CHA zeolite at 353 K. These isotherm data are taken from Table 4 of Khalighi et al.[29]

	q_{sat} mol kg^{-1}	b Pa^{-1}
C_3H_6	2.9	3×10^{-5}
C_3H_8	2.9	8×10^{-5}

On the basis of the information provided in Table 4 of Khalighi et al.:[29]

The Maxwell-Stefan diffusivities are

$Đ_1/r_c^2 = 1.7\times10^{-4}$ s^{-1}; $Đ_2/r_c^2 = 3.4\times10^{-8}$ s^{-1}; $Đ_1/Đ_2 = 5000$.

Table S-5. 1-site Langmuir parameters for propene and propane in ZIF-8.[62] The *T*-dependent parameters are obtained by fitting the combined sets of pure component isotherm data of Li et al.[61] and Böhme et al.[63] determined for a variety of temperatures in the range 273 K to 408 K.

$$q = q_{sat}\frac{bp}{1+bp}\ ;\ b_A = b_0 \exp\left(\frac{E}{RT}\right)$$

	q_{sat} mol kg^{-1}	b_0 Pa^{-1}	E kJ mol^{-1}
propene	5.2	4.57×10^{-11}	33.9
propane	5.2	1.39×10^{-10}	31.3

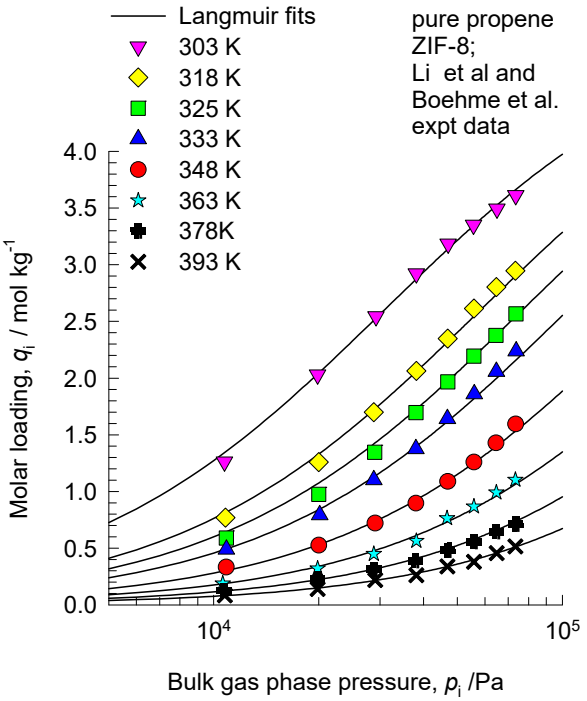

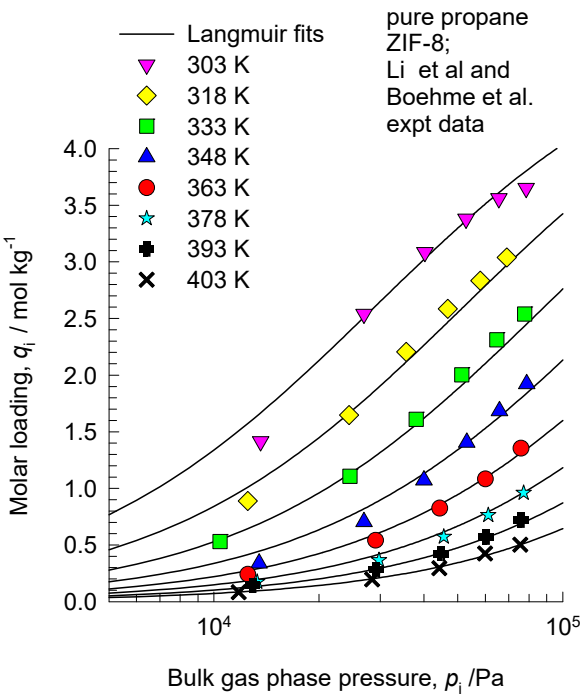

8.6 List of Figures for Separation of C3H6/C3H8 mixtures

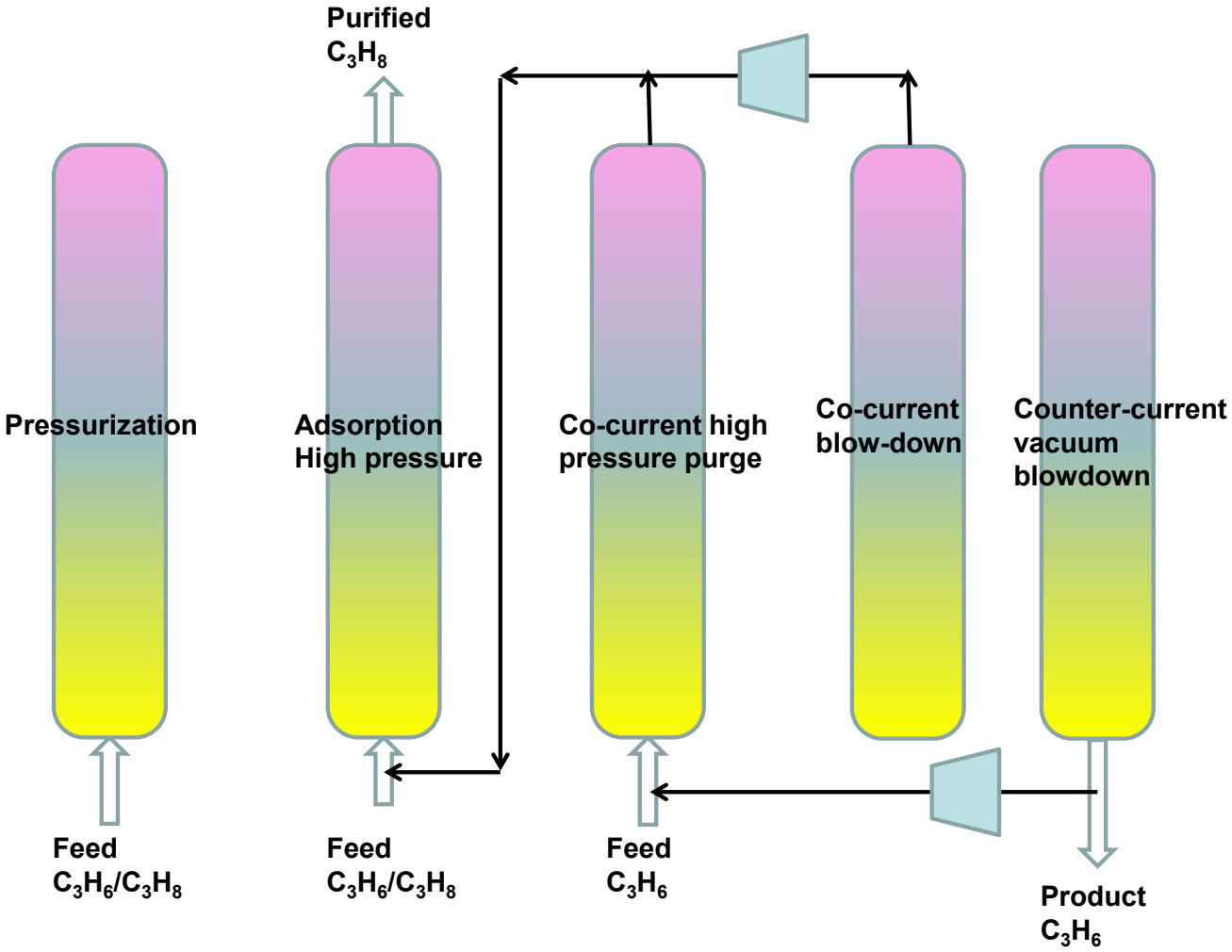

Figure S-14. Five-step P(V)SA process for separating C_3H_6/C_3H_8 mixtures.[52, 53, 57]

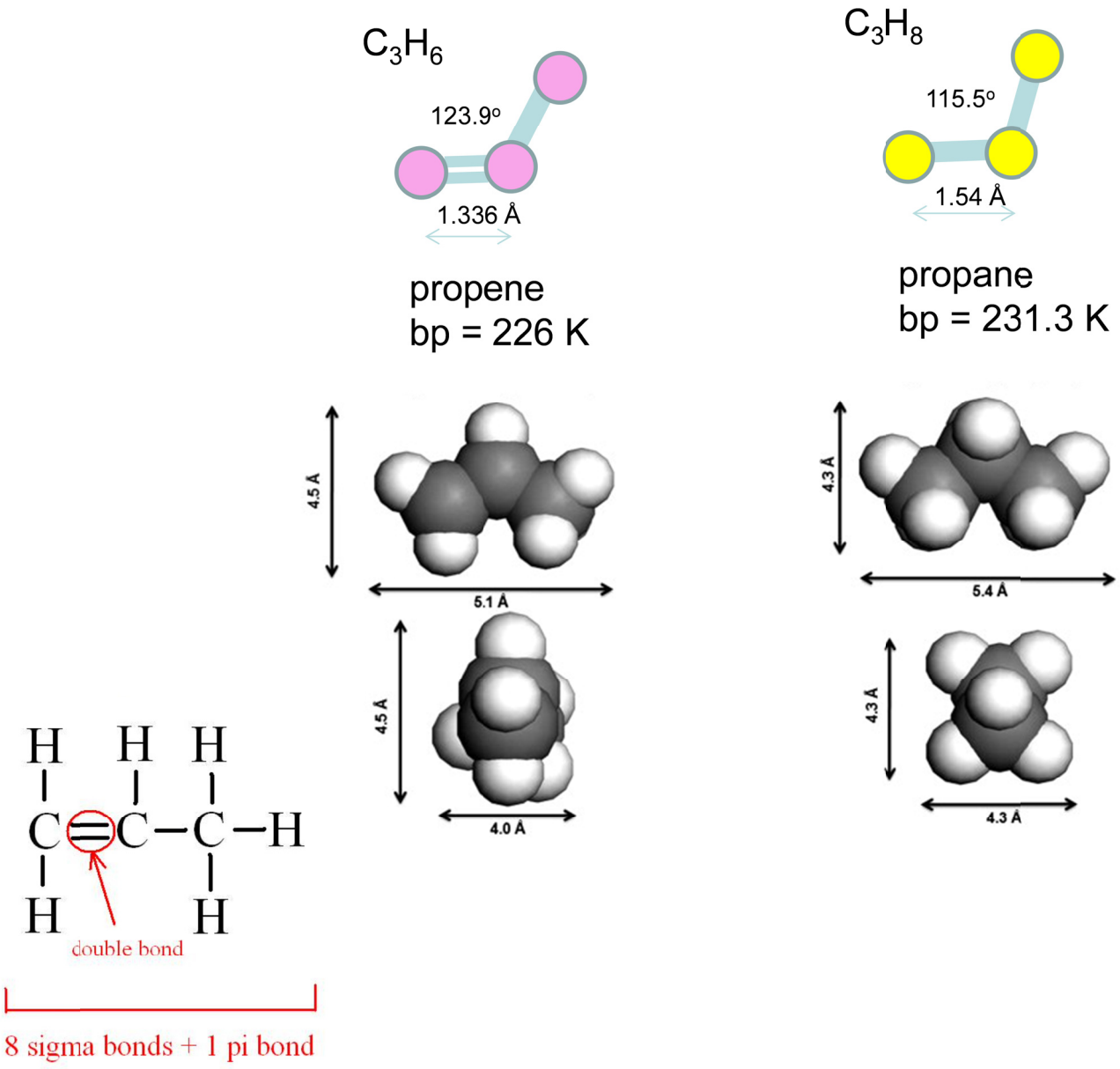

Figure S-15. Molecular dimensions of C_3H_6 and C_3H_8, culled from the literature.[64]

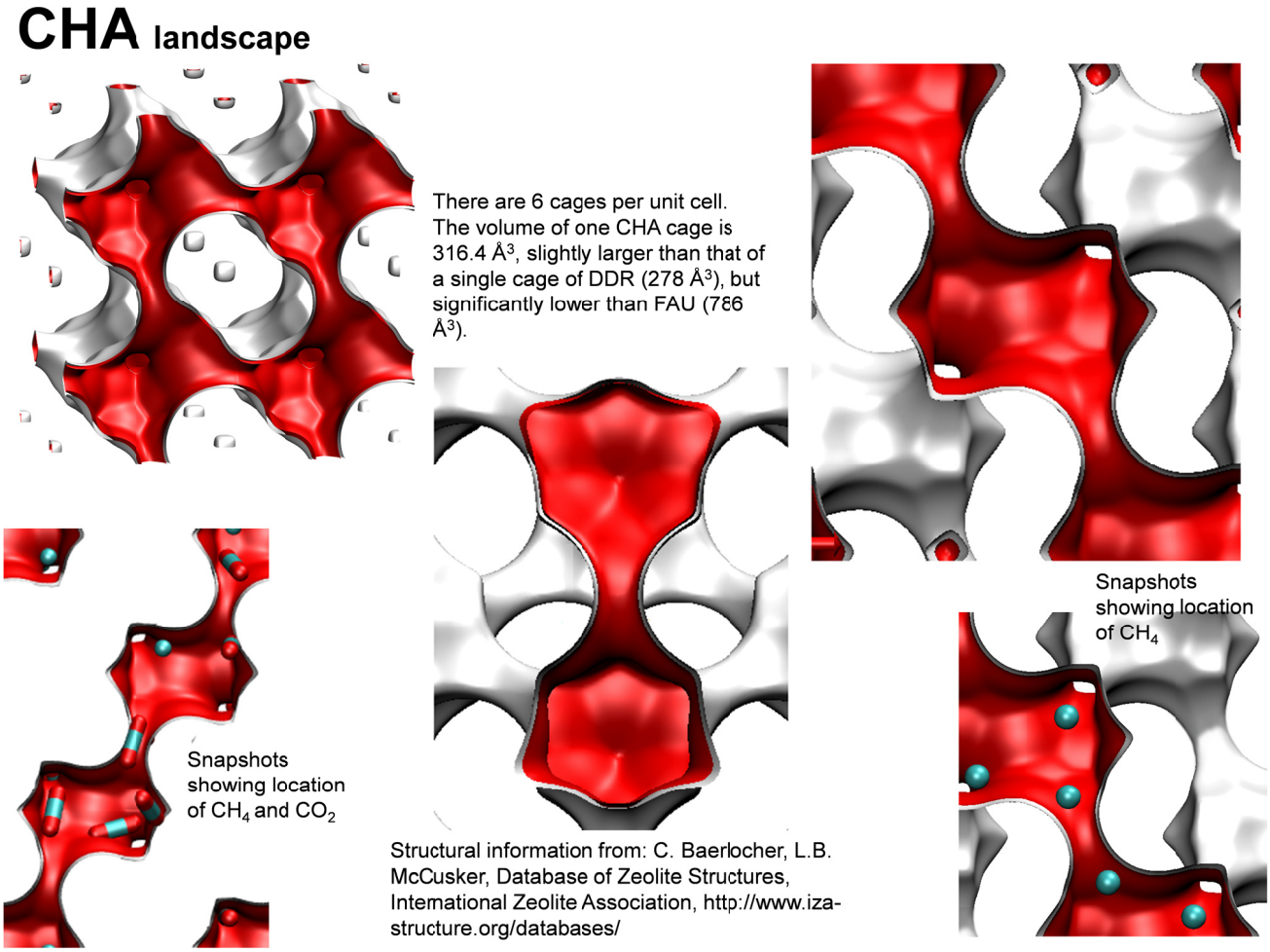

Figure S-16. Pore landscape and structural details of all-silica CHA zeolite, also called SiCHA.

CHA window and pore dimensions

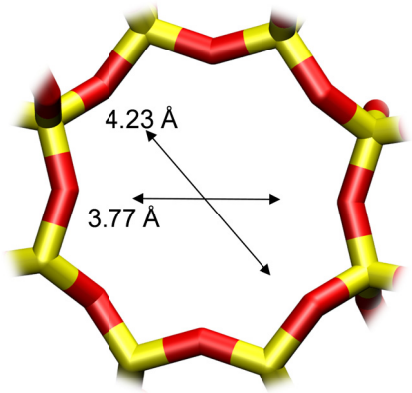

CHA

The window dimensions calculated using the van der Waals diameter of framework atoms = 2.7 Å are indicated above by the arrows.

	CHA
a /Å	15.075
b /Å	23.907
c /Å	13.803
Cell volume / Å^3	4974.574
conversion factor for [molec/uc] to [mol per kg Framework]	0.2312
conversion factor for [molec/uc] to [kmol/m^3]	0.8747
ρ [kg/m3]	1444.1
MW unit cell [g/mol(framework)]	4326.106
ψ, fractional pore volume	0.382
open space / Å^3/uc	1898.4
Pore volume / cm^3/g	0.264
Surface area /m^2/g	758.0
DeLaunay diameter /Å	3.77

Figure S-17. Pore landscape and structural details of all-silica CHA zeolite, also called SiCHA.

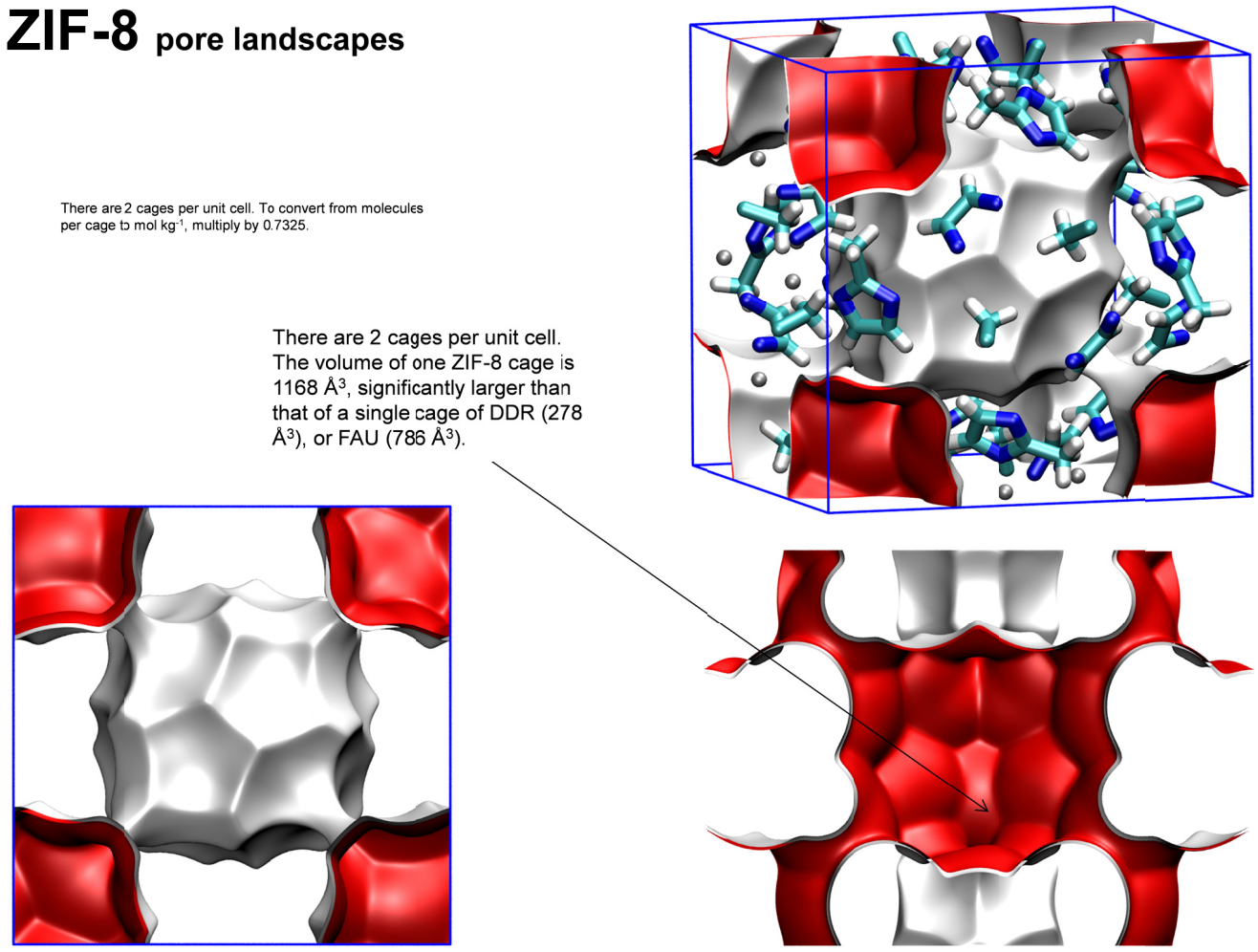

Figure S-18. Pore landscape and structural details of ZIF-8.

ZIF-8 dimensions

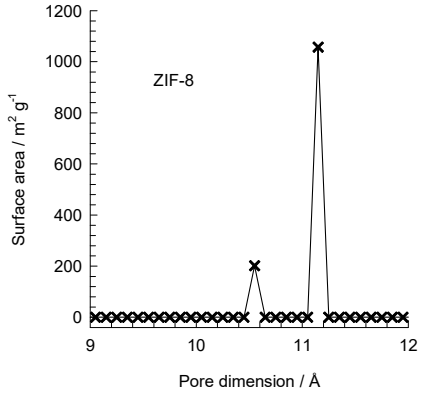

This plot of surface area versus pore dimension is determined using a combination of the DeLaunay triangulation method for pore dimension determination, and the procedure of Düren for determination of the surface area.

	ZIF-8
a /Å	16.991
b /Å	16.991
c /Å	16.991
Cell volume / Å^3	4905.201
conversion factor for [molec/uc] to [mol per kg Framework]	0.3663
conversion factor for [molec/uc] to [kmol/m^3]	0.7106
ρ [kg/m3]	924.253
MW unit cell [g/mol(framework)]	2730.182
ϕ, fractional pore volume	0.476
open space / Å^3/uc	2337.0
Pore volume / cm^3/g	0.515
Surface area /m^2/g	1164.7
DeLaunay diameter /Å	3.26

Figure S-19. Pore landscape and structural details of ZIF-8.

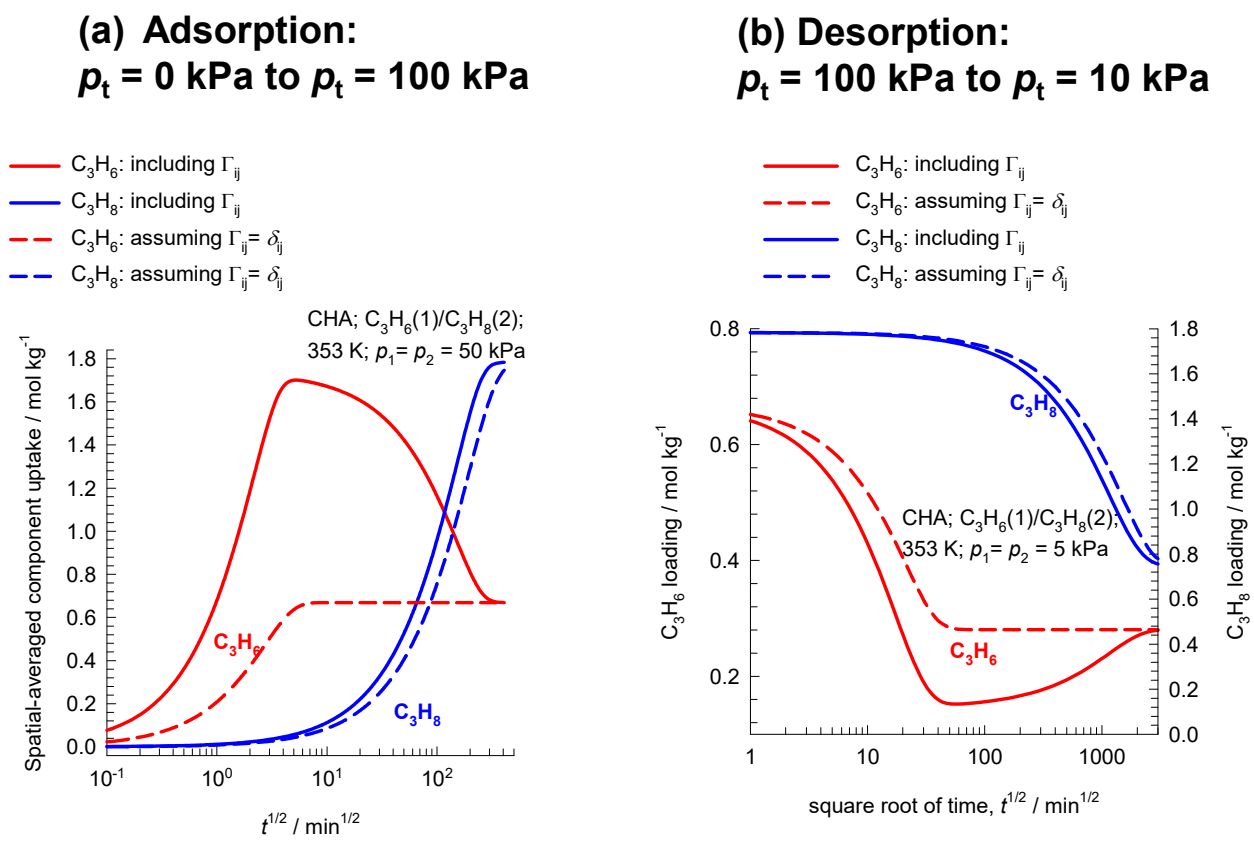

Figure S-20. (a) Simulations of transient uptake of 50/50 $C_3H_6(1)/C_3H_8(2)$ mixtures within crystals of all-silica CHA at 353 K; the bulk gas mixture is maintained at partial pressures $p_1 = p_2 = 50$ kPa. (b) Transient desorption of $C_3H_6(1)/C_3H_8(2)$ mixtures in all silica CHA zeolite at 353 K. The initial loadings are those corresponding to the final equilibrated loadings in (a). At time $t = 0$, the bulk gas phase mixture is maintained at partial pressures $p_1 = p_2 = 5$ kPa. The continuous solid lines are Maxwell-Stefan model simulations based on Equation (S-48). The dashed lines are the simulations based on Equation (S-50), in which the thermodynamic correction factors are assumed to be described by $\Gamma_{ij} = \delta_{ij}$, the Kronecker delta. The unary isotherms are provided in Table S-4. The Maxwell-Stefan diffusivities are $Đ_1/r_c^2 = 1.7\times10^{-4}$ s^{-1}; $Đ_2/r_c^2 = 3.4\times10^{-8}$ s^{-1}; $Đ_1/Đ_2 = 5000$.

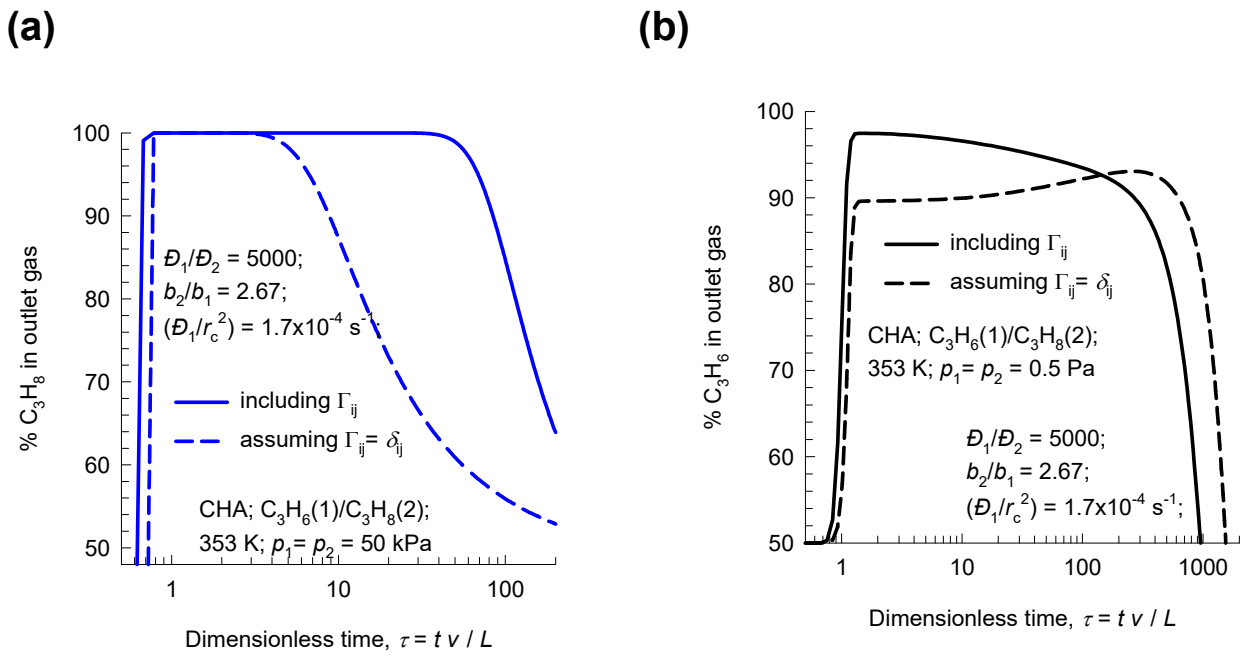

Figure S-21. (a) Simulations of transient breakthrough of 50/50 $C_3H_6(1)/C_3H_8(2)$ mixtures in a fixed bed adsorber packed with crystals of all-silica CHA at 353 K; the bulk gas phase feed mixture is maintained at partial pressures $p_1 = p_2 = 50$ Pa. (b) Co-current blowdown of $C_3H_6(1)/C_3H_8(2)$ mixtures in fixed bed packed with CHA zeolite crystals. The initial loadings are those corresponding to the equilibrated loadings in (a). At time $t = 0$, the bulk gas phase feed mixture is maintained at partial pressures $p_1 = p_2 = 0.5$ Pa. The continuous solid lines are Maxwell-Stefan model simulations based on Equation (S-48). The dashed lines are the simulations based on Equation (S-50), in which the thermodynamic correction factors are assumed to be described by $\Gamma_{ij} = \delta_{ij}$, the Kronecker delta. The unary isotherms are provided in Table S-4. The Maxwell-Stefan diffusivities are $Đ_1/r_c^2 = 1.7\times10^{-4}$ s^{-1}; $Đ_2/r_c^2 = 3.4\times10^{-8}$ s^{-1}; $Đ_1/Đ_2 = 5000$.

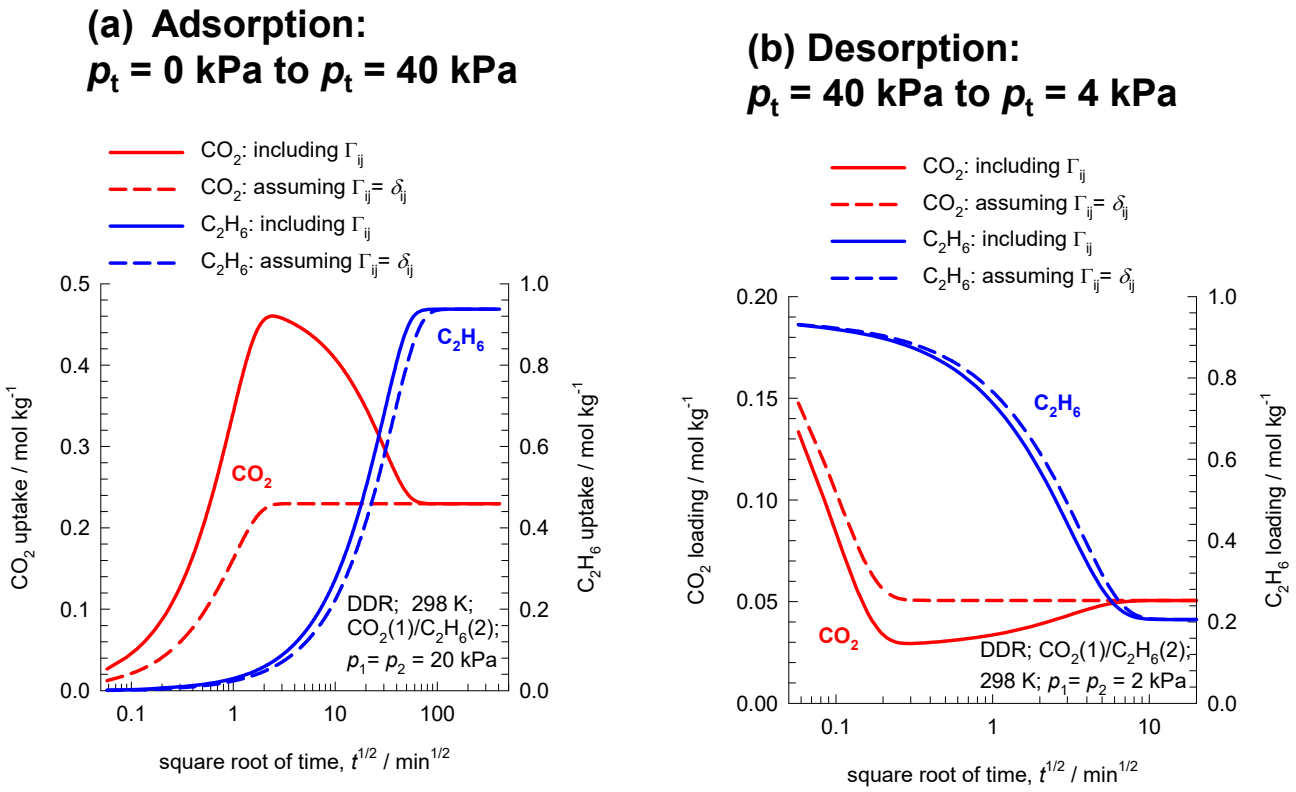

Figure S-22. (a) Simulations of transient uptake of 50/50 $C_3H_6(1)/C_3H_8(2)$ mixtures within crystals of ZIF-8 at 303 K; the bulk gas mixture is maintained at partial pressures $p_1 = p_2 = 50$ kPa. (b) Transient desorption of $C_3H_6(1)/C_3H_8(2)$ mixtures in ZIF-8 at 303 K; the initial loadings are those corresponding to the final equilibrated loadings in (a). At time $t = 0$, the bulk gas phase mixture is maintained at partial pressures $p_1 = p_2 = 5$ kPa. The continuous solid lines are Maxwell-Stefan model simulations based on Equation (S-48). The dashed lines are the simulations based on Equation (S-50), in which the thermodynamic correction factors are assumed to be described by $\Gamma_{ij} = \delta_{ij}$, the Kronecker delta. The simulations use the isotherm parameters specified in Table S-5, along with $Đ_1/r_c^2 = 1.5\times10^{-2}$ s^{-1}; $Đ_2/r_c^2 = 1.2\times10^{-4}$ s^{-1}; $Đ_1/Đ_2 = 125$.

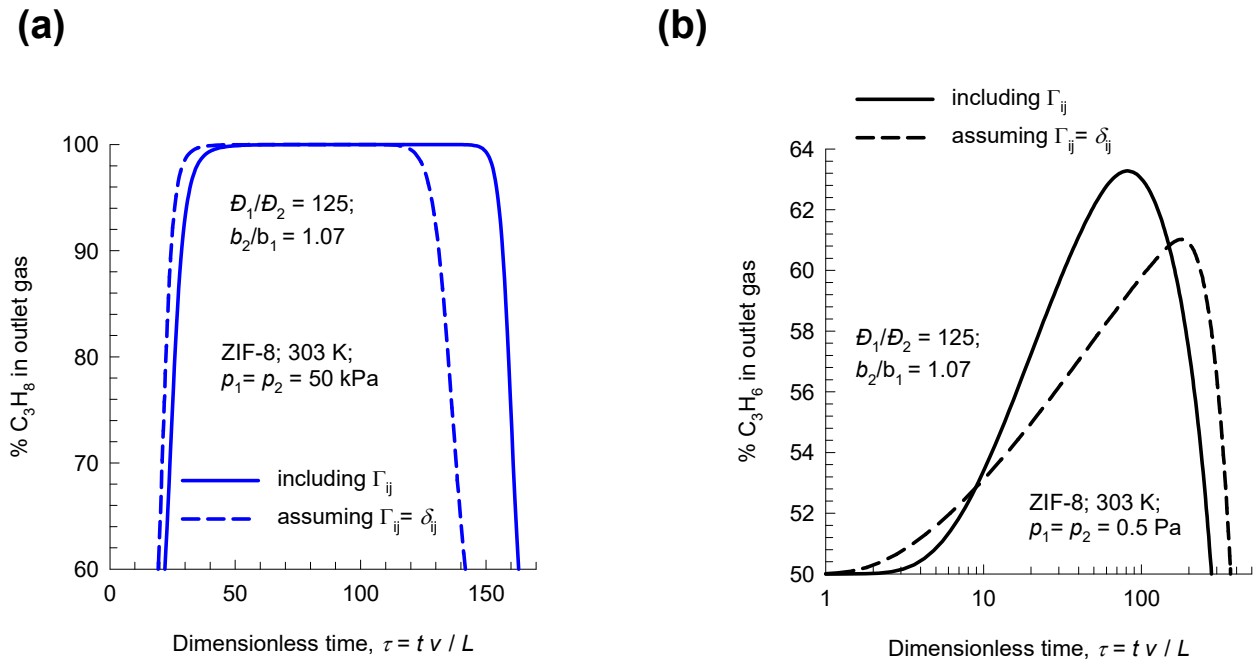

Figure S-23. (a) Simulations of transient breakthrough of 50/50 $C_3H_6(1)/C_3H_8(2)$ mixtures in a fixed bed adsorber packed with crystals of ZIF-8 at 303 K; the bulk gas phase feed mixture is maintained at partial pressures $p_1 = p_2 = 50$ Pa. (b) Co-current blowdown of $C_3H_6(1)/C_3H_8(2)$ mixtures in fixed bed packed with ZIF-8 crystals. The initial loadings are those corresponding to the equilibrated loadings in (a). At time $t = 0$, the bulk gas phase feed mixture is maintained at partial pressures $p_1 = p_2 = 0.5$ Pa. The continuous solid lines are Maxwell-Stefan model simulations based on Equation (S-48). The dashed lines are the simulations based on Equation (S-50), in which the thermodynamic correction factors are assumed to be described by $\Gamma_{ij} = \delta_{ij}$, the Kronecker delta.. The simulations use the isotherm parameters specified in Table S-5, along with $Đ_1/r_c^2 = 1.5\times10^{-2}$ s^{-1}; $Đ_2/r_c^2 = 1.2\times10^{-4}$ s^{-1}; $Đ_1/Đ_2 = 125$.

9 Nomenclature

Latin alphabet

b_i	Langmuir parameter, Pa^{-1}
$[B]$	matrix of inverse M-S coefficients, m^{-2} s
c_i	molar concentration of species *i*, mol m^{-3}
c_t	total molar concentration in mixture, mol m^{-3}
c_{i0}	molar concentration of species *i* in fluid mixture at inlet to adsorber, mol m^{-3}
$Đ_i$	Maxwell-Stefan diffusivity for molecule-wall interaction, m^2 s^{-1}
$Đ_{ij}$	M-S exchange coefficient for *n*-component mixture, m^2 s^{-1}
$Đ_{12}$	M-S exchange coefficient for binary mixture, m^2 s^{-1}
$[D]$	matrix of Fick diffusivities, m^2 s^{-1}
f_i	partial fugacity of species *i*, Pa
n	number of species in the mixture, dimensionless
L	length of packed bed adsorber, m
N_i	molar flux of species *i* with respect to framework, mol m^{-2} s^{-1}
p_i	partial pressure of species *i* in mixture, Pa
p_t	total system pressure, Pa
q_i	component molar loading of species *i*, mol kg^{-1}
$q_{i,sat}$	molar loading of species *i* at saturation, mol kg^{-1}
q_t	total molar loading in mixture, mol kg^{-1}
$\bar{q}_i(t)$	spatial-averaged component uptake of species *i*, mol kg^{-1}
r	radial direction coordinate, m
r_c	radius of crystallite, m

Nomenclature

R	gas constant, 8.314 J mol^{-1} K^{-1}
t	time, s
T	absolute temperature, K
u_i	velocity of motion of adsorbate species *i* with respect to the framework material, m s^{-1}
u	superficial gas velocity in packed bed, m s^{-1}
v	interstitial gas velocity in packed bed, m s^{-1}
x_i	mole fraction of species *i* in adsorbed phase, dimensionless
z	distance along the adsorber, m

Greek alphabet

Γ_{ij}	thermodynamic factors, dimensionless
$[\Gamma]$	matrix of thermodynamic factors, dimensionless
δ_{ij}	Kronecker delta, dimensionless
ε	voidage of packed bed, dimensionless
θ_i	fractional occupancy of component *i*, dimensionless
θ_t	fractional occupancy of adsorbed mixture, dimensionless
θ_V	fractional vacancy, dimensionless
$[\Lambda]$	matrix of Maxwell-Stefan diffusivities, m^2 s^{-1}
μ_i	molar chemical potential, J mol^{-1}
ρ	framework density, kg m^{-3}
τ	time, dimensionless

Subscripts

i	referring to component *i*

Nomenclature

t	referring to total mixture
sat	referring to saturation conditions

10 References

(1) Ruthven, D. M. *Principles of Adsorption and Adsorption Processes*. John Wiley: New York, 1984.

(2) Myers, A. L.; Prausnitz, J. M. Thermodynamics of Mixed Gas Adsorption. *A.I.Ch.E.J.* **1965**, *11*, 121-130.

(3) Siperstein, F. R.; Myers, A. L. Mixed-Gas Adsorption. *A.I.Ch.E.J.* **2001**, *47*, 1141-1159.

(4) Rao, M. B.; Sircar, S. Thermodynamic consistency for binary gas adsorption equilibria. *Langmuir* **1999**, *15*, 7258-7267.

(5) Skoulidas, A. I.; Sholl, D. S.; Krishna, R. Correlation effects in diffusion of CH_4/CF_4 mixtures in MFI zeolite. A study linking MD simulations with the Maxwell-Stefan formulation. *Langmuir* **2003**, *19*, 7977-7988.

(6) Chempath, S.; Krishna, R.; Snurr, R. Q. Nonequilibrium MD simulations of difusion of binary mixtures containing short n-alkanes in faujasite. *J. Phys. Chem. B* **2004**, *108*, 13481-13491.

(7) Krishna, R. Describing the Diffusion of Guest Molecules inside Porous Structures. *J. Phys. Chem. C* **2009**, *113*, 19756-19781.

(8) Krishna, R. Diffusion in Porous Crystalline Materials. *Chem. Soc. Rev.* **2012**, *41*, 3099-3118.

(9) Krishna, R.; van Baten, J. M. Onsager coefficients for binary mixture diffusion in nanopores. *Chem. Eng. Sci.* **2008**, *63*, 3120-3140.

(10) Hansen, N.; Keil, F. J. Multiscale modeling of reaction and diffusion in zeolites: from the molecular level to the reactor. *Soft Mater.* **2012**, *10*, 179-201.

(11) Krishna, R.; van Baten, J. M. An Investigation of the Characteristics of Maxwell-Stefan Diffusivities of Binary Mixtures in Silica Nanopores. *Chem. Eng. Sci.* **2009**, *64*, 870-882.

(12) Krishna, R.; van Baten, J. M. Unified Maxwell-Stefan Description of Binary Mixture Diffusion in Micro- and Meso- Porous Materials. *Chem. Eng. Sci.* **2009**, *64*, 3159-3178.

(13) Krishna, R.; van Baten, J. M. Maxwell-Stefan modeling of slowing-down effects in mixed gas permeation across porous membranes. *J. Membr. Sci.* **2011**, *383*, 289-300.

(14) Krishna, R. Using the Maxwell-Stefan formulation for Highlighting the Influence of Interspecies (1-2) Friction on Binary Mixture Permeation across Microporous and Polymeric Membranes. *J. Membr. Sci.* **2017**, *540*, 261-276.

(15) Krishna, R. The Maxwell-Stefan Description of Mixture Diffusion in Nanoporous Crystalline Materials. *Microporous Mesoporous Mater.* **2014**, *185*, 30-50.

(16) Krishna, R. Tracing the Origins of Transient Overshoots for Binary Mixture Diffusion in Microporous Crystalline Materials. *Phys. Chem. Chem. Phys.* **2016**, *18*, 15482-15495.

(17) Krishna, R.; van Baten, J. M. Investigating the Influence of Diffusional Coupling on Mixture Permeation across Porous Membranes *J. Membr. Sci.* **2013**, *430*, 113-128.

(18) Krishna, R.; Baur, R. Modelling Issues in Zeolite Based Separation Processes. *Sep. Purif. Technol.* **2003**, *33*, 213-254.

(19) Krishna, R.; van Baten, J. M. Diffusion of alkane mixtures in zeolites. Validating the Maxwell-Stefan formulation using MD simulations. *J. Phys. Chem. B* **2005**, *109*, 6386-6396.

(20) Krishna, R.; van Baten, J. M. Influence of segregated adsorption on mixture diffusion in DDR zeolite. *Chem. Phys. Lett.* **2007**, *446*, 344-349.

(21) Krishna, R.; van Baten, J. M. Insights into diffusion of gases in zeolites gained from molecular dynamics simulations. *Microporous Mesoporous Mater.* **2008**, *109*, 91-108.

References

(22) Krishna, R.; van Baten, J. M. Segregation effects in adsorption of CO_2 containing mixtures and their consequences for separation selectivities in cage-type zeolites. *Sep. Purif. Technol.* **2008**, *61*, 414-423.

(23) Krishna, R.; van Baten, J. M. Describing Mixture Diffusion in Microporous Materials under Conditions of Pore Saturation. *J. Phys. Chem. C* **2010**, *114*, 11557-11563.

(24) Krishna, R.; van Baten, J. M. A molecular dynamics investigation of the diffusion characteristics of cavity-type zeolites with 8-ring windows. *Microporous Mesoporous Mater.* **2011**, *137*, 83-91.

(25) Habgood, H. W. The Kinetics of Molecular Sieve Action. Sorption of Nitrogen-Methane Mixtures by Linde Molecular Sieve 4A. *Canad. J. Chem.* **1958**, *36*, 1384-1397.

(26) Ruthven, D. M.; Farooq, S.; Knaebel, K. S. *Pressure swing adsorption*. VCH Publishers: New York, 1994.

(27) Farooq, S.; Ruthven, D. M. Numerical-Simulation of a Kinetically Controlled Pressure Swing Adsorption Bulk Separation Process Based on a Diffusion-Model. *Chem. Eng. Sci.* **1991**, *46*, 2213-2224.

(28) Farooq, S.; Rathor, M. N.; Hidajat, K. A Predictive Model for a Kinetically Controlled Pressure Swing Adsorption Separation Process. *Chem. Eng. Sci.* **1993**, *48*, 4129-4141.

(29) Khalighi, M.; Chen, Y. F.; Farooq, S.; Karimi, I. A.; Jiang, J. W. Propylene/Propane Separation Using SiCHA. *Ind. Eng. Chem. Res.* **2013**, *52*, 3877-3892.

(30) Krishna, R. A Maxwell-Stefan-Glueckauf Description of Transient Mixture Uptake in Microporous Adsorbents. *Sep. Purif. Technol.* **2018**, *191*, 392-399. https://doi.org/10.1016/j.seppur.2017.09.057.

(31) Geddes, R. L. Local efficiencies of bubble-plate fractionators. *Trans. Am. Inst. Chem. Engrs.* **1946**, *42*, 79-105.

(32) Glueckauf, E. Theory of Chromatography. Part 10- Formulae for Diffusion into Spheres and their Application to Chromatography. *Trans. Faraday Soc.* **1955**, *51*, 1540-1551.

(33) Kooijman, H. A.; Taylor, R. A dynamic nonequilibrium model of tray distillation columns. *A.I.Ch.E.J.* **1995**, *41*, 1852-1863.

(34) Michelsen, M. An efficient general purpose method of integration of stiff ordinary differential equations. *A.I.Ch.E.J.* **1976**, *22*, 594-597.

(35) Bulirsch, R.; Stoer, J. Numerical treatment of ordinary differential equations by extrapolation methods. *Numer. Math.* **1966**, *8*, 1-14.

(36) Krishna, R.; Baur, R. Diffusion, Adsorption and Reaction in Zeolites: Modelling and Numerical Issues. http://krishna.amsterchem.com/zeolite/, University of Amsterdam, Amsterdam, 1 January 2015.

(37) Krishna, R.; van Baten, J. M. Investigating the potential of MgMOF-74 membranes for CO_2 capture. *J. Membr. Sci.* **2011**, *377*, 249-260.

(38) He, Y.; Krishna, R.; Chen, B. Metal-Organic Frameworks with Potential for Energy-Efficient Adsorptive Separation of Light Hydrocarbons. *Energy Environ. Sci.* **2012**, *5*, 9107-9120.

(39) Krishna, R. Screening Metal-Organic Frameworks for Mixture Separations in Fixed-Bed Adsorbers using a Combined Selectivity/Capacity Metric. *RSC Adv.* **2017**, *7*, 35724-35737. https://doi.org/10.1039/C7RA07363A.

(40) Krishna, R. Methodologies for Evaluation of Metal-Organic Frameworks in Separation Applications. *RSC Adv.* **2015**, *5*, 52269-52295.

(41) Krishna, R.; Long, J. R. Screening metal-organic frameworks by analysis of transient breakthrough of gas mixtures in a fixed bed adsorber. *J. Phys. Chem. C* **2011**, *115*, 12941-12950.

(42) Tagliabue, M.; Farrusseng, D.; Valencia, S.; Aguado, S.; Ravon, U.; Rizzo, C.; Corma, A.; Mirodatos, C. Natural gas treating by selective adsorption: Material science and chemical engineering interplay. *Chem. Eng. J.* **2009**, *155*, 553-566.

(43) Bhadra, S. J.; Farooq, S. Separation of Methane Nitrogen Mixture by Pressure Swing Adsorption for Natural Gas Upgrading. *Ind. Eng. Chem. Res.* **2011**, *50*, 14030-14045.

(44) Majumdar, B.; Bhadra, S. J.; Marathe, R. P.; Farooq, S. Adsorption and Diffusion of Methane and Nitrogen in Barium Exchanged ETS-4. *Ind. Eng. Chem. Res.* **2011**, *50*, 3021-3034.

(45) Jayaraman, A.; Hernandez-Maldonado, A. J.; Yang, R. T.; Chinn, D.; Munson, C. L.; Mohr, D. H. Clinoptilolites for Nitrogen/Methane Separation. *Chem. Eng. Sci.* **2004**, *59*, 2407-2417.

(46) Yang, R. T. *Adsorbents: Fundamentals and Applications*. John Wiley & Sons, Inc.: Hoboken, New Jersey, 2003.

(47) Krishna, R. Diffusing Uphill with James Clerk Maxwell and Josef Stefan. *Chem. Eng. Sci.* **2019**, *195*, 851-880. https://doi.org/10.1016/j.ces.2018.10.032.

(48) Binder, T. *Mass Transport in Nanoporous Materials: New Insights from Micro-Imaging by Interference Microscopy*. Ph.D. Dissertation, Universität Leipzig, Leipzig, 2013.

(49) Farooq, S.; Ruthven, D. M.; Boniface, H. A. Numerical-Simulation of a Pressure Swing Adsorption Oxygen Unit. *Chem. Eng. Sci.* **1989**, *44*, 2809-2816.

(50) Farooq, S. Sorption and Diffusion of Oxygen and Nitrogen in Molecular- Sieve RS-10. *Gas Sep. Purif.* **1995**, *9*, 205-212.

(51) Da Silva, F. A.; Rodrigues, A. E. Vacuum swing adsorption for propylene/propane separation with 4A zeolite. *Ind. Eng. Chem. Res.* **2001**, *40*, 5758-5774.

(52) Grande, C. A.; Poplow, F.; Rodrigues, A. E. Vacuum pressure swing adsorption to produce polymer-grade polypropylene. *Separ. Sci. Technol.* **2010**, *45*, 1252-1259.

(53) Da Silva, F. A.; Rodrigues, A. E. PropylenePropane Separation by Vacuum Swing Adsorption Using 13X Zeolite. *A.I.Ch.E.J.* **2001**, *47*, 341-357.

(54) Bloch, E. D.; Queen, W. L.; Krishna, R.; Zadrozny, J. M.; Brown, C. M.; Long, J. R. Hydrocarbon Separations in a Metal-Organic Framework with Open Iron(II) Coordination Sites. *Science* **2012**, *335*, 1606-1610.

(55) Geier, S. J.; Mason, J. A.; Bloch, E. D.; Queen, W. L.; Hudson, M. R.; Brown, C. M.; Long, J. R. Selective adsorption of ethylene over ethane and propylene over propane in the metal–organic frameworks M_2(dobdc) (M = Mg, Mn, Fe, Co, Ni, Zn). *Chem. Sci.* **2013**, *4*, 2054-2061.

(56) Yoon, J. W.; Jang, I. T.; Lee, K.-Y.; Hwang, Y. K.; Chang, J.-S. Adsorptive Separation of Propylene and Propane on a Porous Metal-Organic Framework, Copper Trimesate. *Bull. Korean Chem. Soc.* **2010**, *31*, 220-223.

(57) Khalighi, M.; Karimi, I. A.; Farooq, S. Comparing SiCHA and 4A Zeolite for Propylene/Propane Separation using a Surrogate-Based Simulation/Optimization Approach. *Ind. Eng. Chem. Res.* **2014**, *53*, 16973-16983.

(58) Olson, D. H.; Camblor, M. A.; Vallaescusa, L. A.; Kuehl, G. H. Light hydrocarbon sorption properties of pure silica Si-CHA and ITQ-3 and high silica ZSM-58. *Microporous Mesoporous Mater.* **2004**, *67*, 27-33.

(59) Hedin, N.; DeMartin, G. J.; Roth, W. J.; Strohmaier, K. G.; Reyes, S. C. PFG NMR self-diffusion of small hydrocarbons in high silica DDR, CHA and LTA structures. *Microporous Mesoporous Mater.* **2008**, *109*, 327-334.

(60) Ruthven, D. M.; Reyes, S. C. Adsorptive separation of light olefins from paraffins. *Microporous Mesoporous Mater.* **2007**, *104*, 59-66.

(61) Li, K.; Olson, D. H.; Seidel, J.; Emge, T. J.; Gong, H.; Zeng, H.; Li, J. Zeolitic Imidazolate Frameworks for Kinetic Separation of Propane and Propene. *J. Am. Chem. Soc.* **2009**, *131*, 10368-10369.

(62) Krishna, R. Evaluation of Procedures for Estimation of the Isosteric Heat of Adsorption in Microporous Materials. *Chem. Eng. Sci.* **2015**, *123*, 191-196.

(63) Böhme, U.; Barth, B.; Paula, C.; Kuhnt, A.; Schwieger, W.; Mundstock, A.; Caro, J.; Hartmann, M. Ethene/Ethane and Propene/Propane Separation via the Olefin and Paraffin Selective Metal−Organic Framework Adsorbents CPO-27 and ZIF-8. *Langmuir* **2013**, *29*, 8592-8600.

(64) Chng, M. L.; Xiao, Y.; Chung, T.-S.; Toriida, M.; Tamai, S. Enhanced propylene/propane separation by carbonaceous membrane derived from poly (aryl ether ketone)/2,6-bis(4-azidobenzylidene)-4-methyl-cyclohexanone interpenetrating network. *Carbon* **2009**, *47*, 1857-1866.

References